

AD-A085 263

AUBURN UNIV ALA ENGINEERING EXPERIMENT STATION

F/6 17/9

INVESTIGATION OF COMPLEX ANGLE PROCESSING TO REDUCE RADOME INRU--ETC(U)

OCT 79 D G BURKS, E R GRAF

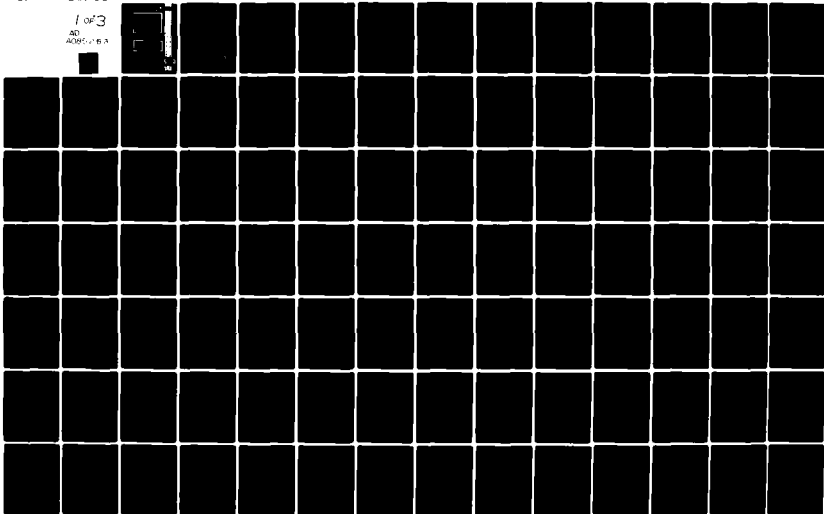
DAAK40-77-C-0022

UNCLASSIFIED

AU-EE-0022

NL

1 OF 3
AD
A085 263



LEVEL # 10

ELECTRICAL

ADA085253

DDC FILE COPY.

DISTRIBUTION STATEMENT A

Approved for public release;
Distribution Unlimited

ENGINEERING EXPERIMENT STATION

AUBURN UNIVERSITY

AUBURN, ALABAMA

DTIC
ELECTE
JUN 10 1980

JUN 10 1980

80 6 9 111

D

LEVEL II

10

Final Technical Report
AU-EE-0022-Final

INVESTIGATION OF COMPLEX ANGLE PROCESSING
TO REDUCE INDUCED ANGLE POINTING ERRORS

Electrical Engineering
Auburn University

E. R. Graf
Project Leader

1 October 1979

Contract DAAK40-77-C-0022
U.S. Army Missile Command
Redstone Arsenal, Alabama

Accession For	
NTIS CS&I	<input checked="" type="checkbox"/>
DDC TAB	<input type="checkbox"/>
Unannounced	<input type="checkbox"/>
Justification	<input type="checkbox"/>
By <u>Per Ltr. on file</u>	
Distribution/	
Availability Codes	
Dist.	Avail and/or special
A	

DISTRIBUTION STATEMENT
Approved for public release
Distribution Unlimited

DTIC
ELECTE
S JUN 10 1980 **D**
D

4638

100

INVESTIGATION OF COMPLEX ANGLE PROCESSING
TO REDUCE INDUCED ANGLE POINTING ERRORS

by

David G. Burks and Edward R. Graf

FOREWARD

This is the final technical report of a study conducted by the Electrical Engineering Department under the auspices of the Engineering Experiment Station of Auburn University. This report is submitted toward fulfillment of Contract DAAK40-77-C-0022, granted to the Engineering Experiment Station by the U.S. Army Missile Command, Redstone Arsenal, Alabama.

INVESTIGATION OF COMPLEX ANGLE PROCESSING TO REDUCE INDUCED ANGLE POINTING ERRORS

David G. Burks and Edward R. Graf

Abstract

This work is an analysis of the effect of a tangent ogive radome on the pointing accuracy of a monopulse radar that employs an aperture antenna. The radar is assumed to be operating in the receive mode and the incident fields at the antenna are found by a ray-tracing procedure. Rays that enter the antenna aperture by direct transmission through the radome and by single reflection from the radome interior are considered. The theory of monopulse radar and the transmission and reflection properties of planar dielectric slabs are presented first to form a background for the radome analysis.

Two orthogonal polarization states which can be combined to produce an arbitrarily polarized incident field are considered. The antenna can be scanned in two angular directions and radar pointing error is presented for both these angles as a function of antenna scan angle and polarization of the incident field. Throughout the work, comparison of two different radome wall designs is made in order to both illustrate the analytical techniques and to show the engineering trade-offs in radome design.

A method that can be used to compensate for radome-induced error is presented. Complex angle processing for the purpose of pointing angle reduction was investigated based upon the simulation described

above. It was concluded that the complex angle could not be uniquely related to radar pointing error, but rather appeared to correlate with phase-front curvature. This quantity is not considered useful for pointing error correction.

ACKNOWLEDGEMENTS

Special thanks are due to Mike Fahey of the U.S. Army Missile R & D Command for initially suggesting the topic of this research and for providing continued interest and support throughout.

I would like to thank the staff of the Antenna Laboratory at Texas Instruments, especially Phil Green and Don Purinton, for an extremely valuable introduction to radomes during the Summer that I was employed there before beginning this work.

Table of Contents

LIST OF FIGURESviii
LIST OF TABLESxii
I. INTRODUCTION	1
II. FUNDAMENTAL FACTORS IN RADOME ANALYSIS	8
Monopulse Radar	
Tangent Ogive Radome Geometry	
Transmission and Reflection Properties of Planar Dielectric Slabs	
Principles of Ray Tracing	
III. RADOME-INDUCED RADAR POINTING ERRORS	71
Concept of Pointing Error	
Wavefront Distortion Due to Transmission	
Wavefront Distortion Due to Internal Reflection	
Composite Wavefront Distortion	
Radar Response to Wavefront Distortion	
IV. RADOME-INDUCED RADAR POINTING ERROR CORRECTION156
Error Compensation	
Complex Indicated Angle and Wavefront Distortion	
V. CONCLUSIONS167
REFERENCES171
APPENDIX175

LIST OF FIGURES

2-1.	Interferometer Monopulse System	11
2-2.	Phasor Diagram of Interferometer Signals	14
2-3.	Interferometer Signals versus Incident Angle	16
2-4.	Parabolic Reflector Antenna System	19
2-5.	Fields of Parabolic Antenna and Sampling Source	27
2-6.	Normalized Antenna Pattern of Circular Aperture with Uniform and Cosine Illumination	31
2-7.	Normalized Antenna Pattern of Circular Aperture with Uniform Illumination and the Term $(1 + \cos \theta)$	33
2-8.	Sum and Difference Patterns of Circular Aperture with Uniform Illumination	35
2-9.	Sum and Difference Patterns of Circular Aperture with Cosine Illumination	36
2-10.	Tangent Ogive Geometry	39
2-11.	Dielectric Slab and Definition of Fields (Parallel Polarization)	44
2-12.	Reference Polarization Directions	53
2-13.	Transmission Coefficient of Lossless Dielectric Slab with Half-wavelength Thickness	57
2-14.	Reflection Coefficient of Lossless Dielectric Slab with Half-wavelength thickness	58
2-15.	Transmission Coefficient of Lossless Dielectric Slab with 75° Design Angle	59
2-16.	Reflection Coefficient of Lossless Dielectric Slab with 75° Design Angle	60

2-17.	Dielectric Slab and Offset Transmitted Rays	62
2-18.	Ray Offset versus Incident Angle for Dielectric Slabs with Various Permittivities	65
2-19.	Dielectric Slab and Reflected Rays	68
3-1.	Two Illustrations of Wavefront Distortion	73
3-2.	Tangent Plane Approximation of Radome Wall	76
3-3.	Outline of Tangent Ogive Radome with Ray to Aperture Center.	78
3-4.	Insertion Phase Delay of TE Polarized Field with 90° Incidence Angle	86
3-5.	Insertion Phase Delay of TE Polarized Field with 85° Incidence Angle	87
3-6.	Insertion Phase Delay of TE Polarized Field with 80° Incidence Angle	88
3-7.	Insertion Phase Delay of TE Polarized Field with 70° Incidence Angle	89
3-8.	Insertion Phase Delay of TE Polarized Field with 60° Incidence Angle	90
3-9.	Insertion Phase Delay of TM Polarized Field with 90° Incidence Angle	92
3-10.	Insertion Phase Delay of TM Polarized Field with 85° Incidence Angle	93
3-11.	Insertion Phase Delay of TM Polarized Field with 80° Incidence Angle	94
3-12.	Insertion Phase Delay of TM Polarized Field with 70° Incidence Angle	95
3-13.	Insertion Phase Delay of TM Polarized Field with 60° Incidence Angle	96
3-14.	Transmission Coefficients of Polyimide Quartz Wall Designed for 60°	98
3-15.	Insertion Phase Delay of TE Polarized Field Incident at 80° on Polyimide Quartz Radome	100

3-16.	Insertion Phase Delay of TM Polarized Field Incident at 80° on Polyimide Quartz Radome	101
3-17.	Outline of Tangent Ogive Radome Showing Both Scan Angles and the Polarization Angle	102
3-18.	Insertion Phase Delay of 22.5° Polarized Field Incident at 80° on Polyimide Quartz Radome	104
3-19.	Insertion Phase Delay of 45° Polarized Field Incident at 80° on Polyimide Quartz Radome	105
3-20.	Insertion Phase Delay of 67.5° Polarized Field Incident at 80° on Polyimide Quartz Radome	106
3-21.	Outline of Tangent Ogive Radome Showing Internal Reflection	108
3-22.	Magnitude of Internal Reflected, TE Polarized Field with 70° Incidence Angle	115
3-23.	Magnitude of Internal Reflected, TE Polarized Field with 60° Incidence Angle	117
3-24.	Magnitude of Internal Reflected, TE Polarized Field with 50° Incidence Angle	118
3-25.	Magnitude of Internal Reflected, TE Polarized Field with 40° Incidence Angle	119
3-26.	Magnitude of Internal Reflected, TM Polarized Field with 70° Incidence Angle	121
3-27.	Magnitude of Internal Reflected, TM Polarized Field with 60° Incidence Angle	122
3-28.	Magnitude of Internal Reflected, TM Polarized Field with 50° Incidence Angle	123
3-29.	Magnitude of Internal Reflected, TM Polarized Field with 40° Incidence Angle	124
3-30.	Reflection Coefficients of Polyimide Quartz Wall Designed for 60°	126
3-31.	Magnitude of Internal Reflected, TE Polarized Field Incident at 70° on Polyimide Quartz Radome	127

3-32.	Magnitude of Internal Reflected, TE Polarized Field Incident at 60° on Polyimide Quartz Radome	128
3-33.	Magnitude of Internal Reflected, TE Polarized Field Incident at 50° on Polyimide Quartz Radome	129
3-34.	In-Plane Radar Pointing Error for Radome with 75° Wall Design and Uniform Aperture Illumination Showing Effect of Internal Reflection	141
3-35.	In-Plane Radar Pointing Error for Polyimide Quartz Radome with 60° Wall Design and Uniform Aperture Illumination Showing Effect of Internal Reflection	143
3-36.	In-Plane Radar Pointing Error for Radome with 75° Wall Design Illustrating Effect of Aperture Illumination Function	146
3-37.	In-Plane Radar Pointing Error for Polyimide Quartz Radome with 60° Wall Design Illustrating Effect of Aperture Illumination Function	147
3-38.	In-Plane Radar Pointing Error for Radome with 75° Wall Design and Various Incidence Polarization	149
3-39.	In-Plane Radar Pointing Error for Radome with 60° Wall Design and Various Incident Polarization	150
3-40.	Cross-Plane Radar Pointing Error for Radome with 75° Wall Design and Various Incident Polarization	152
3-41.	Cross-Plane Radar Pointing Error for Radome with 60° Wall Design and Various Incident Polarization	153
4-1.	Remaining In-Plane Radar Pointing Error After Compensation .	159

LIST OF TABLES

2-1. Classification of Dielectric Slab Fields	45
---	----

I. INTRODUCTION

The Institute of Electrical and Electronics Engineers gives the following definition [1]

RADOME. An enclosure for protecting an antenna from the harmful effects of its physical environment, generally intended to leave the electrical performance of the antenna unaffected.

Skolnik [2] divides radomes into these two major classifications, based on application and geometrical constraints: ground-based radomes and air-borne radomes. This study deals with radomes used on high-speed missiles which require a high degree of streamlining. Streamlining places severe constraints on the geometry of the radome and the radome material, which must withstand the temperature, pressure, and possibly rain or lightning encountered during high-speed flight. The antenna considered here is part of a radar system that provides information concerning target position and velocity to the guidance system of the missile. The radome may be considered a "necessary evil" because it has no beneficial effects on the performance of the radar but it is essential for protection of the antenna and for good flight characteristics of the missile. Of particular interest is the angular pointing error of the radar. This study is addressed mainly at that problem.

Airborne radomes first had extensive application on aircraft in World War II. Many design criteria and construction requirements

were formulated during this period. Much of this work in the United States and England is summarized in a volume of the MIT Radiation Laboratory Series [3]. In another volume [4] of the same series, radomes are discussed in conjunction with antenna installation problems. These two works list the essential characteristics of radome behavior and contain references to most of the wartime work.

All early radome work relies on ray tracing to obtain the electromagnetic energy reflected from or transmitted through the radome wall. This method was extended by Tricoles [5] who treated the receiving problem by tracing rays through the radome to a receiving aperture, but then obtained the antenna voltage by an empirical method based on aperture response to Huygen's sources. In a later paper [6] he used the same methods to obtain the transmittance of an axially symmetric missile radome. Each of these papers indicate that scattering from the radome vertex may be responsible for some of the measured radome behavior, and the second paper includes a crude approximation of this scattering.

Analysis of radome effects on antenna performance has been carried out for both transmitting and receiving antennas. The most frequently calculated antenna parameter in radome analysis is the far-field antenna pattern. Paris [7] has presented a technique for determining the transmitting antenna pattern of a horn antenna covered by an aircraft radome. His procedure is based on calculating the near-fields incident on the radome by using a previously developed aperture integration program [8], treating the incident fields as local plane waves, applying

plane-wave transmission coefficients, and then treating the fields exterior to the radome as equivalent sources of the radiated fields. A similar approach is taken by Wu and Rudduck [9] to obtain transmitting boresight errors for a circular aperture behind an ogive radome. They simplify the determination of the near fields incident on the radome by expressing these fields in a plane wave spectrum. For the uniformly illuminated circular aperture they consider, this results in an analytic expression for the near fields.

Since virtually all radome work has military application, few results of development and testing appear in the open literature. Most dissemination of radome information has been through a series of symposia begun in the mid-1950's under the title of either Radome Symposium or Symposium on Electromagnetic Windows. These symposia were originally sponsored jointly by Ohio State University and the U.S. Air Force and later by the Georgia Institute of Technology and the U.S. Air Force. In recent years the Georgia Institute of Technology has been the host and sponsor of the symposium. The proceedings of these symposia provide an indication of the work performed in the radome area, but due to the unavailability of the proceedings, and the abbreviated nature of the papers in them, they provide little concrete information for other researchers to draw upon.

The importance of radomes in both radar and antenna systems is accented by the inclusion of full chapters on radome design and characteristics in a major radar handbook [10] and a major antenna handbook [11].

The most extensive treatment of radomes is contained in the two volume report edited by Tice and Walton [12]. This report was intended to survey and summarize all of the radome work done up to that time. The report covers all aspects of radome design and testing, both electrical and mechanical. An extensive bibliography is included with references to both the open and classified literature. It is unfortunate that these volumes are not widely available due to their restricted circulation.

More recently, an entire handbook has been devoted to radome research [13]. This volume mainly treats materials, but there are chapters on electrical and operational considerations and a historical introduction. A report on radome design has also been prepared for NATO [14]. This report contains an excellent summary of how environmental, structural, electrical, and material considerations are combined in successful radome design. A subsequent NATO report [15] gives consideration to radome materials.

Simply stated, the radome problem is to find the voltage in the antenna feed line when a plane wave is incident on the radome. An exact solution of the radome problem is extremely difficult. The reasons for this are the complicated geometry of the problem, the boundary conditions which are imposed on the fields, and the large size of the structures as measured in wavelengths at the operating frequency.

The response of an aperture antenna may be determined from the fields incident on the antenna and the known characteristics of the antenna. The radome problem can thus be considered as that of finding the incident fields at the antenna in the presence of the

radome and the antenna. The incident fields at the antenna are composed of two distinct parts: the fields passing directly through the radome to the antenna and the fields that are scattered from the various objects near the antenna including the radome, metal tip, support structure and various feed structures on the antenna. The second category implicitly includes multiple scattering between any combination of the mentioned objects. An exact solution to the radome problem would consider all of these phenomena simultaneously by obtaining a solution to the electromagnetic field equations that would satisfy the boundary conditions at all surfaces of material discontinuity. Such a problem could be formulated in terms of integral equations for the tangential field components over a closed surface surrounding the antenna. The complicated form of the boundary conditions and the typically large electrical size of the structures have made exact techniques intractable and approximate solutions must be sought.

As previously mentioned, the response of a given antenna may be determined from the incident fields. The importance of radome effects should thus be ordered according to the influence on the incident fields at the antenna and an approximate analysis will consider only the most important of these effects. A primary consideration is the effect of the radome wall on the part of the incident field directly incident on the aperture. A well-designed radome will be highly transparent and this component will constitute by far the largest amount of energy incident on the aperture. Since

the radome wall is a curved surface with a transmission coefficient that varies with angle of incidence and polarization, the effect of the radome wall on the direct wave will be attenuation, depolarization and phase shift.

Of secondary priority is the incident field component that is singly reflected from the internal radome wall. This component may be quite significant at angles of incidence several degrees off bore-sight where specular reflection from the radome wall into the aperture is favorable.

Most airborne radomes designed for high-speed flight will be equipped with a metal tip to increase the erosion resistance of the radome. This tip is a source of indirect scatter at all angles of incidence. The support structure behind the antenna proper is thought to contribute little to the antenna voltage, since the feed is shielded by the aperture and a well-designed feed will have little spillover at the aperture. However, the structure behind the antenna can contribute to scatter back to the radome and in turn to the aperture: multiple scatter. Also multiple scatter can occur from the feed and its support structure.

The emphasis of this study is on the analysis of existing radomes as opposed to design of radomes having desired specifications. Of primary interest is the prediction of the pointing error of a monopulse radar operated in the radome. For the type radomes of interest, the transmission properties of the radome wall and reflection from the internal wall are considered to be the major

contributors to pointing error with the first predominating at small gimbal angles and the latter at angles well off the radome axis.

Radar pointing error can be a significant limitation to the accuracy of missile guidance systems. Also, the rate of change of pointing error with aspect angle, commonly called boresight error slope, will influence the radar's measurement of target angular velocity. The analysis performed in this work is directed toward the prediction of these sources of error in order to determine their impact on missile guidance and to evaluate methods for error compensation.

This work is organized to consider the fundamental elements of radome, antenna, and radar analysis separately. This is done in the following chapter. The third chapter contains an analysis of these items as a system with primary emphasis on prediction of angular pointing errors. Methods to compensate for angular errors are the topic of Chapter IV.

II. FUNDAMENTAL FACTORS IN RADOME ANALYSIS

This chapter may be considered a survey of the basic information needed for radome analysis. The approach taken here is to examine the subsystems encountered in the radome-radar problem and some of the models used to obtain tractable solutions to realistic problems. The first section in this chapter deals with the theory of monopulse radar operating ideally without radome, signal distortion, or noise. The second section introduces the radomes that will be considered in this work. A discussion of tangent ogive geometry is presented. Next are sections on the transmission and reflection properties of planar slabs and the technique of ray tracing. These basic optical methods will be used to model the local properties of the radome surface. The final section of this chapter discusses ray tracing which forms the basis for the treatment of propagation within the radome.

MONOPULSE RADAR

Monopulse is a technique for obtaining target direction information from a single radar return, hence the origin of the term. The theory of monopulse operation is well known and discussed in many introductory radar books such as Skolnik [15] and Barton [17]. The most definitive treatment of the mathematical theory of monopulse and the underlying principles is Rhodes early monograph [18]. A recent volume

[19] edited by Barton contains reprints of many of the key papers on monopulse and is recommended reading for anyone wishing a historical perspective on the developments in this area.

This section is designed to serve as an introduction to monopulse operation under ideal conditions and to form a foundation for the later analysis of a monopulse system operating in an environment containing a radome. In the main body of this work it will be shown that, in general, a radome introduces spatial distortion into the wavefront incident on the receiving antenna. This violates one of the key assumptions concerning the received wave and is a source of radar pointing error.

Fundamental to the theory of monopulse is the assumption that the wave scattered from the radar target is a uniform plane wave over the receiving antenna or that the antenna is in the far-field of the target. When this assumption is satisfied the response of a receiving antenna is completely described by its far-field antenna pattern. The far-field antenna pattern of a radar antenna is easily measured and analytic expressions for such patterns are not difficult to obtain.

The first basic problem addressed in this study is the determination of a method to obtain the response of a monopulse system to a non-planar non-uniform wave. This problem has been addressed in the literature in studies on radar response to glint [20], multipath [21], and unresolved targets [22]. The approach taken in each of these studies, however, does not answer the basic question raised here. When analyzing

the above-mentioned sources of a distorted wavefront, the approach taken has been to decompose the target into smaller parts, each of which scatters a wave that is uniform and planar at the receiving aperture. Hence, the principle of superposition can be applied to obtain the monopulse response in these environments. Treating a general wavefront as a superposition of plane waves traveling in different directions is a well-documented analytical technique, often known as plane-wave spectrum analysis [23].

The resolution of a received wave that is distorted by a radome into a plane-wave spectrum representation is a difficult problem and is not justified if only the monopulse response is desired. Techniques are presented in this section for obtaining the monopulse response directly from the fields incident on the antenna, be they planar, distorted, or whatever. However, a most elementary monopulse system in the form of an interferometer is examined first. This provides an easy way to visualize how monopulse works. Later, the receiving properties of the more practical parabolic reflector antenna are presented.

Consider a receiving antenna system made up of two elements separated by a distance D as shown in Figure 2-1. Assume a time-harmonic plane wave traveling in free space is incident on the receiving elements. Here and throughout this work the time variation of all time-varying quantities is assumed to be $e^{j\omega t}$ where $j = \sqrt{-1}$, ω is the frequency in rad/s, and t is the time in seconds. Furthermore, the time variation will usually be suppressed and the conventions of ac circuit

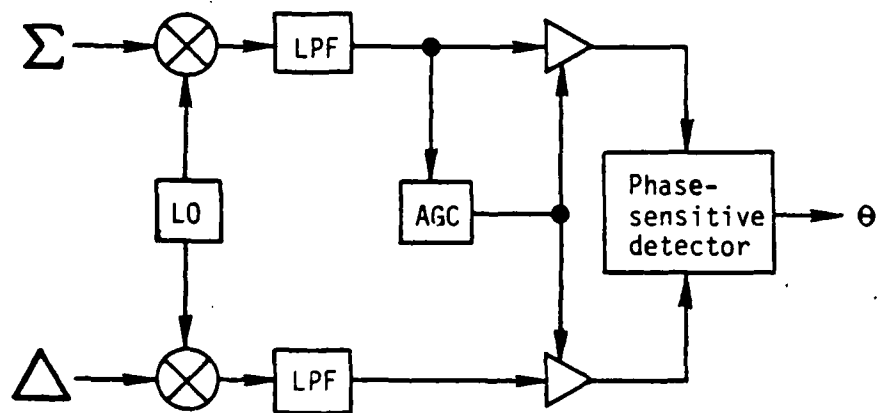
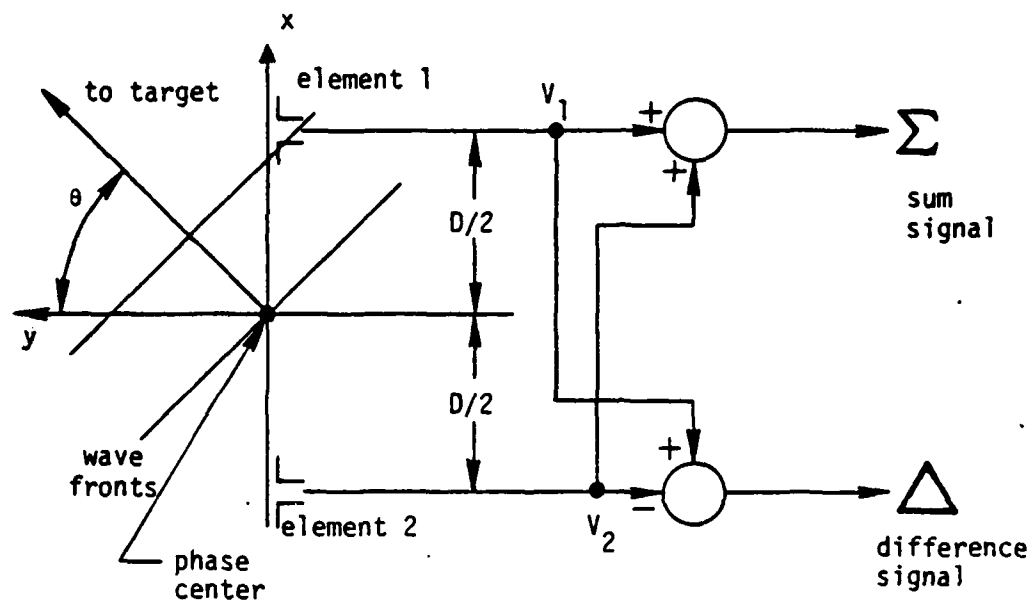


Figure 2-1. Interferometer Monopulse System.

analysis, or phasor notation, will be employed. Thus the electric field amplitude of the incident field, E^i , is given by

$$E^i = E_0^i e^{jk(x \sin \theta + y \cos \theta)} \quad (2.1)$$

where E_0^i is the magnitude of the field, k is the propagation constant given by $2\pi/\lambda$, λ is the wavelength of the wave, and θ is the incident angle as indicated. The phase reference for the incident wave and the antenna system is taken to be the origin.

Induced potentials that are proportional to the incident electric field will exist across the terminals of the receiving elements. These signals can be written as

$$V_1 = V_0 e^{jk \frac{D}{2} \sin \theta} \quad (2.2)$$

at element 1 and

$$V_2 = V_0 e^{-jk \frac{D}{2} \sin \theta} \quad (2.3)$$

at element 2 where V_0 is the voltage magnitude which is identical for element 1 and 2.

The distinguishing feature of monopulse is the method of combining V_1 and V_2 so that the angle of incidence can be determined. This is done by adding and subtracting the antenna voltages to form two new signals known as sum and difference signals. Thus the sum signal, Σ , is given by

$$\Sigma = V_1 + V_2 \quad (2.4)$$

and the difference signal, Δ , is given by

$$\Delta = V_1 - V_2. \quad (2.5)$$

The method of forming these signals is shown in Figure 2-1.

It is convenient to introduce a new variable to represent the phase of V_1 and V_2 as given in (2.2) and (2.3). The symbol, u , will be used to denote this phase angle or,

$$u = k \frac{D}{2} \sin \theta = \frac{\pi D}{\lambda} \sin \theta ; \quad (2.6)$$

where it is noted that u contains the element spacing normalized to the wavelength. Using the variable u and substituting (2.2) and (2.3) into (2.4) and (2.5), the sum and difference signals can be written as

$$\Sigma = V_0 e^{ju} + V_0 e^{-ju} , \quad (2.7)$$

$$\Delta = V_0 e^{ju} - V_0 e^{-ju} , \quad (2.8)$$

or by using Euler's identity,

$$\Sigma = 2V_0 \cos(u) , \quad (2.9)$$

$$\Delta = j2V_0 \sin(u) , \quad (2.10)$$

Signals V_1 and V_2 together with Σ and Δ are conveniently displayed on a phasor diagram as shown in Figure 2-2. It should be pointed out that the choice of the origin as the phase center causes Σ to be purely real, and Δ is in phase quadrature with Σ .

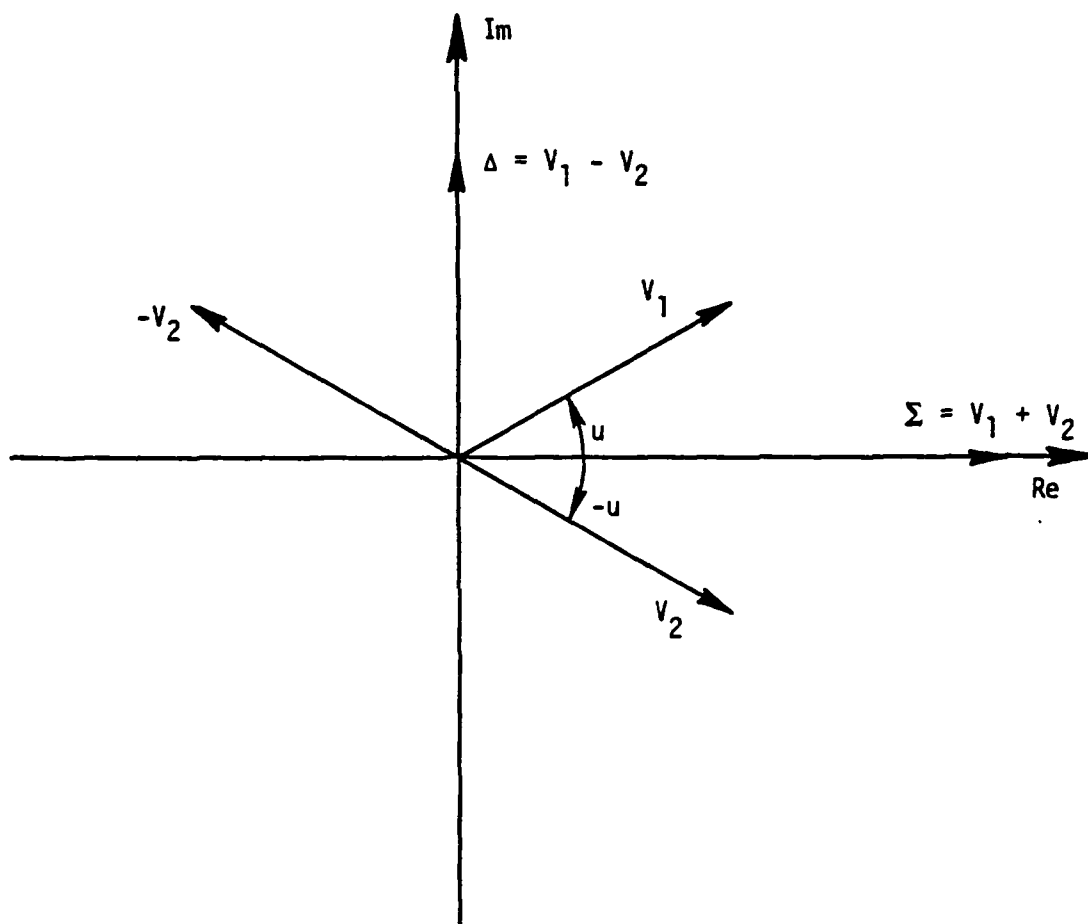


Figure 2-2. Phasor Diagram of Interferometer Signals.

Incidence angle detection is accomplished by taking the real part of the ratio of $-j\Delta$ to Σ or,

$$\theta \propto \operatorname{Re} \left\{ \frac{-j\Delta}{\Sigma} \right\} = \frac{2V_0 \sin(u)}{2V_0 \cos(u)} = \tan(u) \quad (2.11)$$

The ratio $\operatorname{Re}\{-j\Delta/\Sigma\}$ is known as the monopulse ratio and is the output signal of the monopulse system. Figure 2-3 is a plot of the sum and difference response and the monopulse ratio. For tracking radars, the angle of incidence will be near the antenna axis, and thus u will be small. Using the small angle approximation, $\tan(\alpha) \approx \alpha$, and the definition of u , equation (2-11) can be written as

$$\operatorname{Re} \left\{ \frac{-j\Delta}{\Sigma} \right\} \approx u = \frac{\pi D}{\lambda} \sin \theta \quad (2.12)$$

Again using a small angle approximation ($\sin(\alpha) \approx \alpha$), (2.12) can be solved for θ ,

$$\theta \approx \left[\frac{\pi D}{\lambda} \right]^{-1} \operatorname{Re} \left\{ \frac{-j\Delta}{\Sigma} \right\} \quad (2.13)$$

Thus, by measuring the monopulse ratio and multiplying by a constant, the angle to the radar target may be determined. This information may be fed to a gimbal system that repositions the antenna so that a moving target's position is continually tracked.

Some comments are in order concerning this monopulse system. First, the system will have zero output when the amplitude and phase of the voltages at elements 1 and 2 are identical. If the

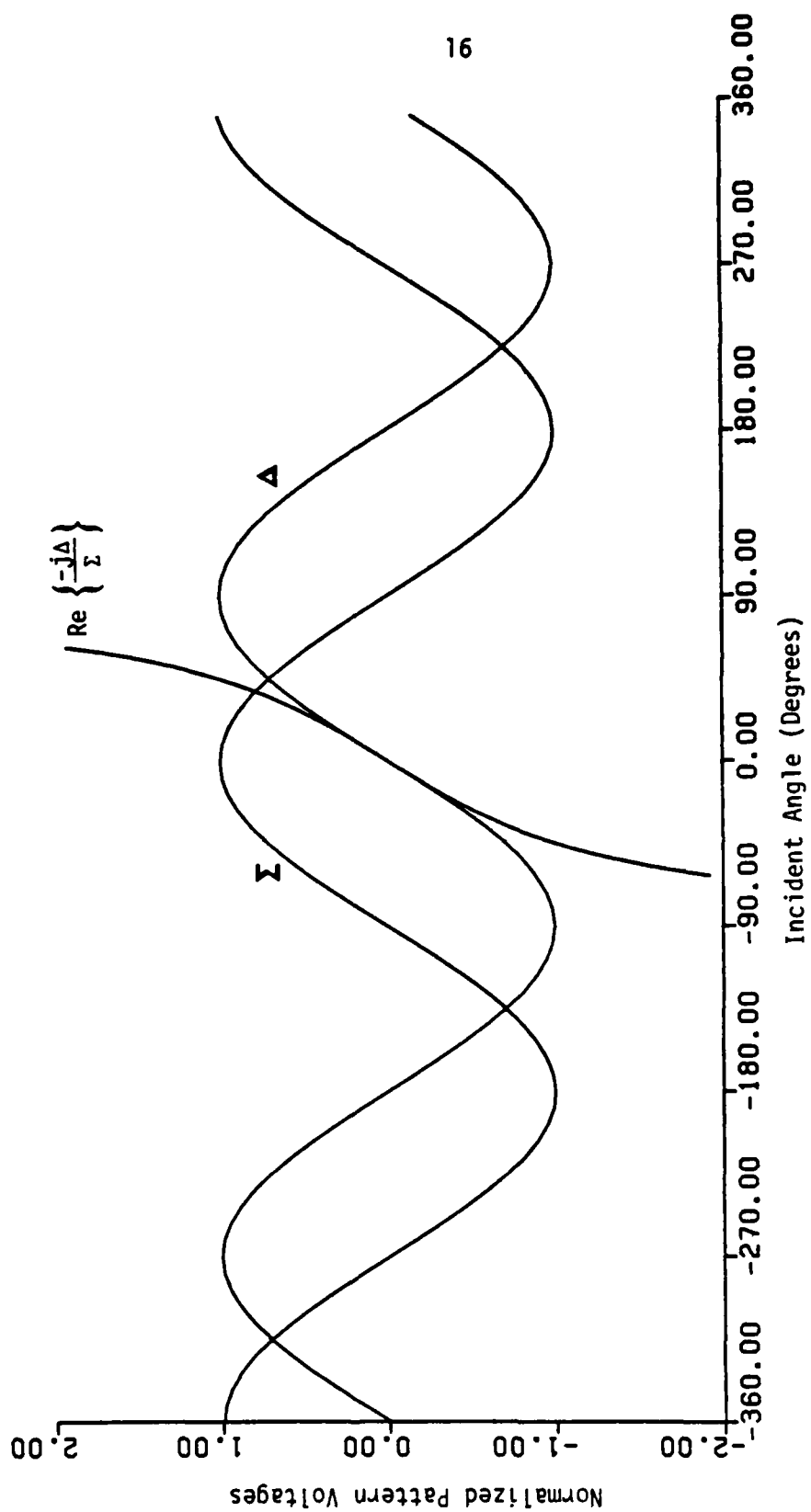


Figure 2-3. Interferometer Signals versus Incident Angle.

phase of the signals at elements 1 and 2 are different, an output signal is produced that is linearly (for small angles) related to the angle of incidence of a plane wave that would produce the element voltages. In this respect the two-element interferometer monopulse system is identical to the method used by Sims and Graf [24] for determining wavefront distortion due to glint. Their method involved sampling the wavefront at two points separated by a distance representing the receiving aperture diameter and using the phase of the wave at these points to make a linear approximation of the wavefront across the receiving aperture. The angular difference between the normal to this wavefront and the true angle to the target was then defined as the radar pointing error due to glint.

Note also that the sign of the incidence angle is determined by the phase of the difference channel with respect to the sum channel. When the incidence angle is positive, Δ leads Σ by 90° in phase, and lags Σ by 90° when the incidence angle is negative. The phase-sensitive detector shown in Figure 2-1 indicates the sign of the incidence angle by measuring this phase relationship. One final comment concerning monopulse systems is that incidence angle determination does not involve the amplitude of the incident wave. This is because incident angle determination occurs in the form of a ratio. Of course the signal levels must be significantly above the noise level for reliable operation and this is assumed throughout.

Next the receiving properties of a monopulse system employing a parabolic reflector antenna are examined. The parabolic reflector is a commonly

used antenna and has received considerable attention in the literature [25, 26]. As previously mentioned, almost all antenna analysis treats the transmitting situation and obtains the fields at points far removed from the radiating structure. The receiving antenna has been treated in general [27], but little attention has been given to the aperture receiving antenna. The purpose of the remainder of this section is to derive expressions for the response of a monopulse receiving antenna excited by an arbitrary (non-planar, non-uniform, randomly polarized, but time-harmonic) incident field. The results are applicable to all aperture antennas.

The Lorentz reciprocity theorem will be employed to find the receiving characteristics of the parabolic reflector antenna. In order to use this theorem, the behavior of the antenna in the transmitting mode must be known. This is most easily done through the use of the equivalence principle, that is, by finding a set of sources which produce the same fields as are produced by the antenna in the region of interest. As will be seen, the equivalent sources play an important role in the monopulse receiving system.

The parabolic reflector antenna system is composed of two principal parts, a feed antenna and a reflecting surface in the shape of a paraboloid of revolution. As shown in Figure 2-4, the feed antenna, the primary radiator, is located at the focus of the parabola. The spherical wavefront leaving the feed antenna will be reflected at the parabola and become a planar wavefront traveling parallel to the antenna axis.

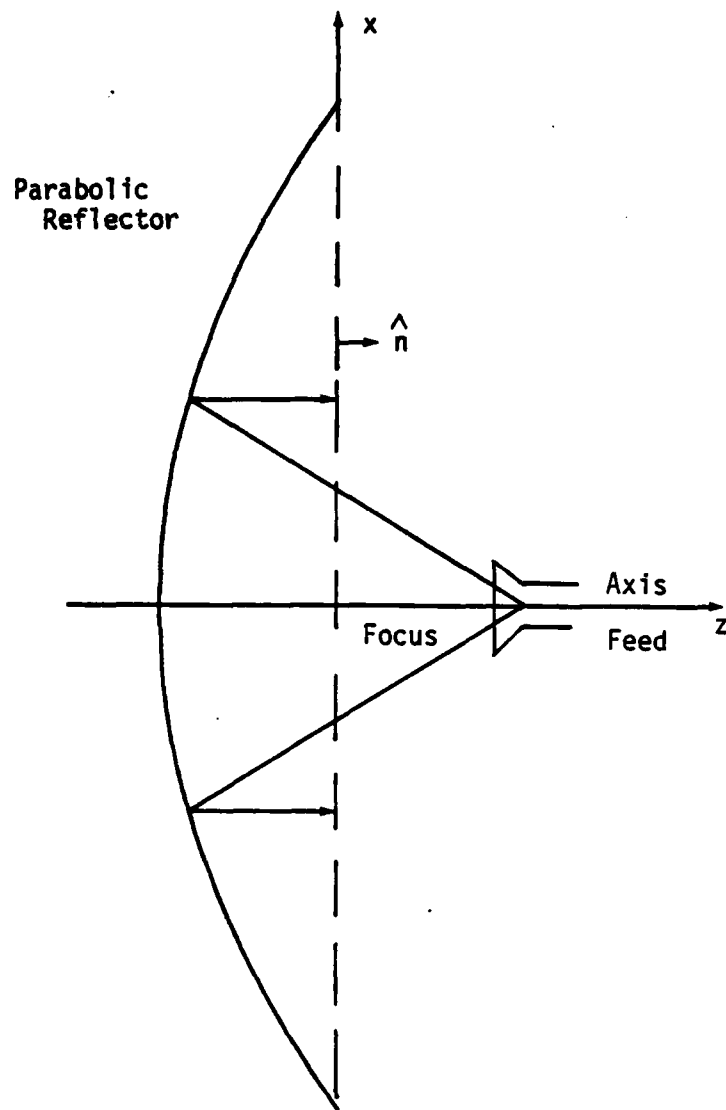


Figure 2-4. Parabolic Reflector Antenna System

The planar circular area that is perpendicular to the antenna axis and has its perimeter at the reflector's edge is called the aperture plane. The fields over the aperture plane can be used to determine the transmitting and receiving characteristics of the antenna. This is shown first for the transmitting case where the fields produced by the antenna in region $z > 0$ are to be found.

The region $z > 0$ is source free, so by the uniqueness theorem [28] the fields in this region are uniquely related to the tangential field components over a closed surface that contains the actual sources. It is convenient to enclose the sources by the surface formed by the xy -plane and a large hemisphere with center at the origin. The hemisphere may be thought of as being of infinite radius or of finite radius but large enough so that the fields over the hemisphere are negligible. Thus the fields in the region $z > 0$ are uniquely related to the tangential field components over the xy -plane.

The electric and magnetic field intensity produced by the antenna will be denoted by \vec{E}^a and \vec{H}^a , and it will be assumed that \vec{E}^a and \vec{H}^a are zero in the region $z < 0$, that is, behind the reflector. This will occur when the feed does not produce fields in this region (no spill-over in the terms of antenna engineers), and when scattering from the reflector edge is neglected. Thus, all the antenna fields in the xy -plane are confined to the aperture plane.

The equivalence principle [29] will next be used to further simplify the antenna analysis. As guaranteed by the uniqueness theorem, the

fields in the region $z > 0$ are now completely determined by the tangential field components in the aperture plane. According to the equivalence principle, these same aperture fields may be supported by equivalent surface currents, \mathbf{J}_s^a and \mathbf{M}_s^a , in the aperture plane, and all the fields in the region $z < 0$ may be set to zero. The equivalent currents are found from,

$$\mathbf{J}_s^a = \hat{n} \times \mathbf{H}^a, \quad (2.14)$$

and

$$\mathbf{M}_s^a = \mathbf{E}^a \times \hat{n}, \quad (2.15)$$

where \mathbf{E}^a and \mathbf{H}^a are the fields produced by the antenna and \hat{n} is a unit vector normal to the aperture plane as shown in Figure 2-4.

The equivalent surface currents given by (2.14) and (2.15) follow from the electromagnetic boundary condition equations which state that discontinuities in tangential field components are associated with surface-current densities. At a smooth interface separating regions labeled 1 and 2 these equations are:

$$\mathbf{J}_s = \hat{n} \times [\mathbf{H}_1 - \mathbf{H}_2], \quad (2.16)$$

$$\mathbf{M}_s = [\mathbf{E}_1 - \mathbf{E}_2] \times \hat{n}, \quad (2.17)$$

where subscripts 1 and 2 indicate the fields at the interface in region 1 and 2 respectively, \mathbf{E} represents the electric field intensity, \mathbf{H} the magnetic field intensity, \mathbf{J}_s is the electric surface-current density, \mathbf{M}_s is the magnetic surface-current density, and \hat{n} is a unit vector normal

to the interface directed into region 1. Thus (2.16) states that electric surface-current densities are associated with discontinuities in tangential magnetic fields and (2.17) states that magnetic surface-current densities are associated with discontinuities in the tangential electric fields.

By choosing region 2 to be the region $z < 0$ and by setting all the fields in this region to zero, (2.14) and (2.15) are seen to follow from (2.16) and (2.17). The fields in the region $z > 0$ are the same as before but now they are supported by the "equivalent currents", \bar{J}_s and \bar{M}_s . Thus the entire problem of finding the antenna fields is reduced to the problem of finding the fields of the currents given by (2.14) and (2.15).

It should be noted that the above treatment of the reflector antenna results in the same formulation as the classical optics problem of diffraction from a circular aperture in a conducting screen. All such aperture problems may be solved by the same method based on the equivalence principle.

A comment concerning the antenna feed is in order before proceeding. As seen in Figure 2-4, part of the field radiated by the feed will be reflected back to the feed and interact with it. This is often referred to as aperture blockage and may have a significant effect on the performance of the antenna system, particularly when the size of the feed is an appreciable part of the reflector size. Consideration of aperture blockage is beyond the scope of this work and it will be assumed that the antenna system can be represented completely by the equivalent currents as previously discussed.

There are several ways of determining the fields of the antenna from the equivalent currents. These include direct integration, use of potential functions, and the plane-wave-spectrum technique. The fields radiated by the antenna will not be found here since it is the antenna's receiving properties that are of greatest interest. These receiving characteristics can be derived from the Lorentz reciprocity theorem.

The Lorentz reciprocity theorem, which follows directly from Maxwell's equations, is a way of relating two sets of sources and their fields. An integral form of this theorem is given by [30],

$$\int_{\text{vol}} (\vec{E}^a \cdot \vec{J}^b - \vec{H}^a \cdot \vec{M}^b) dv = \int_{\text{vol}} (\vec{E}^b \cdot \vec{J}^a - \vec{H}^b \cdot \vec{M}^a) dv \quad (2.18)$$

where superscripts indicate a set of sources and associated fields as used previously, and the integrations extend over all space. Rumsey [31] has given the name reaction to the relation between sources and fields expressed by either side of (2.18). The reciprocity theorem thus states that the reaction of the field a on source b is equal to the reaction of the field b on the source a.

In order to apply (2.18) to the receiving antenna problem the a source and field are chosen to be that of the equivalent currents representing the parabolic reflector antenna and the b source is chosen to be a point electric current element (dipole) given by,

$$\vec{J}^b = \vec{J}_0^b \delta(|\mathbf{R} - \mathbf{R}'|) \quad , \quad (2.19)$$

where J_0^b contains the magnitude and direction of the current element, \bar{R}' is a vector from the origin to the element's location, \bar{R} is the position vector ($\bar{R} = x\hat{x} + y\hat{y} + z\hat{z}$), and δ is the Dirac delta function. \bar{M}^b is set to zero.

Substituting (2.19) into the left-hand side of (2.18) and recognizing the sampling property of the Dirac delta function yields,

$$\int_{vol} \bar{E}^a \cdot J_0^b \delta(|\bar{R} - \bar{R}'|) dv = \bar{E}^a \cdot J_0^b \Big|_{\bar{R} = \bar{R}'} \quad (2.20)$$

If J_0^b is chosen to have unit amplitude and to be in the direction of \bar{E}^a then (2.20) is simply the magnitude of the electric field at the point dipole produced by the sources J^a and \bar{M}^a . From the right-hand side of (2.18), it is seen that the magnitude of E^a at \bar{R}' , as given by (2.20), is equivalent to the reaction of the fields of the unit-amplitude dipole on the equivalent currents of the parabolic antenna.

The behavior of a transmitting antenna at distances much greater than the antenna dimensions (in the far-field) is completely characterized by the electric field it radiates, due to the transverse nature of the radiated fields. The far-field response of a transmitting antenna, defined as the magnitude of the electric field, is obtained from (2.20) when $|\bar{R}'|$ is large. The response of the same antenna in the receiving mode, defined as the open-circuit voltage at the antenna terminals, is proportional to the right-hand side of (2.18) [31]. In the remainder of this section the receiving-mode response of the parabolic antenna is discussed.

The right-hand side of (2.18) can be rewritten using the aperture fields as given by (2.14) and (2.15) yielding,

$$\int_A \bar{E}^b \cdot (\mathbf{n} \times \bar{H}^a) - \bar{H}^b \cdot (\bar{E}^a \times \hat{\mathbf{n}}) ds, \quad (2.21)$$

where A indicates that the integration is only over the antenna aperture since the a currents are zero everywhere else. Throughout this study it is assumed that \bar{E}^a and \bar{H}^a are of constant phase and related like a plane wave in the aperture. For a linearly polarized antenna \bar{E}^a will have the same direction over the aperture and \bar{H}^a will also be uni-directional and at right angles to \bar{E}^a .

As an example, assume that \bar{E}^a in the aperture is given by,

$$\bar{E}^a = E_0^a \hat{x} \quad (2.22)$$

and \bar{H}^a is

$$\bar{H}^a = H_0^a \hat{y} = \frac{1}{\eta} E_0^a \hat{y} \quad (2.23)$$

where zero subscripts indicate magnitude. The second part of (2.23) is obtained from the plane-wave nature of \bar{E}^a and \bar{H}^a , and η is the intrinsic impedance of free space ($\eta = \sqrt{\mu/\epsilon}$). Figure 2-5(a) illustrates these aperture fields.

Substituting these a fields into (2.21) yields,

$$\int_A -\vec{E}^b \cdot \left(\frac{1}{\eta} \vec{E}_0^a \hat{x}\right) + \vec{H}^b \cdot (\vec{E}_0^a \hat{y}) ds, \quad (2.24)$$

where the cross products have been evaluated for $\hat{n} = \hat{z}$.

\vec{E}_0^a is common to both terms in (2.24) and can be factored to yield

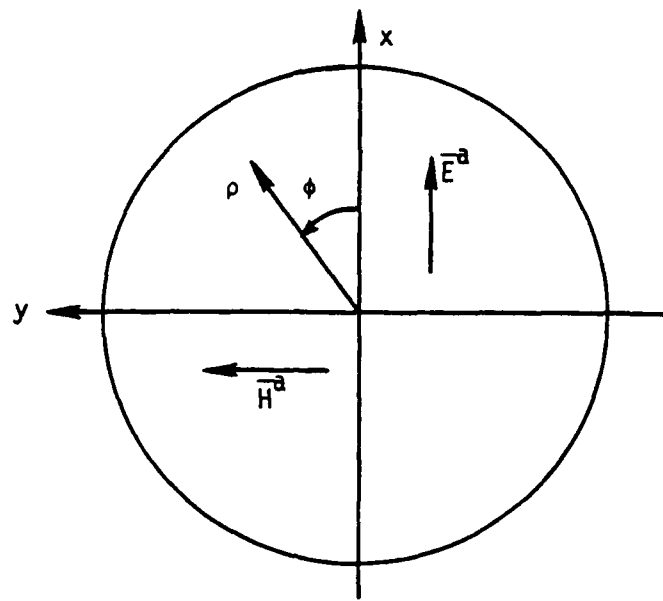
$$\int \vec{E}_0^a [\vec{H}^b \cdot \hat{y} - \frac{1}{\eta} \vec{E}^b \cdot \hat{x}] ds. \quad (2.25)$$

Thus it is seen that \vec{E}_0^a acts as a weighting function for the integration. Also, since \vec{E}_0^a has constant phase, it can be assumed purely real. By adjusting the variation of \vec{E}_0^a over the aperture, various antenna patterns may be obtained. In practice this is accomplished by design of the antenna feed.

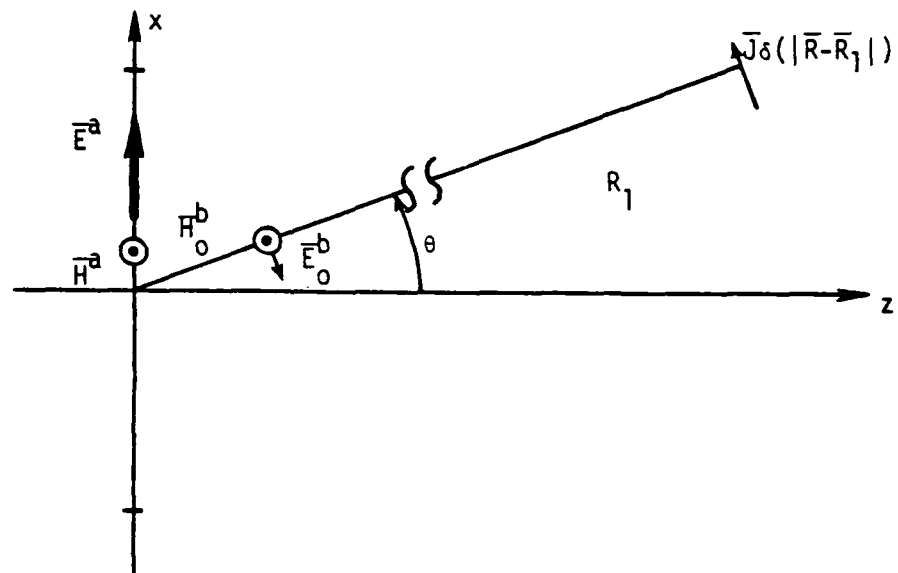
The importance of the form of \vec{E}_0^a will be emphasized by giving it the name aperture illumination function and using the symbol, g , for this function. The monopulse sum and difference patterns are produced by the proper aperture illumination functions. To see how this is accomplished it is first necessary to find the antenna response to an incident plane wave.

To obtain the antenna response, assume that a distant point dipole produces a field which is incident on the aperture as in Figure 2-5(b). This field, which is denoted by b , will be a uniform plane wave over the aperture and can be written as,

$$\vec{E}^b = \vec{E}_0^b e^{jk \sin \theta x} (-\cos \theta \hat{x} + \sin \theta \hat{z}) \quad (2.26)$$



(a) Aperture fields



(b) Plane wave incident on aperture

Figure 2-5. Fields of Parabolic Antenna and Sampling Source.

and

$$\vec{H}^b = \frac{E_0^b}{\eta} e^{jksin\theta x} (\hat{y}) \quad (2.27)$$

where E_0^b is the magnitude of the electric field.

Substituting (2.26) and (2.27) into (2.25), performing the dot products, and using the symbol for the aperture illumination function yields,

$$\int_A g \left[\frac{E_0^b}{\eta} + \frac{1}{\eta} E_0^b \cos \theta \right] e^{jksin\theta x} ds \quad (2.28)$$

By removing the constants from the integral and making the substitution, $k_x = k \sin \theta$, (2.28) becomes,

$$\frac{1}{\eta} E_0^b (1 + \cos \theta) \int_A g e^{jk_x x} ds. \quad (2.29)$$

The integral in (2.29) is immediately recognized as a Fourier transform of F and expresses a well-known relation between the aperture illumination function and the far-field antenna pattern.

The integration in (2.29) is most easily performed in circular cylindrical coordinates for the circular aperture under discussion. Writing the integral completely, (2.29) becomes,

$$\frac{1}{\eta} E_0^b (1 + \cos \theta) \int_0^{2\pi} \int_0^{D/2} g(\rho, \phi) e^{jk_x \rho \cos \phi} \rho d\rho d\phi, \quad (2.30)$$

where the functional dependance of g is now shown and ρ and ϕ are the coordinates indicated in Figure 2-5. In order to normalize this expression as was done for the interferometer, the following variable change is introduced,

$$r = 2\rho/D, \quad (2.31)$$

$$u = \frac{\pi D}{\lambda} \sin\theta. \quad (2.32)$$

Using these variables, expression (2.30) is written

$$\frac{1}{\eta} E_0^b (1 + \cos\theta) \frac{D^2}{4} \int_0^{2\pi} \int_0^1 g(r, \phi) e^{j u r \cos\phi} r dr d\phi \quad (2.33)$$

where $g(r, \phi)$ replaces $g(\rho, \phi)$ according to (2.31).

As with the interferometer, an aperture antenna used with a monopulse system will have two far-field response patterns which are again called the sum and difference patterns. These patterns are determined by the aperture illumination function. The sum pattern is an even function of θ and the difference pattern is an odd function of θ . It has been shown that the far-field pattern of the aperture involves the Fourier transform of the aperture illumination function (2.29).

According to elementary Fourier transform theory [32], the transform of an even function is even and the transform of an odd function is odd. Thus the aperture illumination functions for the sum pattern will be even, and the aperture illumination function for the difference pattern will be an odd function of x .

In this study two commonly used sum-pattern aperture illumination functions will be considered. The first is uniform illumination, or

$$g(\rho, \phi) = 1, \rho < \frac{D}{2}. \quad (2.34)$$

This illumination is sometimes called ideal because it is constant to the edge of the aperture but zero outside. It would be impossible to create in practice due to the discontinuity in the fields at the aperture edge.

The second sum illumination function is tapered from the center of the aperture to the edge according to a cosine function,

$$g(\rho, \phi) = \cos\left(\frac{\pi\rho}{D}\right), \rho < \frac{D}{2}. \quad (2.35)$$

The integral part of (2.33) is called the aperture pattern. It will be shown that for large apertures the aperture pattern contains all the significant variation of (2.33) with θ . The aperture patterns for the two aperture illumination functions are shown in Figure 2-6. These patterns are normalized to their respective maxima and are plotted in dB versus u . It is noted that the tapered illumination function produces a wider main lobe but has lower side-lobe levels than the uniform illumination. These aperture patterns could be obtained analytically, by using a two-dimensional fast Fourier transform algorithm, or by numerical integration. Figure 2-6 and the remaining figures in this section were obtained using the numerical integration technique that is used to find the response of the antenna with radome.

Figure 2-6 may be regarded as an "universal" aperture pattern since the response for any size aperture, any wavelength, and any incidence

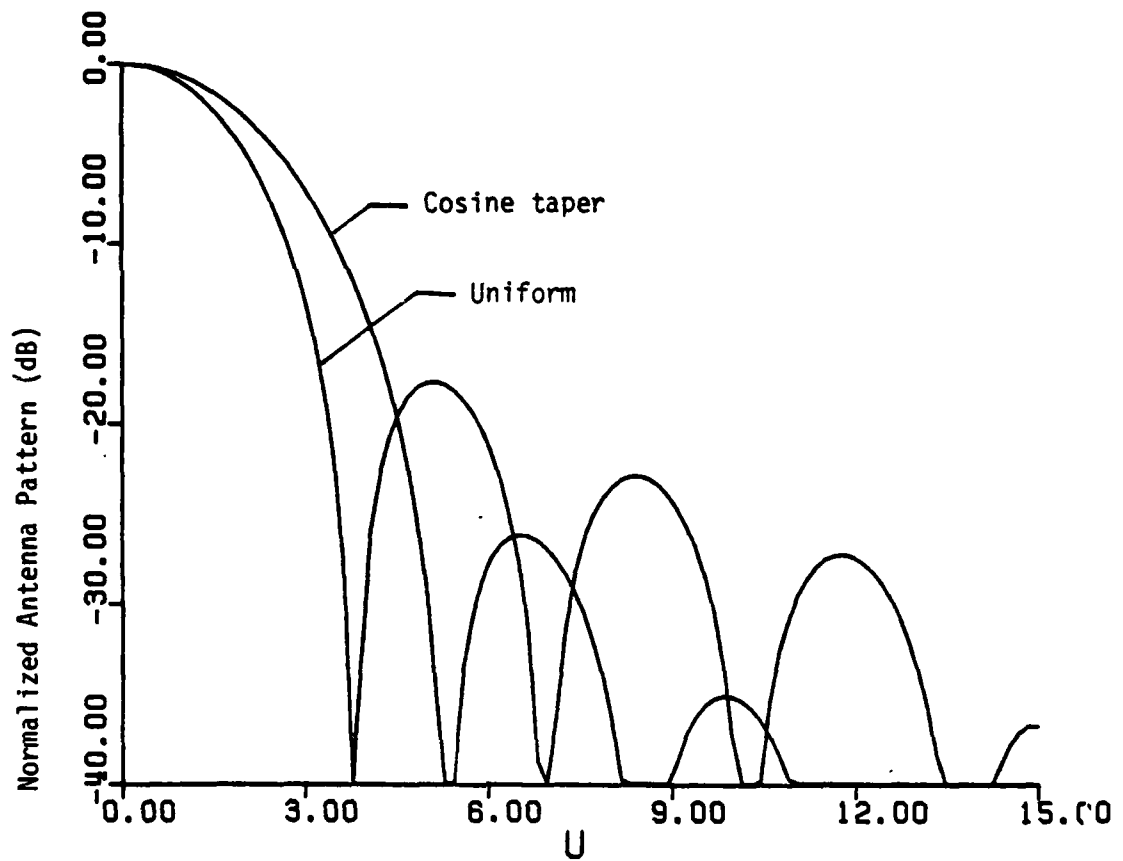


Figure 2-6. Normalized Antenna Pattern of Circular Aperture with Uniform and Cosine Illumination

angle can be looked up. This study is concerned with electrically large apertures, and as an example an aperture with a diameter of 8 wavelengths will be used. The statement that the aperture pattern contains the significant angular variation of the antenna response is now justified. The response function given by (2.33) is the product of two terms that vary with θ : the term $(1 + \cos\theta)$ and the aperture pattern. Figure 2-7 is a plot of these terms in dB versus incidence angle, θ . Each curve is normalized to its maxima. It is seen that the term $(1 + \cos\theta)$ is only 3dB down at $\theta = 65^\circ$ and a maximum of 6dB down at 90° , while the aperture pattern is greater than 30dB down for all angles greater than about 30° . Since the antenna response in dB is the sum of these two terms, little error is introduced by ignoring the $(1 + \cos\theta)$ term.

A method presented by Barton and Ward [33] will be used to obtain the difference pattern illumination functions. They note that the difference pattern of monopulse antennas resembles the derivative of the sum pattern. If this relation is taken to be exact, the difference illumination function, denoted by g_d , is related to the sum illumination function, g , by,

$$g_d(x,y) = \frac{2\pi x}{L_s} g(x,y) \quad , \quad (2.36)$$

where it is noted that g_d is the product of the sum illumination and the linear odd function, x ; L_s is a constant. Since g is even, g_d is odd.

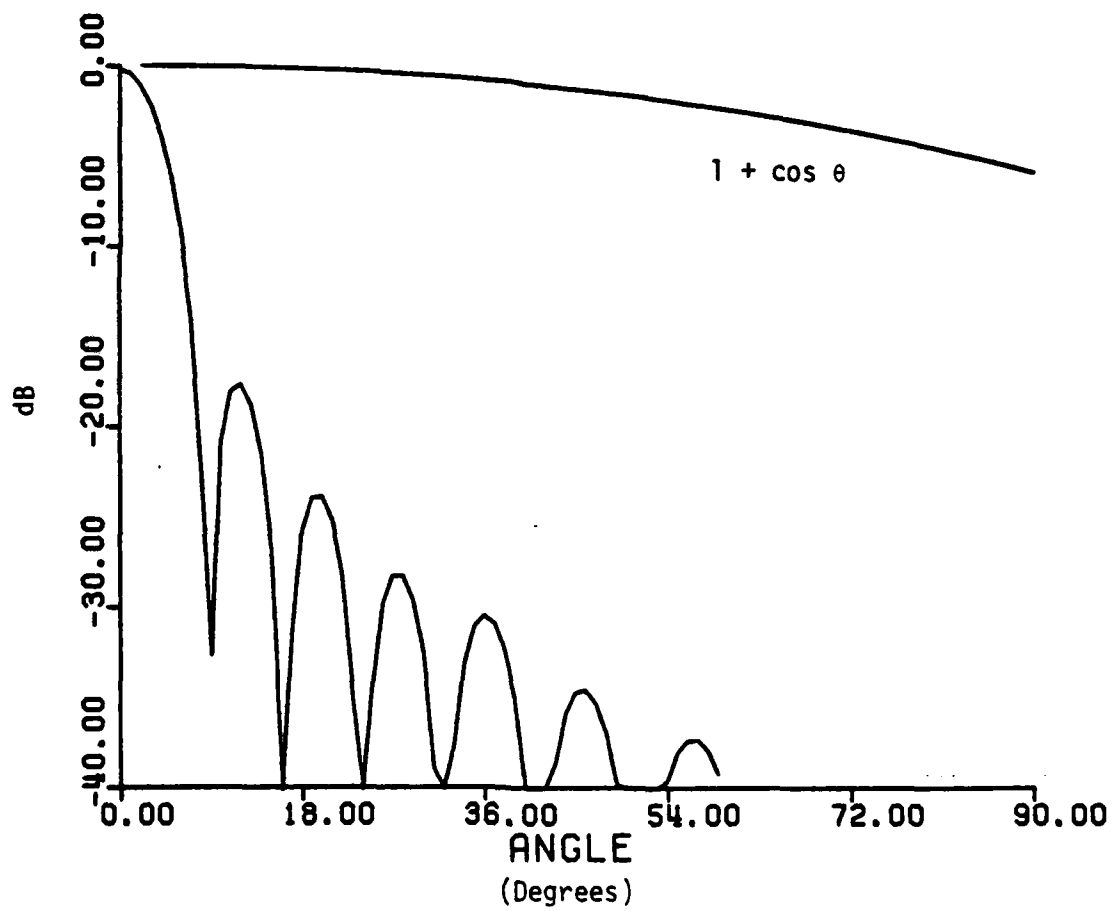


Figure 2-7. Normalized Antenna Pattern of Circular Aperture with Uniform Illumination and the Term $(1 + \cos \theta)$.

The constant, L_s , is the effective aperture illumination power width in the terminology of [33] and is given by

$$L_s = \left[\frac{\int_A (2\pi x)^2 |g(x,y)|^2 ds}{\int_A |g(x,y)|^2 ds} \right]^{1/2} \quad (2.37)$$

For the case of uniform illumination in the circular aperture, L_s is $D\pi/2$, and for cosine tapered illumination (2.37) yields $L_s = 1.071867D$.

When the difference illumination is defined by (2.36) with L_s given by (2.37), the sum and difference illumination functions contain equal power. This would be expected in a well-designed monopulse antenna.

Using (2.36) and the above constants, the difference illumination for uniform sum illumination is,

$$g_d = \frac{4x}{D} \quad , \quad \rho < \frac{D}{2} ; \quad (2.38)$$

and for cosine illumination is,

$$g_d = \frac{5.861962x}{D} \cos\left(\frac{\pi\rho}{D}\right) \quad , \quad \rho < \frac{D}{2} ; \quad (2.39)$$

where a mixed coordinate system is used for convenience.

The sum and difference illumination functions and the far-field response function of an 8λ diameter aperture are shown in Figure 2-8 for uniform illumination, and in Figure 2-9 for cosine tapered illumination. The response functions are again normalized to the maximum of the sum patterns, but are now shown with a linear ordinate scale.

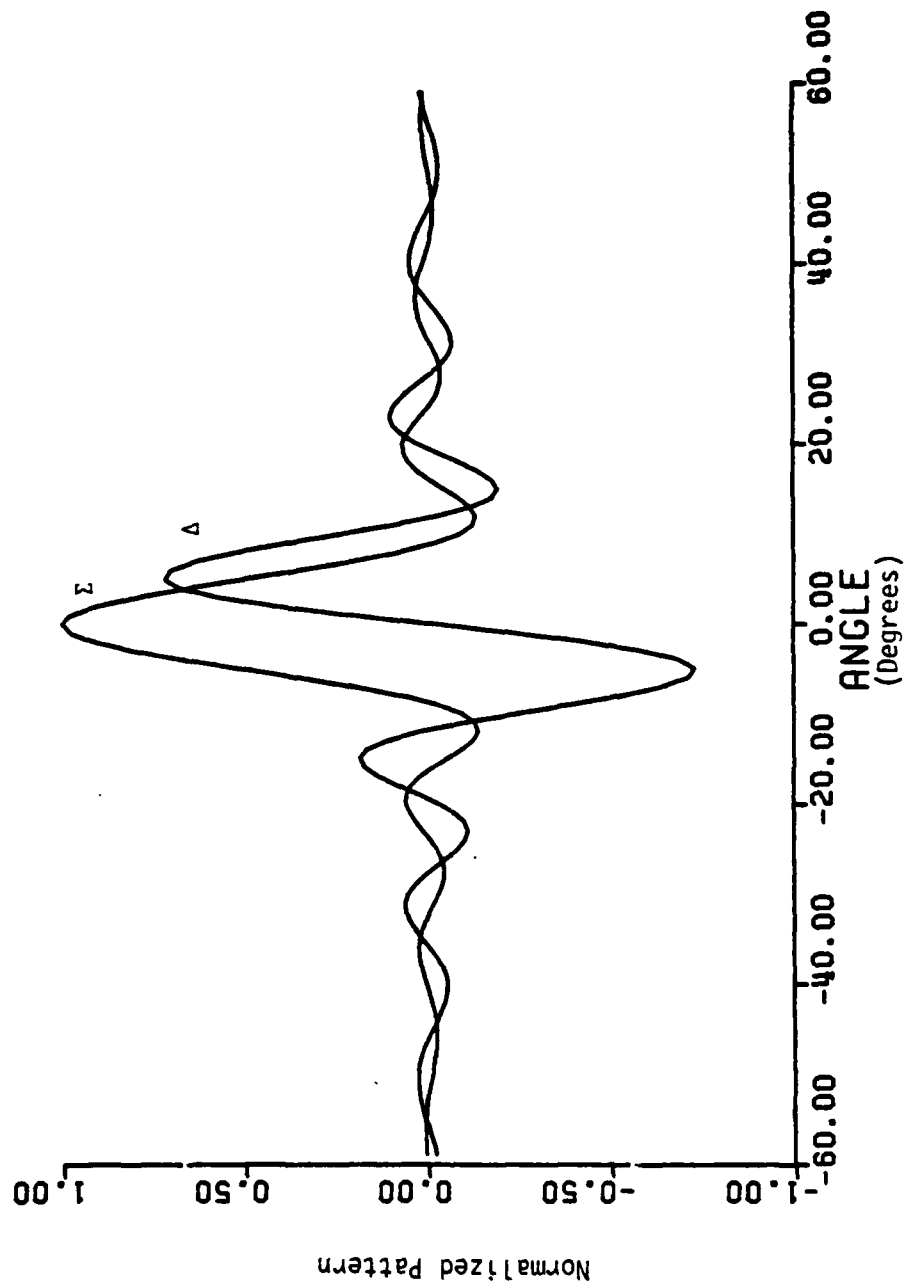


Figure 2-8. Sum and Difference Patterns of Circular Aperture with Uniform Illumination.

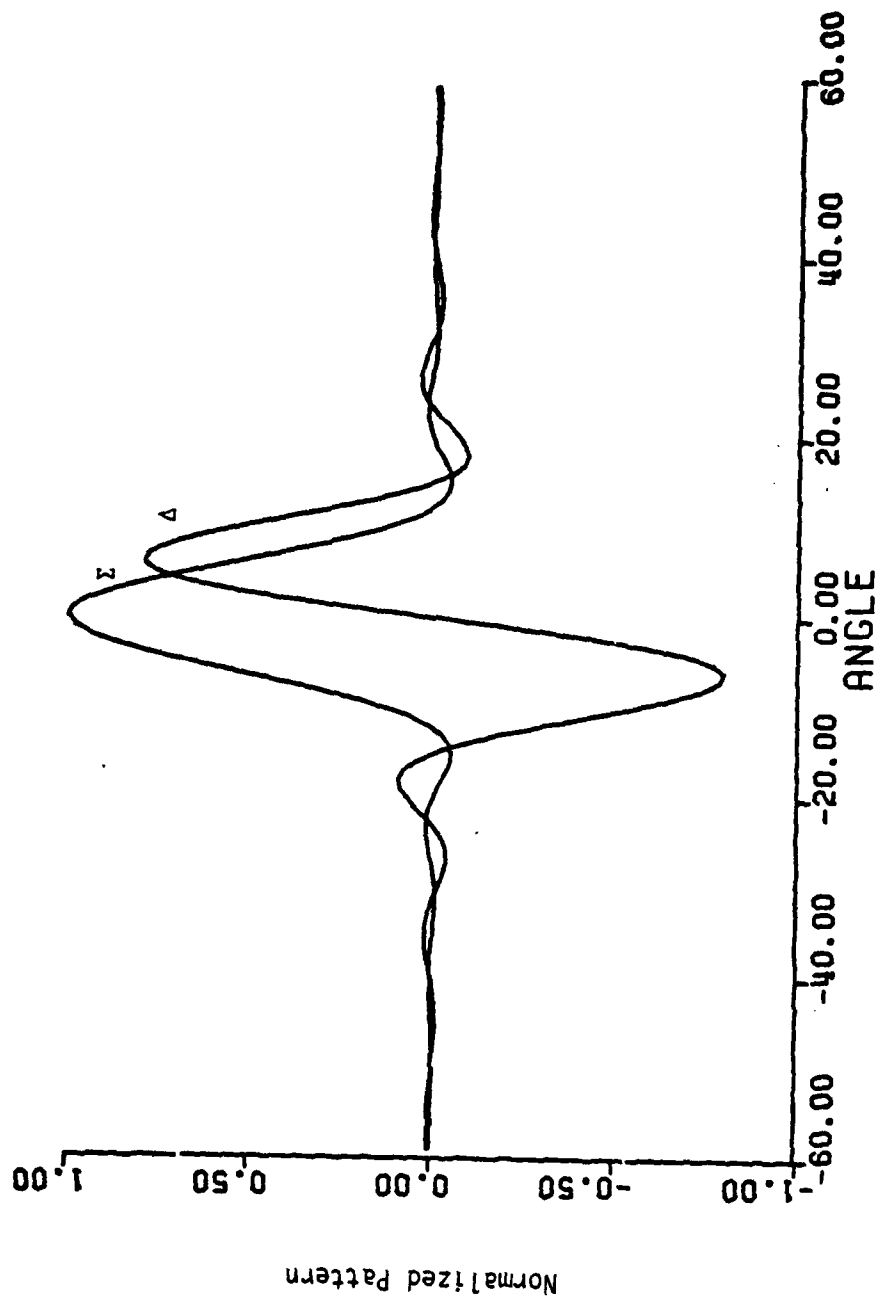


Figure 2-9. Sum and Difference Patterns of Circular Aperture with Cosine Illumination.

Monopulse angle detection is accomplished by connecting the sum and difference outputs of the parabolic antenna to an angle detection circuit as was shown in Figure 2-1. The angle of an incident plane wave, θ_i , is determined from the monopulse ratio, or

$$\theta_i = K^{-1} \operatorname{Re}\left\{\frac{-j\Delta}{\Sigma}\right\} \quad (2.40)$$

where K is the slope of the normalized difference pattern evaluated at $\theta = 0$. For the case of uniform sum illumination, the value of K is given by Barton and Ward to be $1.573 D/\lambda$ for θ_i measured in radians. For the cosine-tapered illumination, K can be shown to be $1.475 D/\lambda$.

The incidence angle equations for the 8λ diameter aperture considered in the example become,

$$\theta_i = (12.585)^{-1} \operatorname{Re}\left\{\frac{-j\Delta}{\Sigma}\right\} , \quad (2.41)$$

for the uniform illumination, and

$$\theta_i = (11.800)^{-1} \operatorname{Re}\left\{\frac{-j\Delta}{\Sigma}\right\} \quad (2.42)$$

for the cosine tapered illumination, where θ_i is in radians. These two equations and the methods outlined above will be used to find the indicated target angle in the next chapter.

To conclude this summary of monopulse principles, it is pointed out that the interferometer may be considered as an aperture illumination function given by,

$$g = E_0 \delta\left[\left|\bar{R} - \left(\pm\frac{D}{2}, 0, 0\right)\right|\right] , \quad (2.43)$$

since the interferometer samples the incident wave at the points $(\pm \frac{D}{2}, 0, 0)$ as described earlier. It is useful to keep this simple idea of wavefront sampling in mind while considering the behavior of radomes.

TANGENT OGIVE RADOME GEOMETRY

The geometry and coordinate system of the tangent ogive radome are discussed in this section. The tangent ogive is used for the radome shape throughout this study because it well represents the nose section of high-speed missiles. For minimum drag the high-speed missile must be highly streamlined. With proper parameter selection, the ogive makes a satisfactory shape for the missile nose.

The tangent ogive is a surface of revolution generated by the arc of a circle as shown in Figure 2-10. The axis of the ogive is chosen to be the y-axis, and the generating arc is centered on the z-axis in order to obtain tangency along the contour where the ogive joins the missile body. The radius of the ogive, ρ , may be expressed as a function of position along the axis, y , and the generating parameters by

$$\rho = \sqrt{R^2 - y^2} + \frac{W}{2} - R, \quad (2.44)$$

where R is the radius of the generating arc, and W is the base diameter.

A measure of an ogive's streamlining is the length-to-diameter ratio, L/W . This ratio is encountered in aerodynamic studies where it was given the name "finess ratio". The greater the fineness ratio the more streamlined is the ogive.

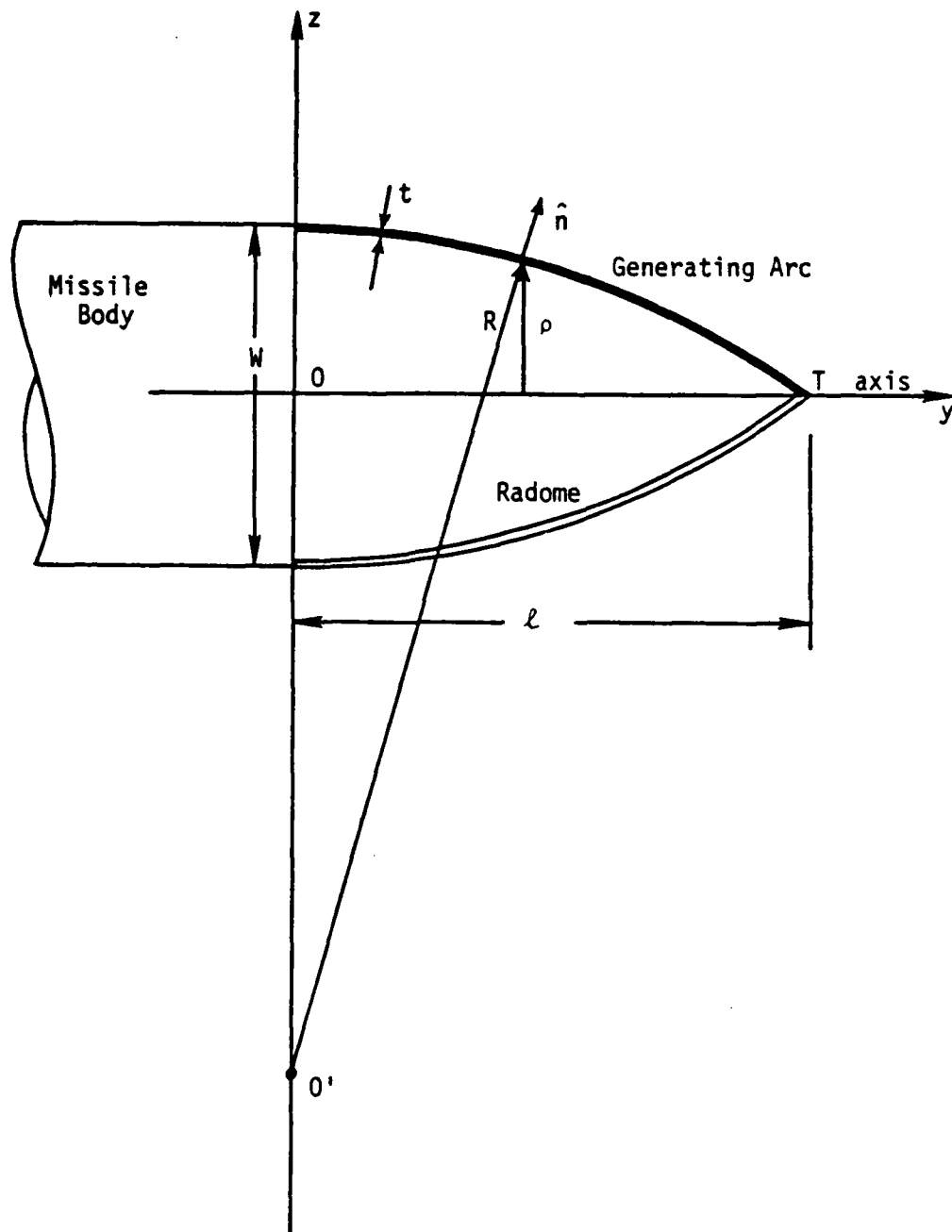


Figure 2-10. Tangent Ogive Geometry.

It is convenient to express the length of the ogive generating arc in terms of the fineness ratio and the ogive base diameter, W . This can be done by considering the right triangle OTO' in Figure 2-10. The sides of OTO' are related by,

$$R^2 = \ell^2 + \left[R - \frac{W}{2}\right]^2, \quad (2.45)$$

which can be solved for R yielding,

$$R = \left(\frac{\ell}{W}\right)^2 W + \frac{W}{4}. \quad (2.46)$$

This expression is useful for calculating R for an ogive with specific fineness ratio and diameter.

The shape of the tangent ogive is sometimes specified by the parameter, caliber. The caliber, C , is defined as the ratio of the generating arc length to the base diameter or,

$$C = R/W \quad (2.47)$$

In addition to knowing the ogive shape, the unit vector normal to the ogive surface is required for the incidence angle calculations discussed later. It is most convenient to express this unit normal, \hat{n} , as a sum of three rectangular components, or

$$\hat{n} = n_x \hat{x} + n_y \hat{y} + n_z \hat{z} \quad (2.48)$$

where n_x , n_y , n_z are the components of \hat{n} in the coordinate directions \hat{x} , \hat{y} , and \hat{z} respectively. These components can be found from geometrical considerations, or by evaluating $\nabla f/|\nabla f|$ with f given by the surface equation. The component of \hat{n} in the axial direction, n_y , is given by

$$n_y = y/R \quad . \quad (2.49)$$

The component of \hat{n} perpendicular to \hat{y} , n_r , is then found from the requirement of unit magnitude, or

$$n_r = [1 - n_y^2]^{1/2}, \quad (2.50)$$

and n_x and n_z are given by,

$$n_x = n_r x/\rho \quad , \quad (2.51)$$

$$n_z = n_r z/\rho \quad . \quad (2.52)$$

The radomes considered in this study have uniform thickness and fill the region between two concentric ogives. Thus a radome with thickness, t , and an inner surface formed by an ogive with generating radius R , has as an outer surface an ogive with generating radius $(R + t)$.

TRANSMISSION AND REFLECTION PROPERTIES OF PLANAR DIELECTRIC SLABS

In this section the transmission and reflection coefficients for plane waves incident on an infinite planar dielectric slab, or several slabs sandwiched, are derived. Virtually all analyses of radomes have used such plane-wave transmission coefficients to relate the electromagnetic field on opposite sides of a radome wall; and good results are

obtained. The technique of modeling the radome wall is discussed in the following section. Although transmission coefficients for planar slabs have been presented in the literature in varying degrees of completeness and generality (Collin [34] being one of the better examples); they are derived here in order to define the notation and demonstrate the method of solution. The technique used here is similar to the equivalent circuit approach used by Robinson [35].

The problem of transmission and reflection of a plane wave incident on a planar dielectric slab is an electromagnetic boundary condition problem. Transmission and reflection of an incident wave are necessary results of the boundary conditions at surfaces of material discontinuity. Complex transmission and reflection coefficients can be used to express the fractions of the incident fields that are respectively transmitted through and reflected from the dielectric slab as well as giving the phase of these fields. The general equation for a plane wave is used to express all the fields.

Electromagnetic fields in homogeneous, isotropic, time-invariant, source-free regions satisfy the vector Helmholtz equation,

$$\nabla^2 \vec{F} - \mu \epsilon \frac{\partial^2 \vec{F}}{\partial t^2} = 0 \quad (2.53)$$

where \vec{F} is either the electric field intensity or the magnetic field intensity, ∇^2 is the vector Laplacian operator, time dependence is $e^{j\omega t}$, μ is the permeability of the medium, and ϵ is the complex permittivity of the medium given by

$$\hat{\epsilon} = \epsilon(1 - j \tan \delta), \quad (2.54)$$

with ϵ the permittivity and $\tan \delta$ the loss tangent of the medium ($\tan \delta = \sigma/\omega\epsilon$). The use of the complex permittivity in (2.53) accounts for attenuation of the fields due to loss.

The solution to (2.53) for fields that vary in only one direction (plane waves) may be written as,

$$\bar{F} = \bar{F}_0 e^{jk\hat{a}_n \cdot \bar{r}}, \quad (2.55)$$

where \hat{a}_n is a unit vector in the direction of wave motion; $\bar{r} = x\hat{x} + y\hat{y} + z\hat{z}$; $k = \omega\sqrt{\mu\epsilon}$; and \bar{F}_0 is a complex-vector constant representing the amplitude, direction, and phase of E or H at the origin; and the time dependence is suppressed.

It will be useful to define the vector \bar{k} as

$$\bar{k} = k\hat{a}_n = k_x\hat{x} + k_y\hat{y} + k_z\hat{z}. \quad (2.56)$$

This vector is in the direction of the Poynting vector and is sometimes called the wave vector. The components of \bar{k} must satisfy

$$k_x^2 + k_y^2 + k_z^2 = \omega^2\mu\epsilon \quad (2.57)$$

This relation provides a very convenient way to treat the boundary condition problem of a plane wave incident on a planar dielectric slab.

The geometry used for a dielectric slab which may be located between two dissimilar regions is shown in Figure 2-11. For the

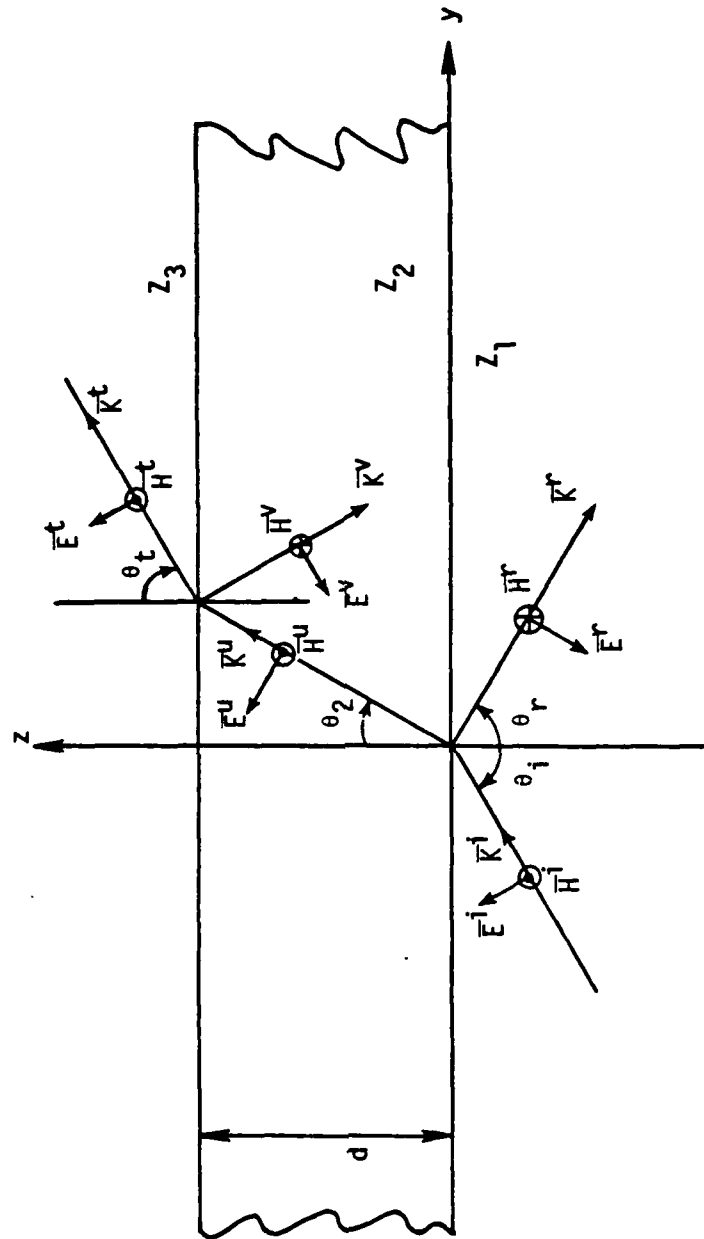


Figure 2-11. Dielectric Slab and Definition of Fields (Parallel Polarization).

practical case of a single layer, the regions $z < 0$ and $z > d$ will contain the same material, usually air.

The fields in the various regions are classified according to location and direction of travel as presented in Table 2-1. Super-scripts identify each category.

Table 2-1

Classification of Dielectric Slab Fields

Name	Location	
Incident Fields	$z < 0$	\bar{E}^i, \bar{H}^i
Positive Internal Fields	$0 < z < d$	\bar{E}^u, \bar{H}^u
Negative Internal Fields	$0 < z < d$	\bar{E}^v, \bar{H}^v
Transmitted Fields	$z > d$	\bar{E}^t, \bar{H}^t
Reflected Fields	$z < 0$	\bar{E}^r, \bar{H}^r

These classifications are straightforward but a comment is in order concerning the internal fields. When a wave is incident at $z = 0$, in general, there is a field transmitted through the interface at angle θ_2 . This field will travel to the $z = d$ interface and be partially reflected, return to $z = 0$ and again be partially reflected and so on. The notation \bar{E}^u and \bar{H}^u means the superposition of all fields in the slab traveling in the generally positive z direction. All of these fields will have the same wave vector, \bar{k}^u , as will seen by Snell's reflection law. Similarly \bar{E}^v and \bar{H}^v mean the sums of all fields traveling in the generally negative z direction. These definitions are necessary to solve the "steady-state" problem.

Two orthogonal polarization states can be considered for the incident field. The polarization directions are with respect to the plane of incidence: the plane containing the normal to the slab and \bar{k}^i . Perpendicular polarization means \bar{E}^i is perpendicular to the plane of incidence, and parallel polarization means \bar{E}^i is contained in the plane of incidence. An arbitrarily polarized incident field can be expressed as a superposition of a parallel polarized \bar{E}^i and a perpendicular polarized \bar{E}^i .

Parallel polarization will be considered first, then the transmission and reflection coefficients for perpendicular polarization will be obtained using the principle of duality. The equations for the parallel polarized plane waves listed in Table 2-1 are as follows:

$$\bar{E}^i = E_0^i e^{-j(k_y^i y + k_z^i z)} (-\cos\theta_i \hat{y} + \sin\theta_i \hat{z}) \quad (2.58)$$

$$\bar{H}^i = Z_1^{-1} E_0^i e^{-j(k_y^i y + k_z^i z)} (\hat{x}) \quad (2.59)$$

$$\bar{E}^r = E_0^r e^{-j(k_y^r y - k_z^r z)} (-\cos\theta_r \hat{y} - \sin\theta_r \hat{z}) \quad (2.60)$$

$$\bar{H}^r = Z_1^{-1} E_0^r e^{-j(k_y^r y - k_z^r z)} (-\hat{x}) \quad (2.61)$$

$$\bar{E}^u = E_0^u e^{-j(k_y^u y + k_z^u z)} (-\cos\theta_u \hat{y} + \sin\theta_u \hat{z}) \quad (2.62)$$

$$\bar{H}^u = Z_2^{-1} E_0^u e^{-j(k_y^u y + k_z^u z)} (\hat{x}) \quad (2.63)$$

$$\bar{E}^v = E_0^v e^{-j(k_y^v y - k_z^v z)} (-\cos\theta_v \hat{y} - \sin\theta_v \hat{z}) \quad (2.64)$$

$$\bar{H}^v = Z_2^{-1} E_0^v e^{-j(k_y^v y - k_z^v z)} (-\hat{x}) \quad (2.65)$$

$$\bar{E}^t = E_o^t e^{-j(k_y^t y + k_z^t(z-d))} (-\cos\theta_t \hat{y} - \sin\theta_t \hat{z}) \quad (2.66)$$

$$\bar{H}^t = Z_3^{-1} E_o^t e^{-j(k_y^t y + k_z^t(z-d))} (\hat{x}) \quad (2.67)$$

where the subscript, "o", indicates the quantity is a complex constant and Z_n is the intrinsic impedance of the n^{th} region as given by

$$Z_n = \sqrt{\frac{\mu}{\epsilon}} \quad (2.68)$$

Z_n is the ratio of transverse components of \bar{E} and \bar{H} in a uniform plane wave traveling in the medium of the n^{th} region. Note that the phase reference of the transmitted fields is taken at $(0,0,d)$.

Relations between the fields listed above are obtained from boundary conditions (2.16) and (2.17). Since no surface currents will be present on dielectric sheets, these boundary conditions reduce to continuity of tangential fields or,

$$E_{t1} = E_{t2} \quad H_{t1} = H_{t2} \quad \text{at } z = 0 \quad , \quad (2.69)$$

$$E_{t2} = E_{t3} \quad H_{t2} = H_{t3} \quad \text{at } z = d \quad , \quad (2.70)$$

where the subscript t indicates total tangential field, and the number refers to the region.

For parallel polarization (2.69) and (2.70) refer to the y-components of \bar{E} and the x-components of \bar{H} . In terms of the field components (2.70) can be written as

$$E_y^u + E_y^v = E_y^t \quad |_{z=d} \quad (2.71)$$

$$H_x^u + H_x^v = H_x^t \quad |_{z=d} \quad (2.72)$$

Substituting (2.62) - (2.67) into (2.71) and (2.72) yields

$$\begin{aligned} E_0^u e^{-j(k_y^u y + k_z^u d)} (-\cos\theta_u) + E_0^v e^{-j(k_y^v y - k_z^v d)} (-\cos\theta_v) \\ = E_0^t e^{-jk_y^t y} (-\cos\theta_t) \end{aligned} \quad (2.73)$$

$$Z_2^{-1} E_0^u e^{-j(k_y^u y + k_z^u d)} - Z_2^{-1} E_0^v e^{-j(k_y^v y - k_z^v d)} = Z_3^{-1} E_0^t e^{-jk_y^t y} \quad (2.74)$$

Equations (2.73) and (2.74) must hold for any y , given the following relation,

$$k_y^u = k_y^v = k_y^t, \quad (2.75)$$

which can be written in terms of the wave angles as

$$k^u \sin\theta_u = k^v \sin\theta_v = k^t \sin\theta_t. \quad (2.76)$$

Since k^u equals k^v (waves in the same medium), the first equality in (2.76) expresses Snell's reflection law: angle of incidence equals angle of reflection. The second equality in (2.76) is Snell's law of refraction. The same relationship holds at the $z = 0$ boundary and can be applied consecutively for layered media.

By taking advantage of (2.75), equation (2.73) and (2.74) can be simplified to

$$E_0^u e^{-j\psi} \cos\theta_2 + E_0^v e^{+j\psi} \cos\theta_2 = E_0^t \cos\theta_t \quad (2.77)$$

$$Z_2^{-1} [E_0^u e^{-j\psi} - E_0^v e^{+j\psi}] = Z_3^{-1} E_0^t \quad (2.78)$$

where θ_u and θ_v have been replaced by θ_2 and where ψ is given by

$$\psi = (k_z^u d) = (k_z^v d) = k^u d \cos\theta_2 \quad (2.79)$$

A matrix equation can be written to combine (2.77) and (2.78),

$$\begin{bmatrix} \frac{j\psi}{e} + \frac{-j\psi}{e} & Z_2 \cos\theta_2 \frac{-j\psi}{e} - \frac{j\psi}{e} \\ \frac{-j\psi}{Z_2 \cos\theta_2} - \frac{j\psi}{2} & \frac{j\psi}{e} + \frac{-j\psi}{e} \end{bmatrix} \begin{bmatrix} (E_0^u + E_0^v) \cos\theta_2 \\ Z_2^{-1} (E_0^u - E_0^v) \end{bmatrix} = \begin{bmatrix} E_0^t \cos\theta_t \\ Z_3^{-1} E_0^t \end{bmatrix} \quad (2.80)$$

The use of hyperbolic functions allows this to be written as

$$\begin{bmatrix} \cosh(j\psi) & -Z_2 \cos\theta_2 \sinh(j\psi) \\ \frac{-\sinh(j\psi)}{Z_2 \cos\theta_2} & \cosh(j\psi) \end{bmatrix} \begin{bmatrix} (E_0^u + E_0^v) \cos\theta_2 \\ Z_2^{-1} (E_0^u - E_0^v) \end{bmatrix} = \begin{bmatrix} E_0^t \cos\theta_t \\ Z_3^{-1} E_0^t \end{bmatrix} \quad (2.81)$$

Multiplying each side of (2.81) by the inverse of the coefficient matrix yields,

$$\begin{bmatrix} (E_0^u + E_0^v) \cos\theta_2 \\ Z_2^{-1} (E_0^u - E_0^v) \end{bmatrix} = \begin{bmatrix} \cosh(j\psi) & Z_2 \cos\theta_2 \sinh(j\psi) \\ \frac{\sinh(j\psi)}{Z_2 \cos\theta_2} & \cosh(j\psi) \end{bmatrix} \begin{bmatrix} E_0^t \cos\theta_t \\ Z_3^{-1} E_0^t \end{bmatrix} \quad (2.82)$$

This is a very useful result since it relates the tangential fields on one side of the slab to those on the other side or in general,

$$\begin{bmatrix} E_{tN} \\ H_{tN} \end{bmatrix} = \begin{bmatrix} A & B \\ C & D \end{bmatrix} \begin{bmatrix} E_{t(N+1)} \\ H_{t(N+1)} \end{bmatrix}, \quad (2.83)$$

where N and $N+1$ indicate the total tangential fields at the N^{th} and $(N+1)^{\text{th}}$ interface and A , B , C , and D are identified from (2.82). This result is analogous to the ABCD matrix used in circuit theory to relate the input voltage and current of a two-port network to the output voltage and current.

The left-hand side of (2.82) contains the tangential fields at the $z = 0^+$ boundary, which must be equal to the tangential components of the incident fields. Writing this in matrix form yields,

$$\begin{bmatrix} (E_0^i + E_0^r) \cos \theta_1 \\ Z_1^{-1} (E_0^i - E_0^r) \end{bmatrix} = \begin{bmatrix} (E_0^u + E_0^v) \cos \theta_2 \\ Z_2^{-1} (E_0^u - E_0^v) \end{bmatrix} \quad (2.84)$$

Since E_0^i and E_0^r are both of interest they can be factored out of the left-hand side of (2.84) and the right-hand side can be replaced using (2.82)

$$\begin{bmatrix} \cos \theta_1 & \cos \theta_1 \\ Z_1^{-1} & -Z_1^{-1} \end{bmatrix} \begin{bmatrix} E_0^i \\ E_0^r \end{bmatrix} = \begin{bmatrix} A & B \\ C & D \end{bmatrix} \begin{bmatrix} E_0^t \cos \theta \\ Z_3^{-1} E_0^t \end{bmatrix} \quad (2.85)$$

This equation contains all the information needed to find the transmission and reflection coefficients. For the usual case of a slab with

the same medium on both sides, $\theta_i = \theta_t$ and $Z_1 = Z_3$. This case is considered here. The parallel polarization transmission coefficient, T_{11} , is defined as

$$T_{11} = \frac{E_0^t}{E_0^i} \quad (2.86)$$

and is found from (2.85) to be

$$T_{11} = \frac{2}{A + \frac{B}{Z_1 \cos \theta_i} + C Z_1 \cos \theta_i + D} \quad (2.87)$$

The parallel polarization reflection coefficient, r_{11} , is defined as,

$$r_{11} = \frac{E_0^r}{E_0^i} \quad (2.88)$$

and is from (2.85),

$$r_{11} = \frac{A + \frac{B}{Z_1 \cos \theta_i} - C Z_1 \cos \theta_i - D}{A + \frac{B}{Z_1 \cos \theta_i} + C Z_1 \cos \theta_i + D} \quad (2.89)$$

One additional parameter of interest is the insertion phase delay (IPD) which is defined as the phase of E_0^t minus the phase of E_0^i at $(0,0,d)$, when the slab is removed. This is the additional phase shift introduced by the presence of the slab. The IPD for parallel polarization is given by

$$\text{IPD}_{11} = -\angle T_{11} - \text{Re}\{k^i\} d \cos \theta_i \quad (2.90)$$

Transmission and reflection coefficients for perpendicular polarization can be easily obtained from the above by duality. The symmetry of the electromagnetic field equations permits the following substitutions

to be made in any equation to obtain a dual equation: \bar{H} replaces \bar{E} , $-\bar{E}$ replaces \bar{H} and Z^{-1} replaces Z . These and other duals are listed in many electromagnetic texts such as [36]. As seen in Figure 2-13(a) and (b), these substitutions transform parallel polarization to perpendicular polarization.

The ABCD matrix that relates tangential field components at the slab boundaries becomes,

$$\begin{bmatrix} H_{tN} \\ -E_{tN} \end{bmatrix} = \begin{bmatrix} A & B \\ C & D \end{bmatrix} \begin{bmatrix} H_t (N+1) \\ -E_t (N+1) \end{bmatrix}, \quad (2.91)$$

where,

$$\begin{bmatrix} A & B \\ C & D \end{bmatrix} = \begin{bmatrix} \cosh(j\psi) & \frac{\cos\theta_2 \sinh(j\psi)}{Z_2} \\ \frac{Z_2 \sinh(j\psi)}{\cos\theta_2} & \cosh(j\psi) \end{bmatrix}, \quad (2.92)$$

and ψ is still given by (2.79).

The dual of (2.85) is

$$\begin{bmatrix} \cos\theta_i & \cos\theta_i \\ Z_1 & -Z_1 \end{bmatrix} \begin{bmatrix} H_o^i \\ H_o^r \end{bmatrix} = \begin{bmatrix} A & B \\ C & D \end{bmatrix} \begin{bmatrix} H_o^t \cos\theta_t \\ Z_3 H_o^t \end{bmatrix} \quad (2.93)$$

and can be used to find the transmission and reflection coefficients.

The perpendicular polarization transmission coefficient, T_{\perp} , is now found from,

$$T_{\perp} = \frac{H_o^t}{H_o^i}, \quad (2.94)$$

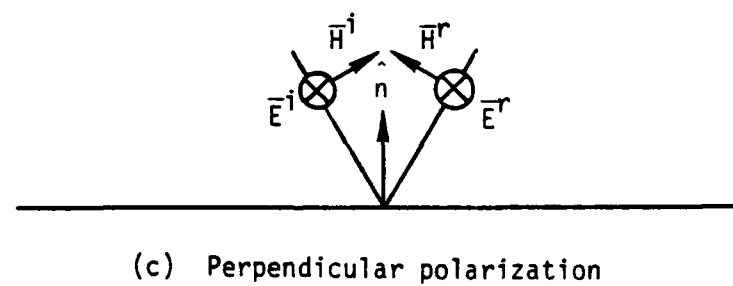
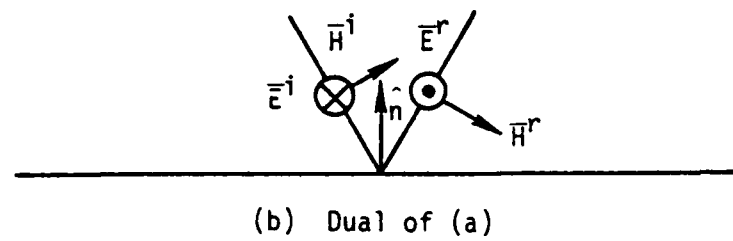
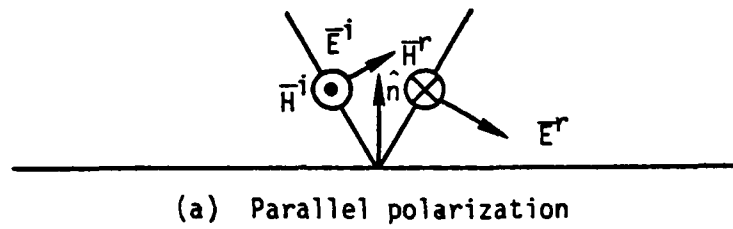


Figure 2-12. Reference Polarization Directions.

and is given by,

$$T_{\perp} = \frac{2}{A + \frac{B Z_1}{\cos \theta_i} + \frac{C \cos \theta_i}{Z_1} + D} \quad (2.95)$$

The perpendicular polarization reflection coefficient, r_{\perp} , is defined as,

$$r_{\perp} = \frac{-H_0^r}{H_0^i} \quad , \quad (2.96)$$

and is given by

$$r_{\perp} = \frac{-A - \frac{B Z_1}{\cos \theta_i} + \frac{C \cos \theta_i}{Z_1} + D}{A + \frac{B Z_1}{\cos \theta_i} + \frac{C \cos \theta_i}{Z_1} + D} \quad (2.97)$$

The minus sign in (2.96) is chosen to conform to the reference directions of Figure 2-12(c) in order to make $T_{11} = T_{\perp}$ at normal incidence.

The insertion phase delay for perpendicular polarization is found by substituting T_{\perp} for T_{11} in (2.90).

Practical radomes are usually constructed of several different materials arranged in laminated layers in order to achieve design goals for strength, weight, rain erosion resistance, etc. The above formulation permits the quick calculation of transmission and reflection coefficients for multiple layered slabs. Recall that the ABCD matrix related the tangential fields at opposite sides of a homogeneous layer. When several layers are present the "output" fields of one layer become the "input" fields to the next layer. Thus by cascading the transfer matrices for each layer the overall transmission

and reflection properties of sandwiched layers can be determined.

The system transfer matrix is given by

$$\begin{bmatrix} A & B \\ C & D \end{bmatrix} = \begin{bmatrix} A_1 & B_1 \\ C_1 & D_1 \end{bmatrix} \begin{bmatrix} A_2 & B_2 \\ C_2 & D_2 \end{bmatrix} \cdots \begin{bmatrix} A_N & B_N \\ C_N & D_N \end{bmatrix} \quad (2.98)$$

where N layers are present and the terms are given by (2.82) or (2.92) depending on the polarization. Transmission and reflection coefficient are given by the same formulas with the ABCD parameters determined from (2.98). Subroutine TRANS listed in the appendix computes the transmission and reflection coefficients used to model radome walls in this study.

Radomes with high transmission coefficients are desirable in most applications. A lossless planar slab can be designed to have a transmission coefficient with a magnitude of one for a particular angle of incidence. This is seen for a single-layer slab by examining the denominators of the transmission coefficient expressions (2.87) and (2.95). When the slab material is lossless, ψ is purely real and these denominators will equal 2 whenever $\psi = n\pi$, with n an integer. For a slab constructed of a given material this is achieved by making the thickness of the slab, d , according to

$$d = \frac{n\lambda_0}{2[\mu_r \epsilon_r - \sin^2 \theta_i]^{\frac{1}{2}}}, \quad (2.99)$$

where λ_0 is the free-space wavelength; μ_r and ϵ_r are the relative permeability and permittivity of the slab respectively; and (2.76) has been

used to write $\cos\theta_2$ in terms of $\sin\theta_1$, the incident angle. For normal incidence, (2.99) indicates that the slab thickness must be an integral number of half wavelengths in the slab for 100% transmission. However, the transmission coefficient for this case is unity only at normal incidence and decreases as the incidence angle increases. Figure 2-13 shows the transmission coefficient of a half-wave-thick slab as a function of incidence angle for both polarizations. Insertion phase delay is also plotted. The reflection coefficients for this slab are shown in Figure 2-14.

The incidence angles for the radomes in this study are quite large, as will be shown in the next chapter and a slab designed for complete transmission at an angle in the range of angles actually encountered will make a better radome wall. Figure 2-15 shows the transmission coefficients for a slab with a 75° design angle and Figure 2-16 contains the reflection coefficient for the same slab. It should be noted that the IPD of both polarizations are equal at the design angle and the reflection coefficient vanishes at this angle.

PRINCIPLES OF RAY TRACING

This section discusses the application of ray tracing to obtain electromagnetic fields that are transmitted or reflected by planar dielectric slabs. The previous section dealt with infinite planar slabs and true plane waves (infinite in extent). Ray tracing fits this theory to finite structures.

The technique of ray tracing is based on the fact that all electromagnetic fields behave locally like plane waves whenever they interact

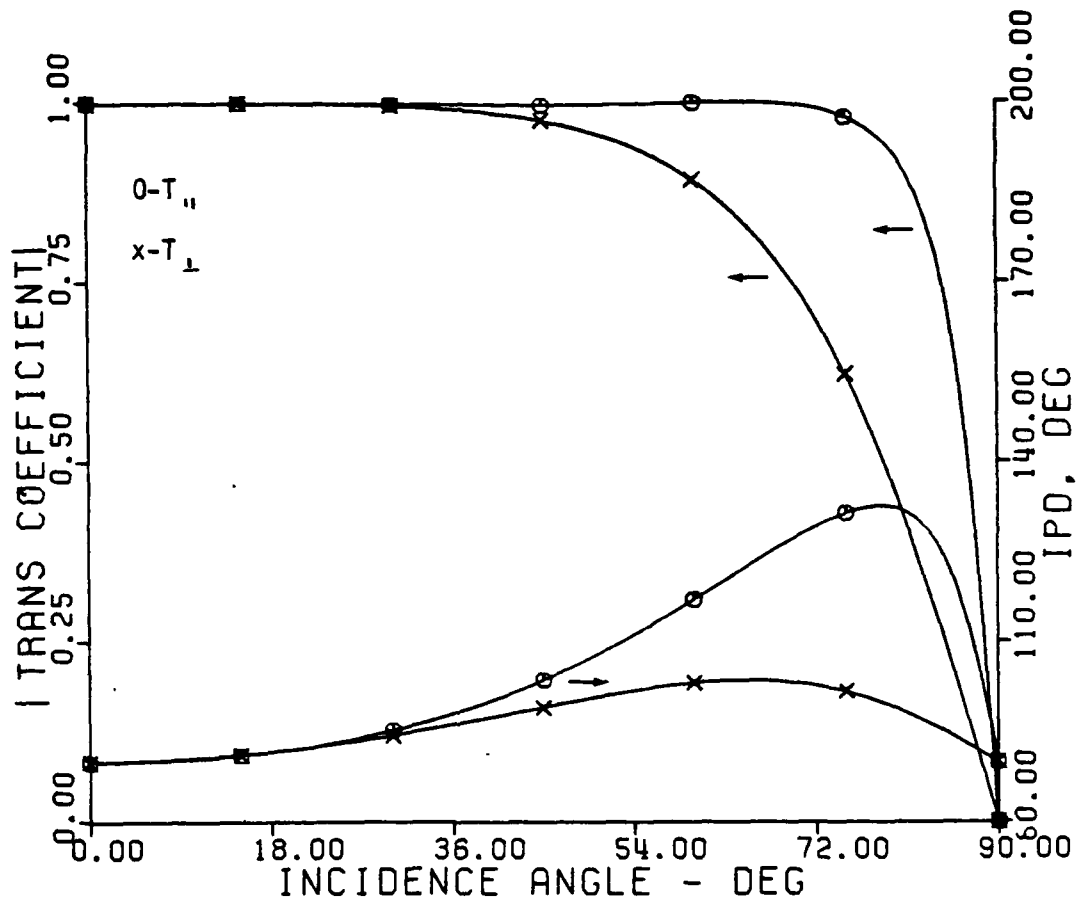


Figure 2-13. Transmission Coefficient of Lossless Dielectric Slab with Half-wavelength Thickness.

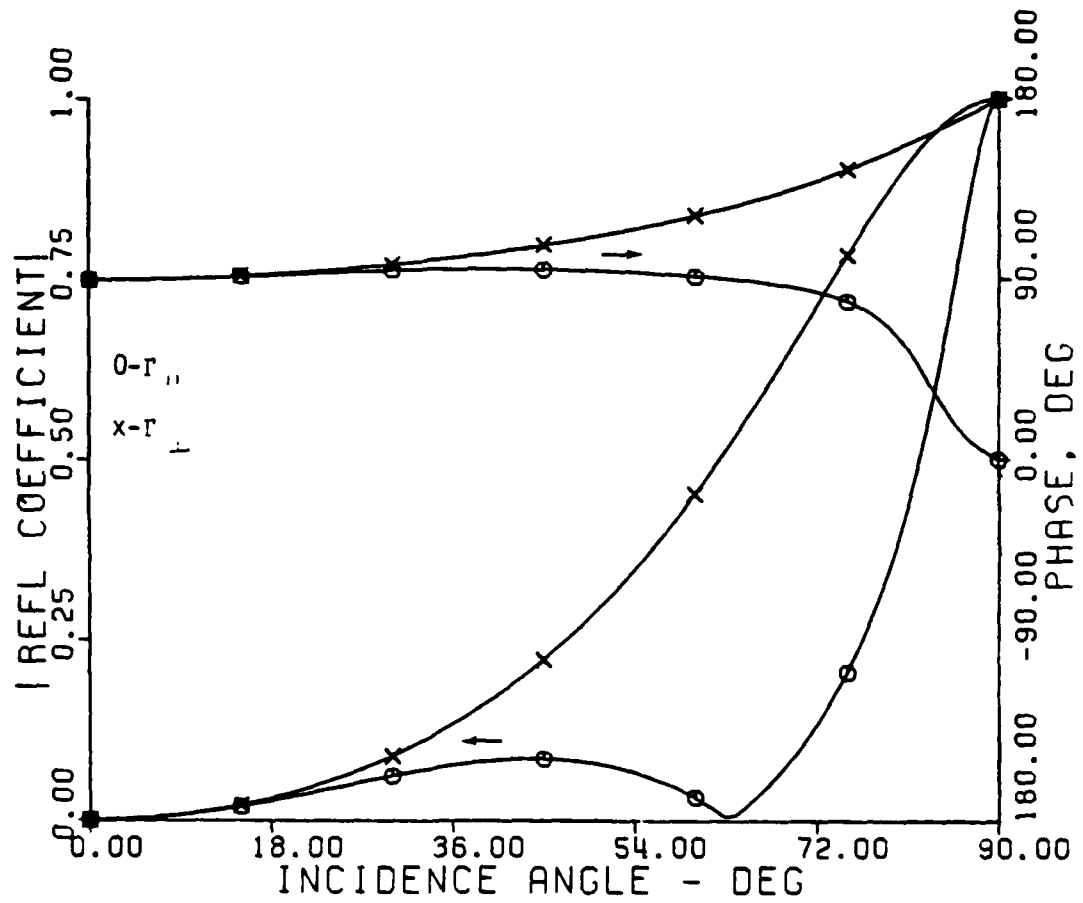


Figure 2-14. Reflection Coefficient of Lossless Dielectric Slab with Half-wavelength Thickness.

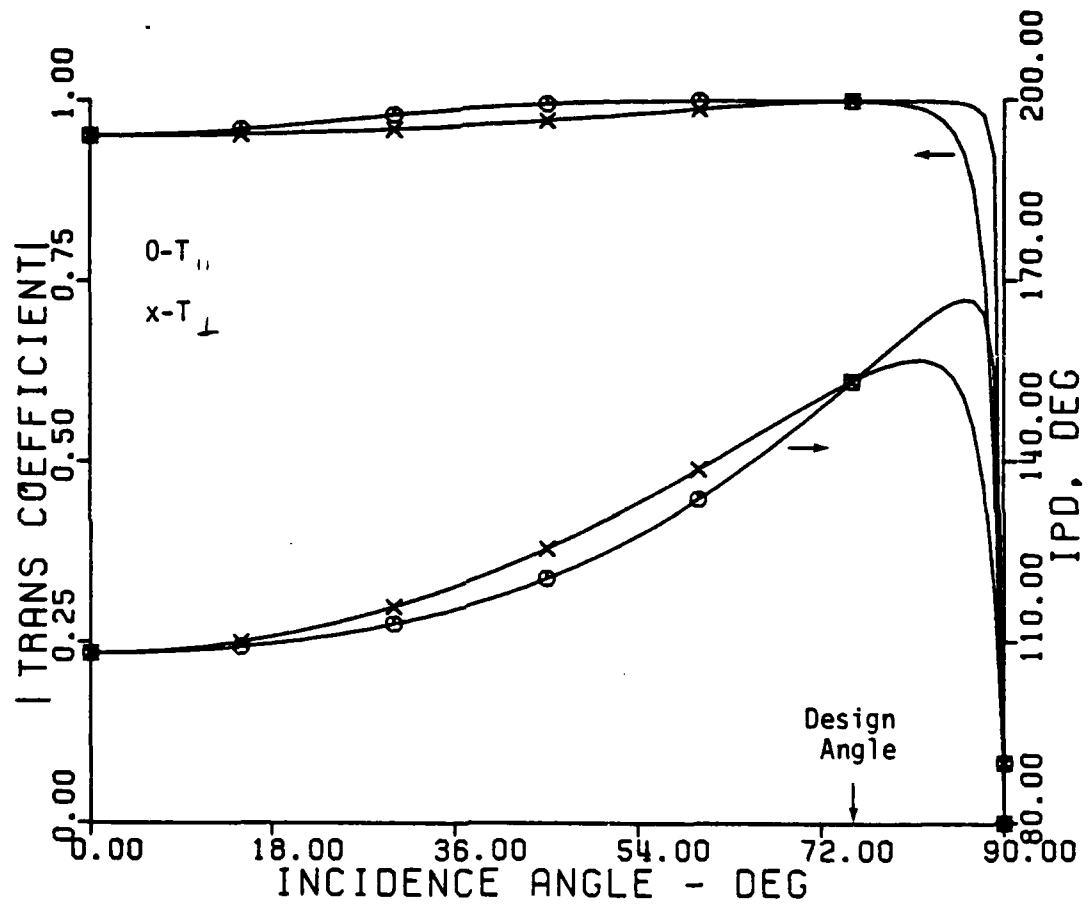


Figure 2-15. Transmission Coefficient of Lossless Dielectric Slab with 75° Design Angle.

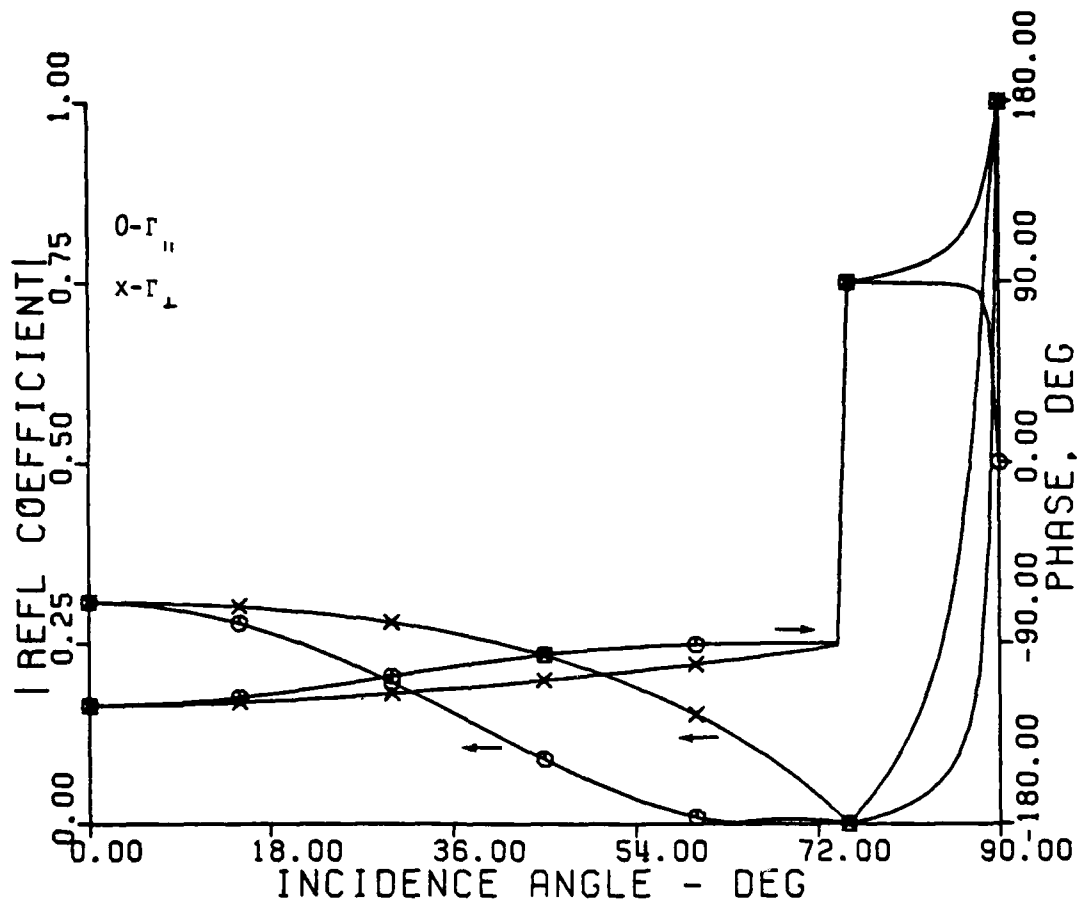


Figure 2-16. Reflection Coefficient of Lossless Dielectric Slab with 75° Design Angle.

with matter that is large with respect to wavelength, and has radii of curvature large with respect to wavelength. Macroscopic materials have these properties at optical frequencies, and ray tracing is frequently used in the analysis of optical systems.

A ray is a directed line that is everywhere perpendicular to a wave's surfaces of constant phase. Rays are in the direction of wave propagation which is the direction of power flow or the Poynting vector. When dealing with plane waves, as in the previous section, it is easy to visualize the wave traveling in the direction of the rays in the various media.

Snell's transmission and reflection laws are used to predict the directions of the "transmitted ray" and "reflected ray" whenever a ray intersects a material discontinuity. Ray tracing of a transmitted ray will be considered here first, and a discussion of ray reflection will end this section.

Consider an arbitrarily polarized wave incident on a planar slab. This wave can be decomposed into a sum of parallel and perpendicular polarized waves as shown in Figure 2-17. The perpendicular component is found by first forming a unit vector perpendicular to the plane of incidence (plane containing the ray and the surface normal). This unit vector, \hat{b} , is often called a binormal vector and is found from,

$$\hat{b} = \frac{\hat{r} \times \hat{n}}{|\hat{r} \times \hat{n}|}, \quad (2.100)$$

where \hat{r} and \hat{n} are unit vectors in the directions of the ray and surface normal respectively as shown in Figure 2-17.

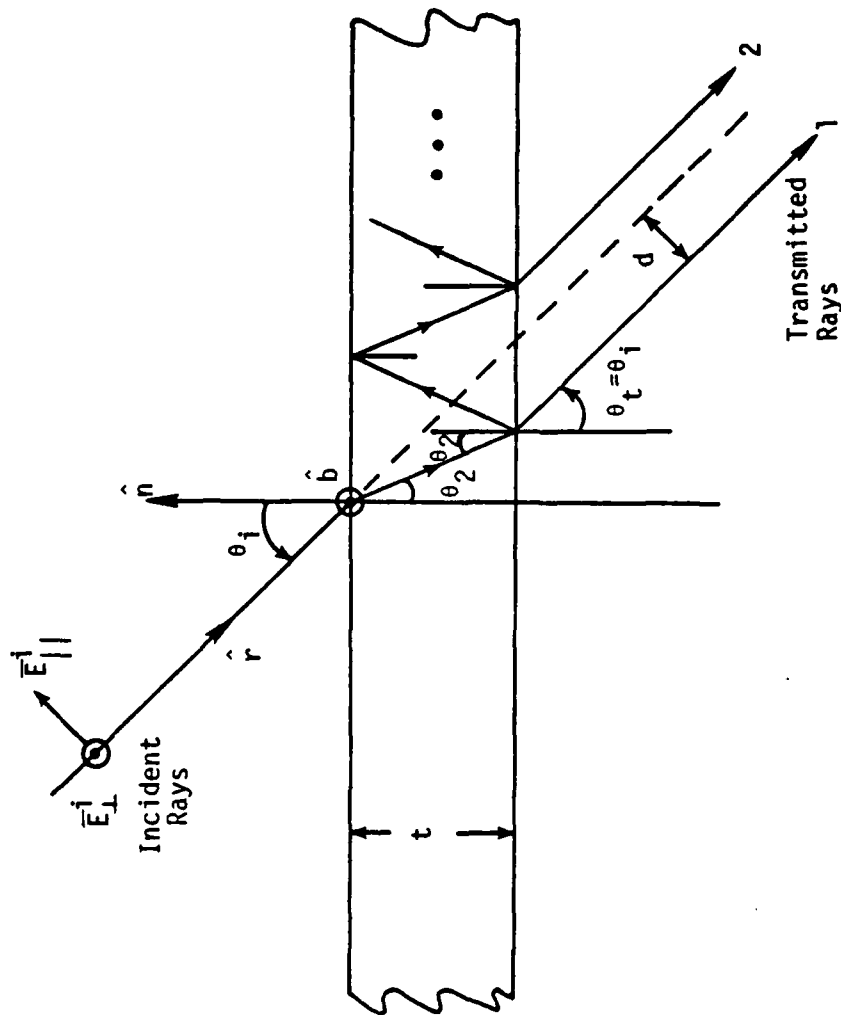


Figure 2-17. Dielectric Slab and Offset Transmitted Rays

The perpendicular component, E_{\perp}^i , of the incident electric field, \vec{E}^i , is found from the dot product as

$$E_{\perp}^i = \vec{E}^i \cdot \hat{b} \quad . \quad (2.101)$$

Since the incident field is transverse to \hat{r} , the parallel component of the incident field can be found by vectorially subtracting the perpendicular component from the total incident field or,

$$\vec{E}_{||}^i = \vec{E}^i - \vec{E}_{\perp}^i \quad , \quad (2.102)$$

where $\vec{E}_{||}^i$ is the parallel polarized component of the incident field and \vec{E}_{\perp}^i is given by

$$\vec{E}_{\perp}^i = (\vec{E}^i \cdot \hat{b})\hat{b} \quad . \quad (2.103)$$

Of course, the total field is now the superposition of the parallel and perpendicular parts or,

$$\vec{E}^i = \vec{E}_{||}^i + \vec{E}_{\perp}^i \quad . \quad (2.104)$$

This decomposition is useful since a parallel polarized incident wave produces only a parallel polarized reflected and transmitted wave. Likewise there is no cross-polarization for the perpendicular case.

The ray angle of incidence, θ_i , is important since the transmission and reflection coefficients are functions of this angle as shown in the preceding section. The angle of incidence can be found from the vectors \hat{r} and \hat{n} by use of the dot product, or,

$$\theta_i = \cos^{-1} (-\hat{r} \cdot \hat{n}) \quad (2.105)$$

The ray incident on the slab at angle θ_i will enter the slab at angle θ_2 given by Snell's refraction law, (2.76), and emerge on the opposite side again at angle θ_i . Although the transmitted ray exits at the same angle as the incident ray, there is an offset between them because θ_2 is less than θ_i for dielectric slabs in air. This offset is indicated by d in Figure 2-17. The amount of this offset will depend on the slab material, slab thickness, and the angle of incidence. Jenkins and White [37] give the following expression for d produced by lossless dielectric slabs,

$$d = t \sin \theta_i \left[1 - \frac{n \cos \theta_i}{n_1 \cos \theta_2} \right] \quad (2.105)$$

where n and n_1 are the indices of refraction of the immersing medium and slab respectively, as given by $\sqrt{\mu_r \epsilon_r}$ for the appropriate medium.

Plots of d normalized to the slab thickness versus angle of incidence are shown in Figure 2-18 for non-magnetic slabs with various permittivities. It is noted that for intermediate values of dielectric constant, as frequently encountered with radome materials, the deviation is approximately linear with incidence angle.

In addition to the ray that initially emerges from the dielectric slab, other rays will be transmitted after multiple reflection from the interior slab boundaries. These rays exit periodically down the slab and their energy diminishes geometrically with the number of interior reflections. The transmission coefficients previously derived consider all these reflections in order to satisfy the boundary conditions at the interfaces.

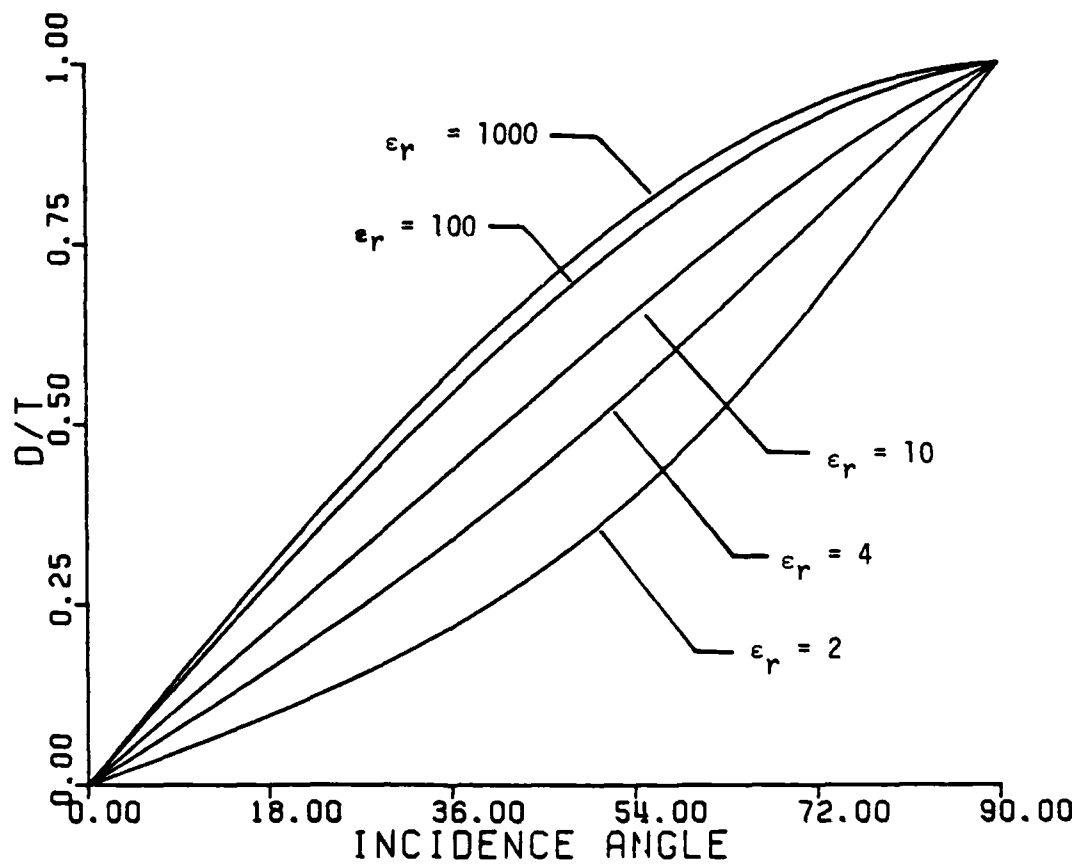


Figure 2-18. Ray Offset versus Incident Angle for Dielectric Slab with Various Permittivities.

The approach taken in this work is to ignore the ray deviation produced by transmission and assume the incident ray continues linearly through the slab. The radome walls under consideration here have thicknesses on the order of one-quarter of a free-space wavelength and even at the high incidence angles encountered, the ray deviation is approximately two-tenths of a wavelength. The error introduced by this assumption is considered to be in line with other approximations made. Multiple reflections are taken into account through the use of the transmission coefficients from the last section.

The transmitted electric field at a given point is found by considering an incident ray which would pass through the point with the slab removed and then weighting the field of this ray with the appropriate transmission coefficient, or in equation form,

$$\bar{E}^t = \bar{E}_{||}^i \hat{T}_{||} + \bar{E}_{\perp}^i \hat{T}_{\perp} \quad , \quad (2.106)$$

with $\bar{E}_{||}^i$ and \bar{E}_{\perp}^i are the previously derived parallel and perpendicular components of the incident field, $\hat{T}_{||}$ and \hat{T}_{\perp} are the insertion transmission coefficients given by,

$$\hat{T}_{||} = |T_{||}| \exp (-j \text{IPD}_{||}) \quad , \quad (2.107)$$

and

$$\hat{T}_{\perp} = |T_{\perp}| \exp (-j \text{IPD}_{\perp}) . \quad (2.108)$$

Since the two transmission coefficients generally have magnitude less than one and differ in both magnitude and phase, equation (2.106)

indicates that the transmitted field is, in general, attenuated, phase shifted, and depolarized. Furthermore each of these undesirable characteristics is a function of incident angle. All these phenomena contribute to radome-induced radar pointing error.

Reflection may also be treated by ray tracing. Consider again a plane wave incident on a dielectric slab as shown in Figure 2-19. The incident field is composed of parallel and perpendicular components as given by (2.102) and (2.103). The unit vector, \hat{r} , is in the direction of the incident ray and the unit vector, \hat{p} , is in the direction of the primary reflected ray.

According to Snell's reflection law, the angle of incidence, θ_i , is equal to the angle of reflection, θ_r . This results in the following equation for finding the reflected ray vector, \hat{p} :

$$\hat{p} = \hat{r} - 2(\hat{n} \cdot \hat{r}) \hat{n} \quad , \quad (2.109)$$

where \hat{n} is the outward unit surface normal.

As in the transmission case, additional rays emerge from the slab due to multiple internal reflection as seen in Figure 2-19. Again for the purpose of ray tracing these rays will be ignored; however, the reflection coefficients used to find the magnitude and phase of the reflected ray take into account multiple reflection as discussed in the previous section.

The perpendicular-polarized reflected field, \bar{E}_\perp^r , is given by

$$\bar{E}_\perp^r = \Gamma_\perp \bar{E}_\perp^i \quad , \quad (2.110)$$

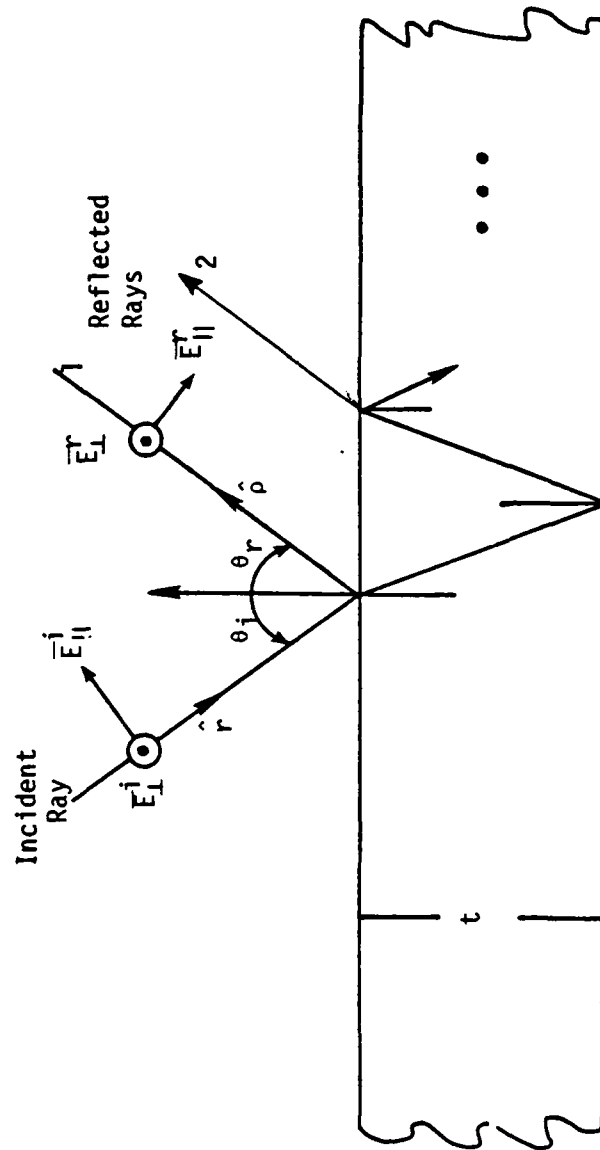


Figure 2-19. Dielectric Slab and Reflected Rays

where Γ_{\perp} is the reflection coefficient for perpendicular polarization, \bar{E}_{\perp}^i is given by (2.103), and the expression is evaluated at the boundary.

The equation for the parallel polarized reflected field, $\bar{E}_{||}^r$, is not as simple as (2.110). Recall that the reference direction for $\bar{E}_{||}^r$ was chosen as shown in Figure 2-19 so that parallel and perpendicular polarization would coincide at normal incidence. $\bar{E}_{||}^r$ must lie in the plane of incidence and be normal to the direction of propagation. Thus, there is no scalar constant which gives $\bar{E}_{||}^r$ when multiplied by $\bar{E}_{||}^i$ (except at normal and grazing incidence).

According to the reference directions of Figure 2-19, the tangential components of the incident and reflected field are related by the reflection coefficient, but the normal components are related by the negative of the transmission coefficient. The normal component of $\bar{E}_{||}^i$ is given by

$$\bar{E}_{||n}^i = (\bar{E}_{||}^i \cdot \hat{n}) \hat{n} \quad , \quad (2.111)$$

and the tangential component can be found by subtraction as

$$\bar{E}_{||t}^i = \bar{E}_{||}^i - \bar{E}_{||n}^i \quad , \quad (2.112)$$

where n and t in the subscript indicates normal and tangential respectively. The reflected components at the boundary are,

$$\bar{E}_{||t}^r = \Gamma_{||} \bar{E}_{||t}^i \quad , \quad (2.113)$$

and

$$\bar{E}_{||n}^r = -\Gamma_{||} \bar{E}_{||n}^i \quad , \quad (2.114)$$

for the reference directions used here.

The total reflected field is the sum of (2.113) and (2.114) which simplifies by substitution of (2.111) and (2.112) to,

$$\bar{E}_{11}^r = \Gamma_{11} [\bar{E}_{11}^i - 2(\bar{E}_{11}^i \cdot \hat{n}) \hat{n}] . \quad (2.115)$$

This equation gives the magnitude, phase, and direction of the reflected field at the interface.

As discussed in conjunction with the transmission problem, an incident field will, in general, have parallel and perpendicular field components. The reflection coefficients for these two polarization states differ in magnitude and phase. Thus, as was the case with transmission, the fields reflected from a planar dielectric slab will be attenuated, phase shifted and depolarized. One might hastily conclude that these effects must degrade radome performance, but it will be seen that indeed any reflection from a radome wall is undesirable.

This chapter has discussed the basic elements used in radome analysis. The following chapter will connect these elements to analyze radome system performance.

III. RADOME-INDUCED RADAR POINTING ERRORS

In this chapter the effect of an ogive radome on an incident uniform plane wave is considered. It will be shown that the radome causes amplitude, phase and polarization distortion in the wave transmitted through the radome. This distortion causes the radar inside the radome to indicate erroneous pointing directions.

Two mechanisms for wavefront distortion are considered. The first is due to the variation of the radome wall transmission coefficient with incidence angle and the second is due to reflection of energy from the interior of the radome wall. The methods for treating these sources of distortion are based on techniques presented in Chapter II. Radar response to wavefront distortion is obtained by integration of the incident wave over the radar antenna aperture.

This chapter begins with a short section discussing pointing error. Sections on the two sources of wavefront distortion and the composite effects of distortion follow. The chapter is concluded by considering radar response to radome-induced wavefront distortion.

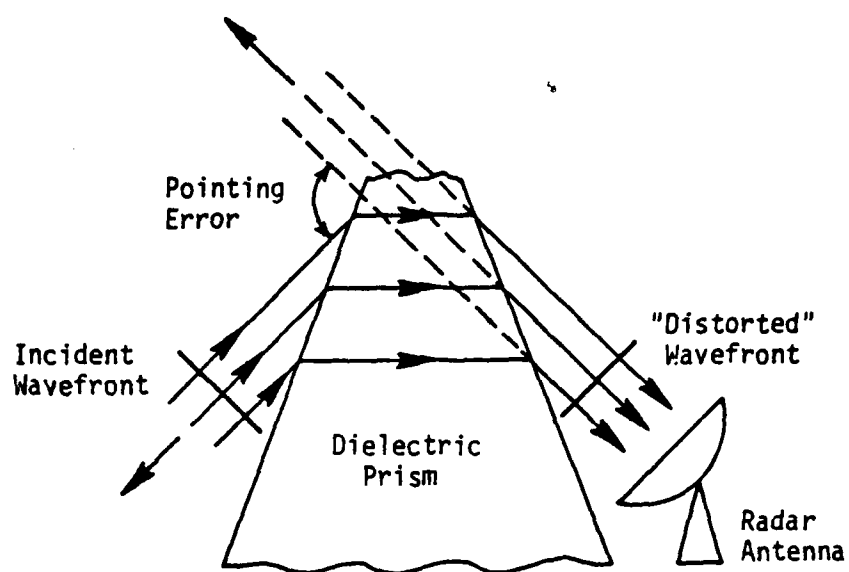
CONCEPT OF POINTING ERROR

Radar pointing error is the difference between the angle that a radar indicates to a given target and the true angle to that target. A similar term given by the Institute of Electrical and Electronics Engineers (IEEE) is boresight error which is defined as "the angular deviation of the electrical boresight of an antenna from its reference

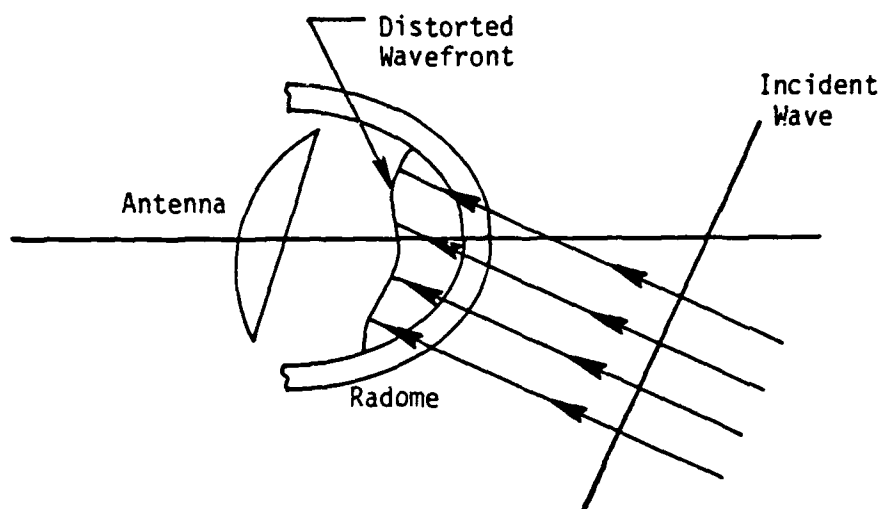
boresight" [38]. Although the IEEE gives no definition for the word "boresight", it obviously originated from the practice of using optical instruments mounted on the antenna to calibrate the electrical output of the radar with the mechanical position of the antenna.

Sources of radar pointing error may be broadly divided into two categories: internal sources and external or environmental sources. Internal sources of error refer to imperfections in the radar hardware (or software) and would include amplitude and phase unbalance in signal forming networks, noise in signal channels, nonlinearities, and quantization errors. External sources of error are due to environmental factors which would cause even a "perfect" radar to indicate an erroneous direction to the radar target. Some external sources of error are glint, multipath, non-uniform propagation media, clutter, jamming, and of course radomes. (A different point of view will be taken in the next chapter where the radar and radome are considered a single system.)

As a simple example of how pointing error can arise consider a uniform plane wave incident on a dielectric prism as illustrated in Figure 3-1(a). According to the familiar principles of the prism, the waves entering and leaving the prism are in different directions due to the unequal optical path lengths of the rays through different parts of the prism. A radar measuring the direction to the source of the wave leaving the prism will indicate that the source is located in the direction perpendicular to the wavefront at the antenna as was discussed in the previous chapter. The difference between the direction to the target indicated by the radar and the true direction to the target is the pointing error.



(a). Plane wave incident on dielectric prism.



(b). Plane wave incident on radome.

Figure 3-1. Two Illustrations of Wavefront Distortion.

While this example may have no practical counterpart, it does illustrate an environmental source of pointing error that behaves much like the radome. (This example is also similar to propagation through a stratified atmosphere.)

The separation of colors when white light strikes an optical prism illustrates still another property of environmental sources of pointing error. Color separation is due to variation of the prism dielectric constant with frequency. This causes the exit angle from the prism to vary with frequency (color). For white light incident at a given angle, the angle to the source, as indicated by an optical sensor behind the prism, would depend on the frequency to which the sensor is sensitive. All of the previously mentioned environmental sources of pointing error are frequency dependent (some quite strongly).

As a preview to the remainder of the chapter, consider a uniform plane wave incident on a radome as illustrated in Figure 3-1(b). As was seen in the discussion of plane waves incident on planar dielectric slabs, the wave transmitted through the radome will have amplitude and phase that varies with the angle between the radome surface normal and the incident rays. Variation in the amplitude of the transmission coefficient causes the transmitted wave to be non-uniform. Variation in the phase (time delay) of the transmission coefficient causes the wave to be non-planar.

Both of these forms of distortion lead to radar pointing error in the monopulse radar which is designed to operate with uniform plane waves incident at the antenna. Throughout this work it is assumed

that radome-induced distortion is the only source of error present; that is, all radar elements and other propagation considerations are assumed to be ideal.

WAVEFRONT DISTORTION DUE TO TRANSMISSION

In the receiving formulation of the radar problem, the radar response is calculated from the fields incident on the antenna aperture and known characteristics of the antenna. A radome around the antenna introduces distortion into the wave that is incident on the antenna. The first distortion mechanism to be considered here treats the radome as locally planar and modifies the incident wave with a transmission coefficient to obtain the transmitted wave. Ray tracing is then carried out to account for propagation to the antenna aperture.

The radome and incident field are depicted in Figure 3-2. The incident wave is regarded as being made up of parallel rays traveling perpendicular to the wavefront. The radome is treated as being locally flat in the region near the intersection of a ray and the radome surface. This planar approximation to the radome surface is oriented to coincide with the plane tangent to the radome surface at the ray-radome intersection point, and the thickness of the planar slab approximation is the same as the radome wall thickness at the intersection point.

The incidence angle, θ_i , for a given ray is determined by equation (2.105). Parallel and perpendicular components of the incident field are formed with respect to the plane of incidence as outlined in Chapter II. The parallel and perpendicular components of the incident field are then weighted by the appropriate plane wave transmission coefficients

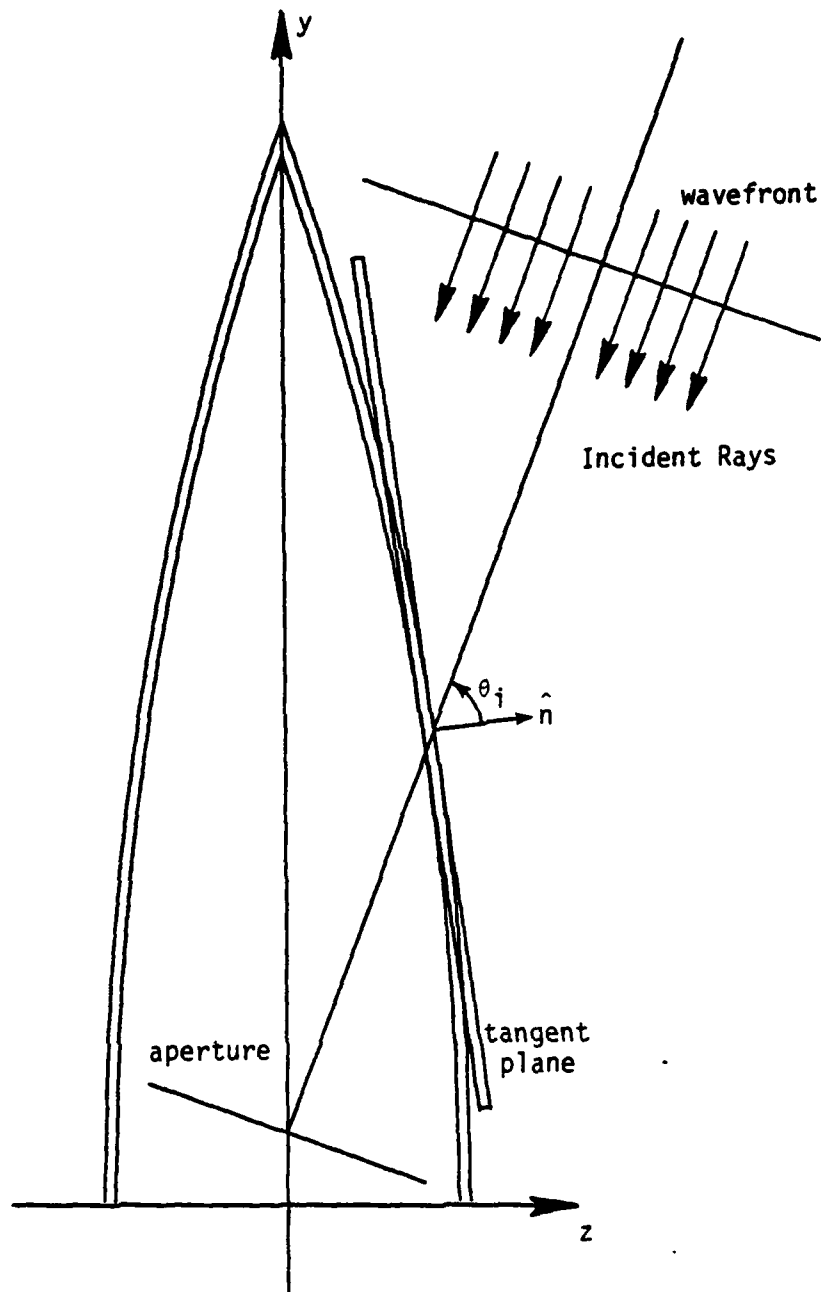


Figure 3-2. Tangent Plane Approximation of Radome Wall.

for the planar slab. These weighted fields now make up the field transmitted to the radome interior.

The ray thus transmitted to the radome interior is traced, without deviation, straight to the antenna aperture. This is, of course, an approximation as was discussed in the previous chapter. The field over the entire antenna aperture is obtained by considering each of the rays in the incident wave that passes through the aperture. The appropriate tangent plane approximation of the radome wall must be determined for each ray, since the direction of the surface normal varies over the radome. With this description of the ray tracing procedure as background, a more explicit description of the details is now given.

The tangent ogive has been previously discussed, and the same conventions and notations will apply to the present discussion. The axis of the ogive will be taken as the y-axis. The y coordinate of a point on the ogive surface with x and z coordinates given by x and z is found from,

$$y = [R^2 - (\sqrt{x^2 + z^2} + R - \frac{w}{2})^2]^{\frac{1}{2}}, \quad (3.1)$$

where $\sqrt{x^2 + z^2}$ is recognized as the perpendicular distance from the y-axis, and other variables are as defined for equation (2.44).

A separate coordinate system will be used for the antenna aperture. The rectangular coordinate axes of this system are designated x' , y' , and z' , and the axis of the aperture is taken to be the y' axis. The origin of the $x'y'z'$ system will lie on the ogive axis. Figure 3-3 shows an outline of the ogive and the antenna aperture with their respective coordinate axes.

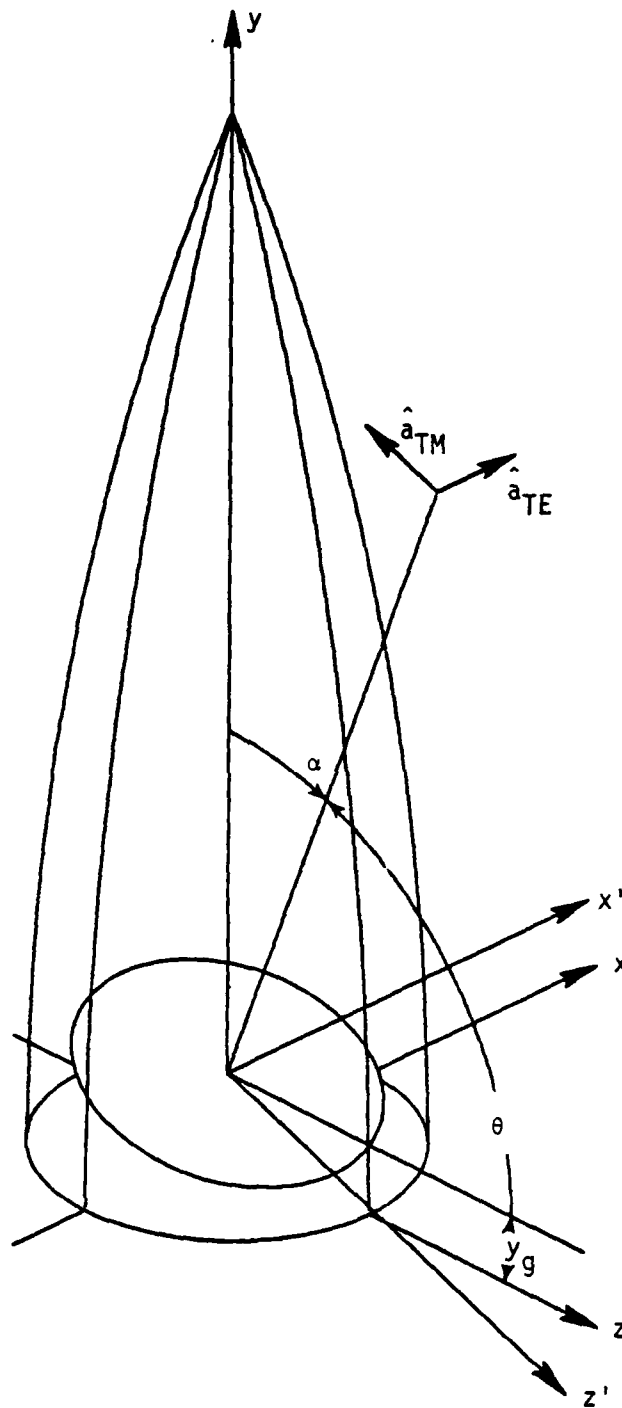


Figure 3-3. Outline of Tangent Ogive Radome with Ray To Aperture Center.

The origin of the aperture is translated with respect to the ogive origin so that clearance with the missile body is achieved for large aperture scan angles. The symbol y_g is used for this translation.

The aperture can be rotated about its x' and z' axes to direct the antenna in any direction in the forward half-space. The order and directions of these rotations are significant, and the convention adopted here will be to rotate first about the x' -axis and then about the z' -axis. Positive rotation will mean that the rotation of the primed coordinate system with respect to the unprimed coordinate system is in the direction that the fingers of the right-hand curl when the right thumb is directed in the positive coordinate direction of the axis of rotation. The symbol α will be used to denote the positive rotation angle about the x' -axis, and β will denote the positive rotation angle about the z' -axis. The angle α is shown in Figure 3-3 and β is zero.

It is important to be able to locate points with primed coordinates in the unprimed coordinate system. The transformation that accomplishes this is given by,

$$\begin{bmatrix} x \\ y \\ z \end{bmatrix} = \begin{bmatrix} \cos\beta & -\sin\beta & 0 \\ \cos\alpha \sin\beta & \cos\alpha \cos\beta & -\sin\alpha \\ \sin\alpha \sin\beta & \sin\alpha \cos\beta & \cos\alpha \end{bmatrix} \begin{bmatrix} x' \\ y' \\ z' \end{bmatrix} + \begin{bmatrix} 0 \\ y_g \\ 0 \end{bmatrix} \quad (3.2)$$

Without loss of generality, the incident rays will be assumed to be parallel to the yz -plane since the coordinate axes of the radome can always be rotated to achieve this orientation due to the symmetry of the radome. A rotation of the antenna aperture about its y' -axis would

be necessary to consider waves incident on the aperture from arbitrary directions, however, since the antenna does not have rotational symmetry due to its polarization and aperture illumination function.

Points on an incident ray obey the equation,

$$y = (z - z_0) \tan \theta + y_0, \quad (3.3)$$

where y and z are coordinates on the ray, y_0 and z_0 are the y and z coordinates respectively of some point on the ray, and θ is the angle of the ray as measured from the xz -plane (the same for all rays since they are parallel) as shown in Figure 3-3 for a ray passing through the aperture center. Of course, all z -coordinates on any particular ray are the same.

In order to obtain the field over the antenna aperture, rays will be traced to the intersection points of a rectangular grid over the aperture. Suppose (x_a, y_a, z_a) is a point in the aperture expressed in the primed coordinate system. The coordinates of (x_a, y_a, z_a) in the unprimed coordinate system are obtained by applying transformation (3.2). The equation for the ray passing through (x_a, y_a, z_a) is given by (3.3) with y_0 and z_0 being replaced by the appropriate transformed coordinates (x_a, y_a, z_a) .

Next the intersection of the ray and the radome must be found. The intersection point must satisfy the equation of the ray, (3.3), and the equation of the ogive, (3.1). Simultaneous solution of these two equations results in finding the roots of a (rather messy) fourth-order equation. Since the x coordinate of the ray is constant, the intersection

point must have this x coordinate. Equation (3.1) thus reduces to a function of one variable that expresses the height of the radome along a slice parallel to the yz-plane as a function of z.

The intersection point is the point where the ray has the same height as the ogive. This point is found numerically by a procedure based on Mueller's method [39] for finding the roots of functions of one variable. Subroutine INTRSC listed in the Appendix performs these computations.

The incidence angle of the ray at the radome is found from a unit vector along the ray and the unit vector normal to the radome at the intersection point. The unit vector, \hat{a} , pointing out of the radome at the intersection point and along any incidence ray is given by,

$$\hat{a} = \sin\theta \hat{y} + \cos\theta \hat{z} \quad . \quad (3.4)$$

A method for finding the unit vector normal to the radome surface has been previously discussed. Subroutine NORM listed in the Appendix makes the calculations necessary to find this vector. The incident angle of the ray is then given by,

$$\theta_i = \cos^{-1} [\hat{a} \cdot \hat{n}] \quad , \quad (3.5)$$

where θ_i is the incident angle, and \hat{n} is the unit surface normal at the intersection point.

The polarization of the incident wave is transverse to the direction of propagation since this field is a uniform plane wave. Two principal polarization directions will be considered here. These

polarization directions are defined with respect to the yz -plane and form a basis to express an arbitrarily polarized incident field. An incident field will be said to be TE polarized (for Transverse Electric) if its electric field lies transverse to the yz -plane, that is in the \hat{x} direction, for any incident angle θ .

An incident field is TM polarized (for Transverse Magnetic) if its electric field is parallel to the yz -plane for any incident direction. Unit vectors in the directions of TE and TM polarized fields are given by,

$$\hat{a}_{TE} = \hat{x} \quad , \quad (3.6)$$

for the TE field, and

$$\hat{a}_{TM} = \cos\theta \hat{y} - \sin\theta \hat{z} \quad , \quad (3.7)$$

for the TM field, where θ is the previously defined angle of the incident rays. These unit vectors are indicated in Figure 3-3.

Any incident polarization can be expressed as a sum of TE and TM components with appropriate amplitude and phase. Waves polarized in only the TE or TM directions will first be considered. Later waves with diagonal linear polarization and circular polarization are discussed.

The procedure for obtaining the fields transmitted through the radome and directly incident on the aperture is summarized as follows. Beginning at a point in the aperture with known aperture coordinates, the radome coordinates of the point are found. Next a ray is constructed through the aperture point. The intersection of this ray with

the radome wall is found numerically. At the ray-radome intersection the radome wall is approximated by a planar slab, and the ray angle of incidence is found from the dot product of the unit surface normal and a unit vector in the ray direction.

The incident field at the ray-radome intersection is decomposed into parallel and perpendicular components with respect to the local plane of incidence as prescribed by equations (2.101) and (2.102). The transmitted field is then found by multiplying the incident field components by the appropriate plane-wave transmission coefficients for the planar slab approximation to the radome wall. The transmitted field, \bar{E}^t , is given by

$$\bar{E}^t = \hat{t}_1 \bar{E}_1 + \hat{t}_{11} \bar{E}_{11}^i, \quad (3.8)$$

where \bar{E}_1^i and \bar{E}_{11}^i are the perpendicular and parallel components, respectively, of the field incident at the aperture point in the absence of the radome; and \hat{t}_1 and \hat{t}_{11} are the insertion transmission coefficients for perpendicular and parallel polarization, respectively, as given by (2.108) and (2.107).

It has been previously noted that \hat{t}_1 and \hat{t}_{11} are, generally, unequal functions of incident angle. Because the radome surface is curved the local ray incident angle will, in general, be different for any two different rays. Thus, equation (3.8) indicates that the phase and amplitude of the transmitted field will vary over the antenna aperture. Furthermore, since the radome surface is curved, the parallel and perpendicular components of the incident field will be different for

AD-A085 263

AUBURN UNIV ALA ENGINEERING EXPERIMENT STATION

F/G 17/9

INVESTIGATION OF COMPLEX ANGLE PROCESSING TO REDUCE RADOME INDOU--ETC(11)

OCT 79 D G BURKS, E R GRAF

DAAK40-77-C-0022

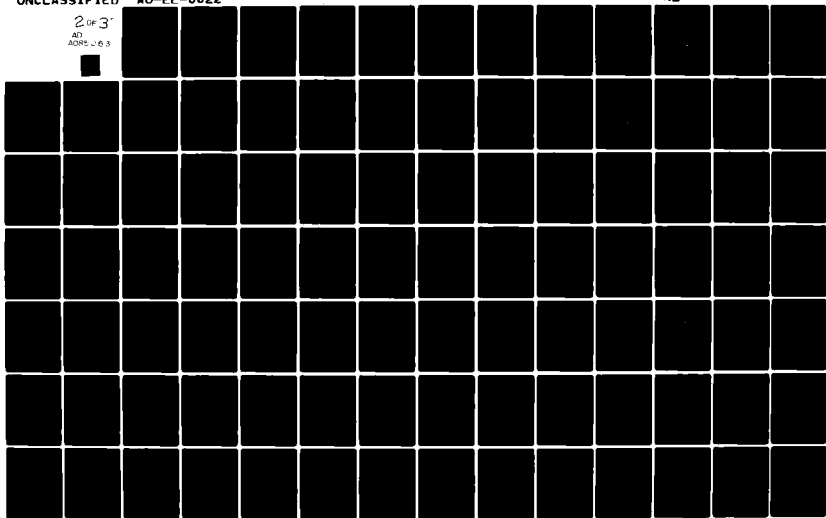
UNCLASSIFIED

AU-EE-0022

NL

2 OF 3

AD
A085 263



different rays in the aperture. The above phenomena are summarized by the expression: wavefront distortion due to transmission.

An example is presented to illustrate the ray-tracing technique. The radome considered is a tangent ogive with length of $30\lambda_0$ and a base diameter of $10\lambda_0$ for a fineness ratio of 3. The radome wall is taken to be a lossless non-magnetic homogeneous dielectric with relative permittivity of 4. The wall has a constant thickness of $0.2855\lambda_0$ which is the thickness of a planar slab designed for 100% transmission at an incidence angle of 75° . The transmission curves for this dielectric were presented in Figure 2-15. A design angle of 75° was selected since it is near the mean of the actual ray incidence angles of a wave that is incident along the axis of an ogive with fineness ratio of 3. Most of the rays in this case are incident at angles ranging from 70° to 80° .

Primary emphasis in this section will be placed on the phase of the field over the antenna aperture. As can be seen from the transmission curves, the amplitude of the transmission coefficients remain near unity over the entire range of the angles encountered; however, the phase of the transmission coefficients varies about 20° over this same range. The amplitude of the field over the aperture is thus approximately constant, but the phase is not. Since the monopulse radar indicates the direction to the target as perpendicular to the weighted phase slope, the phase of the fields incident on the aperture is of extreme importance.

As noted earlier, only linear polarization in the TE and TM directions will be considered initially and the phase of the incident field

across the antenna aperture will be found for a given polarization and incidence angle. The slope of the phase-front across the aperture leads to radar pointing errors and this phase front distortion varies with incidence angle. Radar pointing errors have a corresponding angular dependence. Thus, considerable insight into radome-induced radar pointing error is provided by the phase front across the aperture.

Figures 3-4 through 3-8 contain the insertion phase delay for TE polarized rays traced through the radome to the aperture, plotted as a function of position in the aperture. This series of figures has a progressively lower angle of incidence (θ) with the incidence angle noted on each figure. The small diagram in the upper-right-hand corner of each figure is similar to Figure 3-3 and shows the incidence angle for a ray to the aperture center as well as the coordinate axes. Also indicated on the small figure is the polarization of the incident field.

For each of these figures the aperture was rotated to be normal to the incident rays. Thus, each figure can be considered as the phase front of the distorted wave across the aperture when the antenna is adjusted for zero pointing error.

The aperture used for these figures has a diameter of 8λ and the IPD of a ray is plotted above the base plane only for rays incident on the aperture. The height of the antenna gimbal point above the radome base (y_g in Figure 3-3) is $2\lambda_0$, and the small figure shows this to scale. The grid spacing in this series of figures is $\lambda_0/2$.

Several attributes of these figures should be pointed out. First the IPD is symmetric about the $x' = 0$ plane. This is due to the mirror

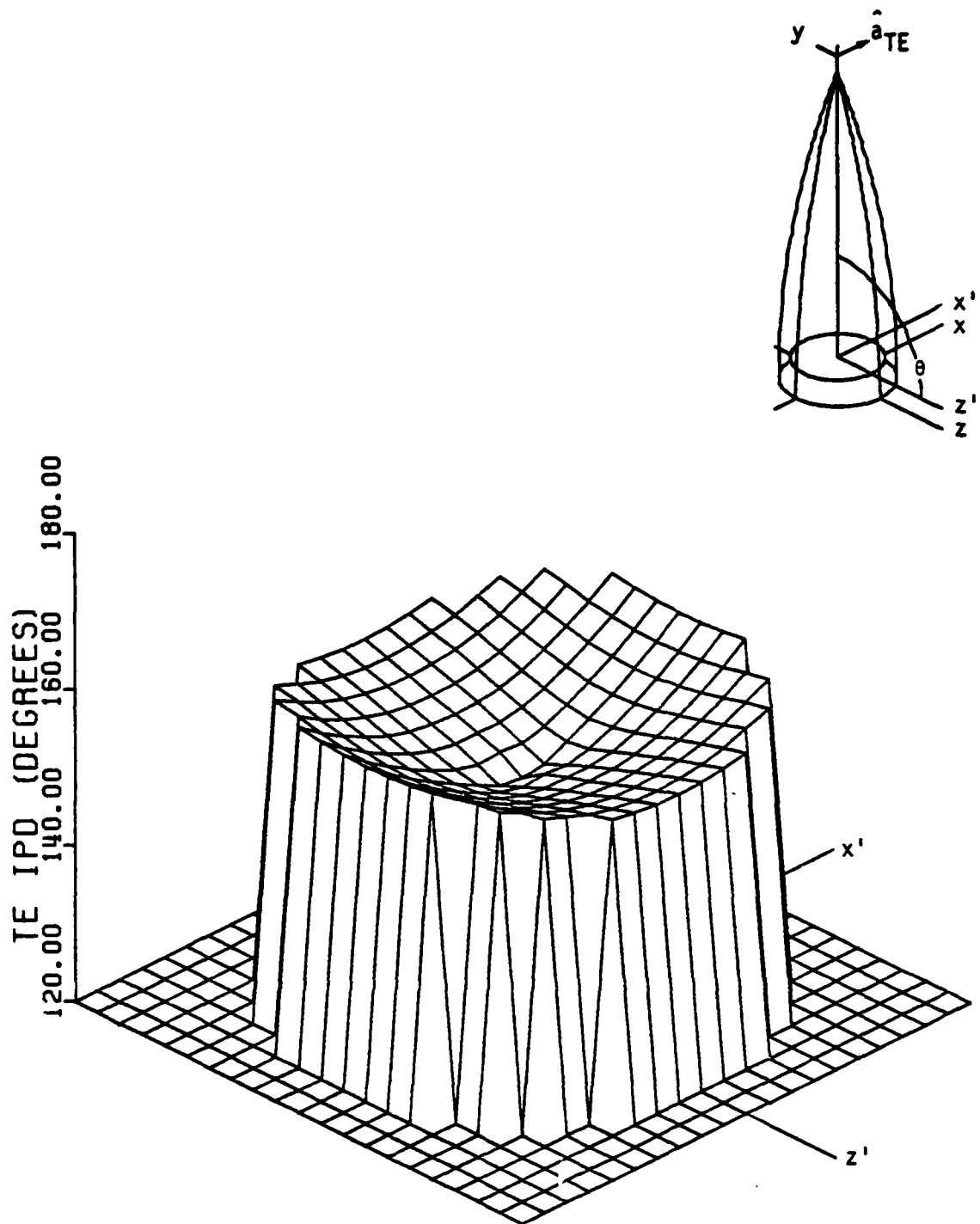


Figure 3-4. Insertion Phase Delay of TE Polarized Field with 90° Incidence Angle.

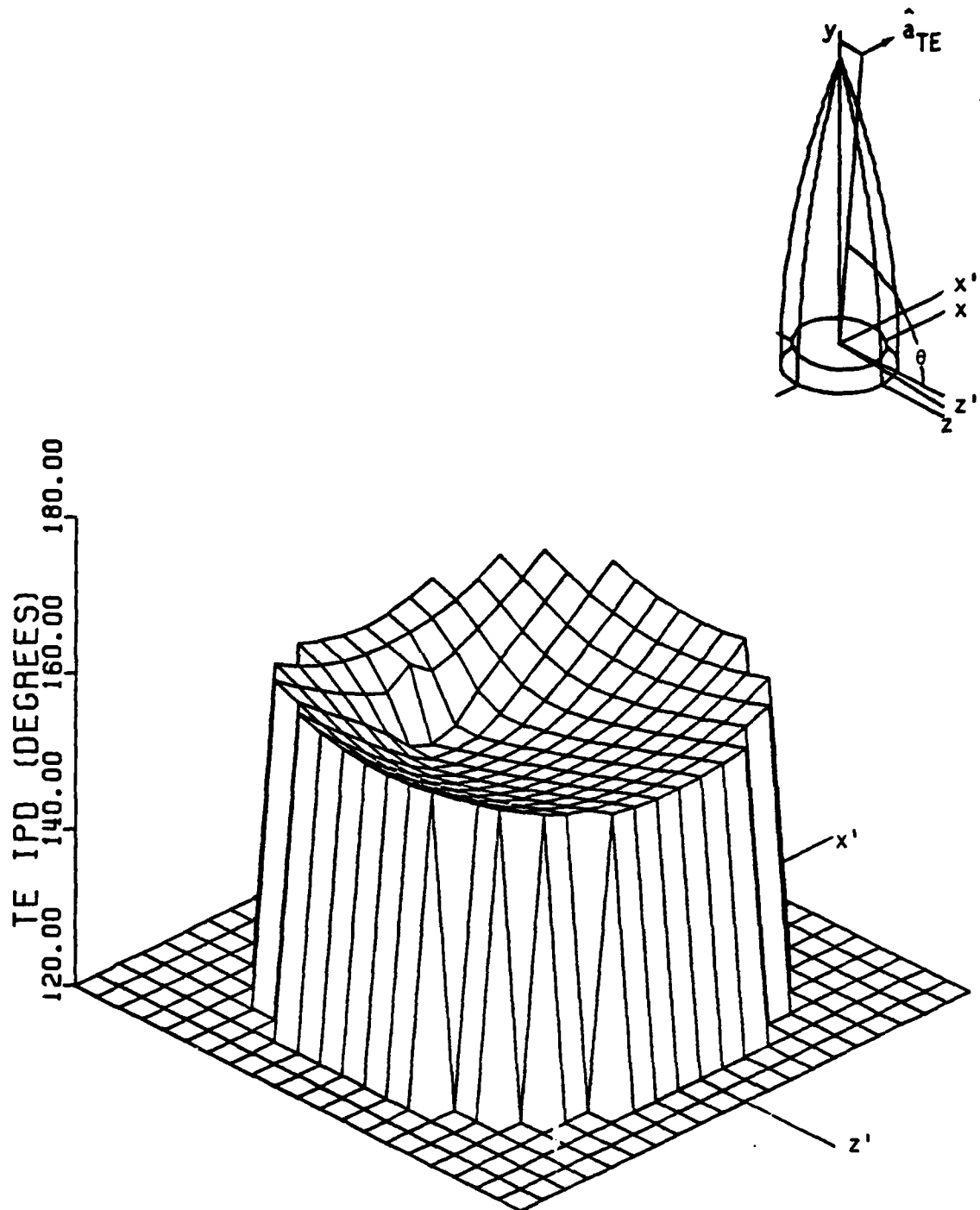


Figure 3-5. Insertion Phase Delay of TE Polarized Field with 85° Incidence Angle.

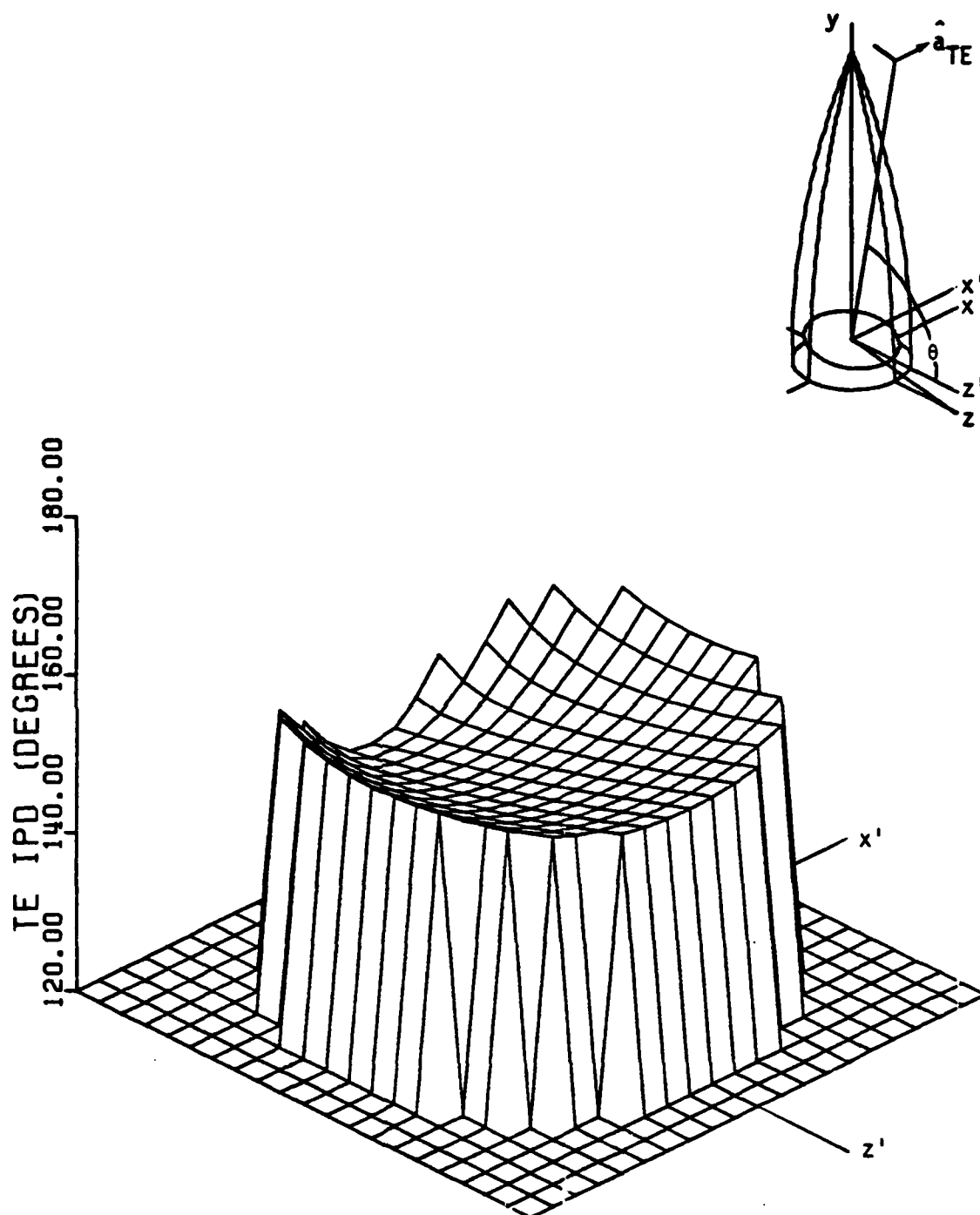


Figure 3-6. Insertion Phase Delay of TE Polarized Field with 80° Incidence Angle.

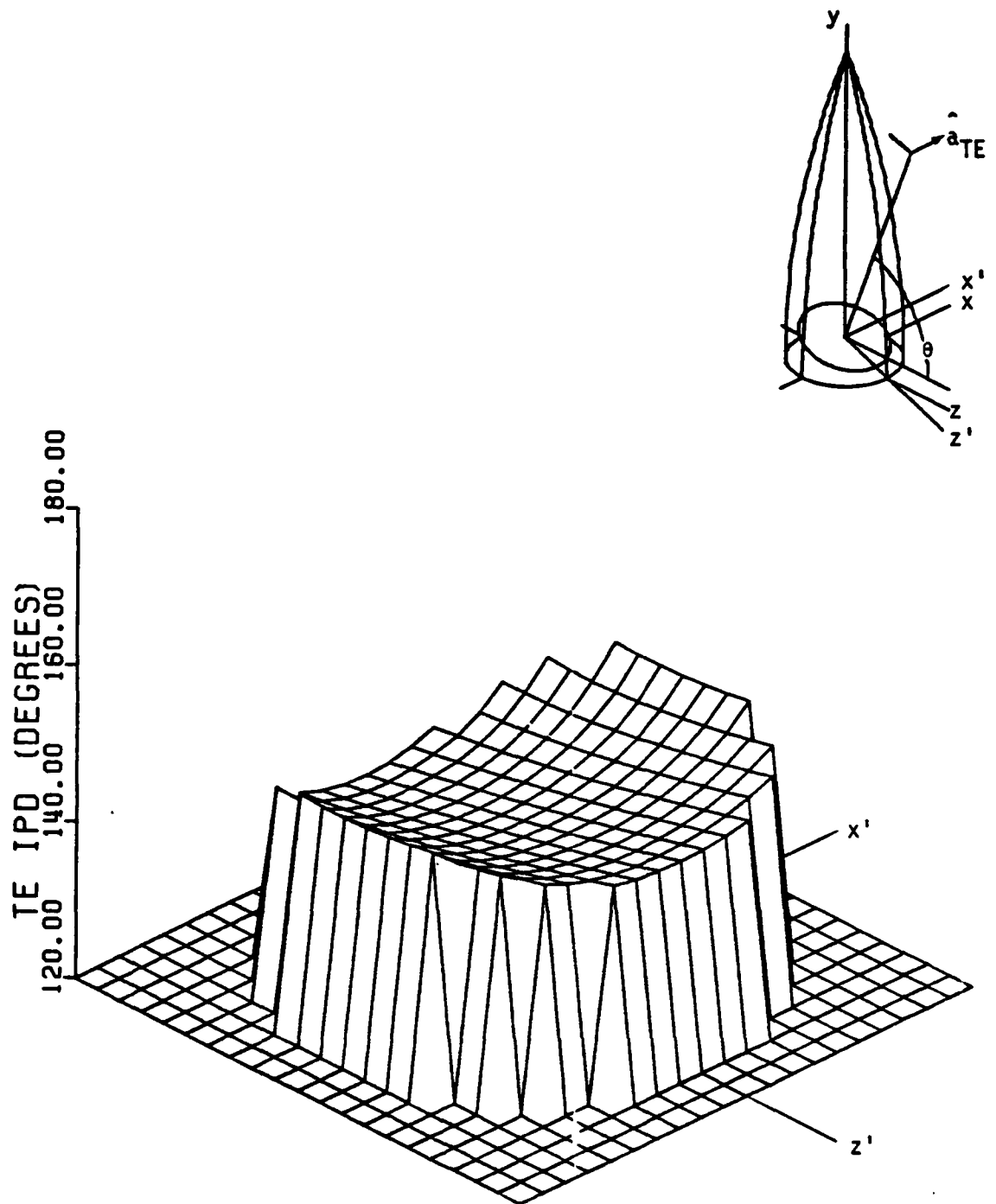


Figure 3-7. Insertion Phase Delay of TE Polarized Field with 70° Incidence Angle.

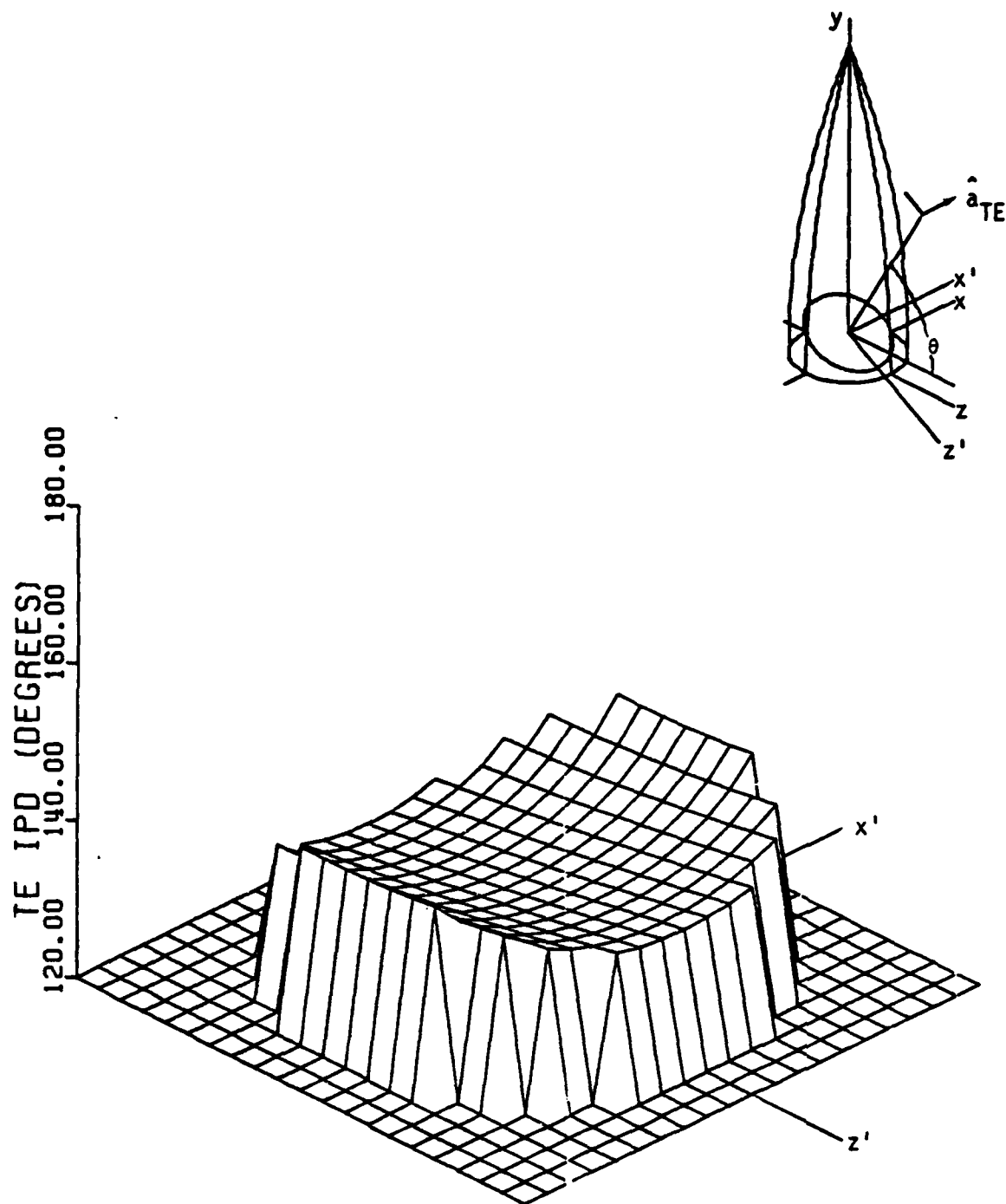


Figure 3-8. Insertion Phase Delay of TE Polarized Field with 60° Incidence Angle.

symmetry of the radome and incident polarization about this plane. The shadow of the radome tip is observed in Figure 3-4 as the point of minimum phase delay since the lowest angle of incidence occurs for the ray passing through the tip. The phase front is observed to increase from the center due to the increase in the angle of incidence of the corresponding rays and the monotonic increase in the IPD with incidence angle for this radome wall.

In Figure 3-5 the shadow of the radome tip is seen about midway between the aperture center and edge as the point of minimum phase delay. At 80° incidence the tip shadow has moved out of the aperture, but the phase front is still observed to slope down toward that point. At the lower angles of incidence the phase front is seen to have less variation over the aperture because the incident rays are now passing through the (relatively flatter) side of the radome.

Also it will be noted that as the incidence angle decreases the average height of the IPD across the aperture decreases. Again this is due to the monotonic variation of the IPD with incidence angle over the range of angles encountered.

Next a TM polarized incident wave is considered. Figures 3-9 through 3-13 show the IPD for this polarization with all other parameters as in Figures 3-4 through 3-8. Again the IPD is noted to be symmetric about the $x' = 0$ plane due to the symmetry of the incident field and the radome. At on-axis incidence TE and TM IPD differ only by a 90° rotation about the y axis. However, at non-axial incidence the TE and TM IPD are different. It will be seen later that radar pointing error can be a strong function of polarization at certain incidence angles.

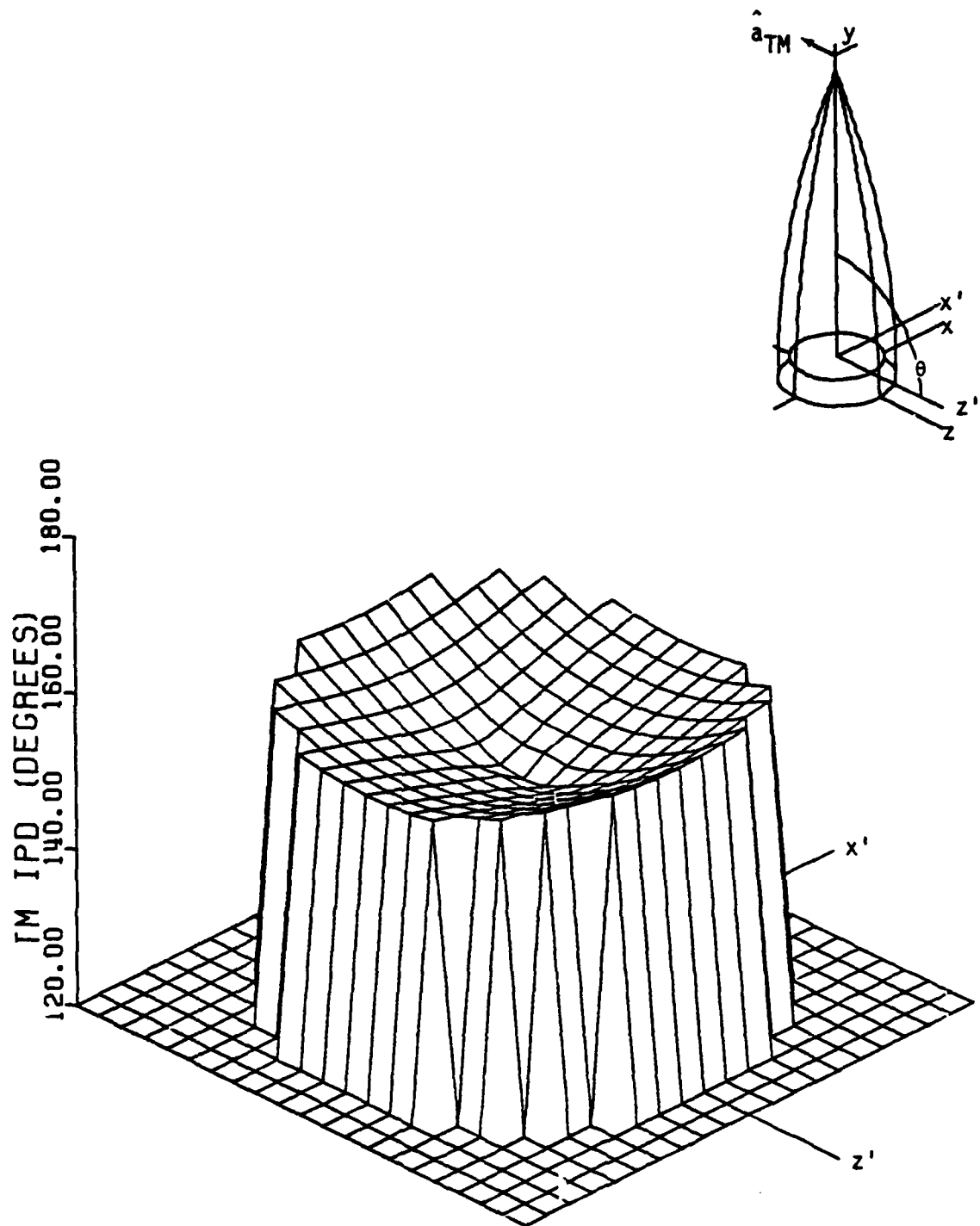


Figure 3-9. Insertion Phase Delay of TM Polarized Field with 90° Incidence Angle.

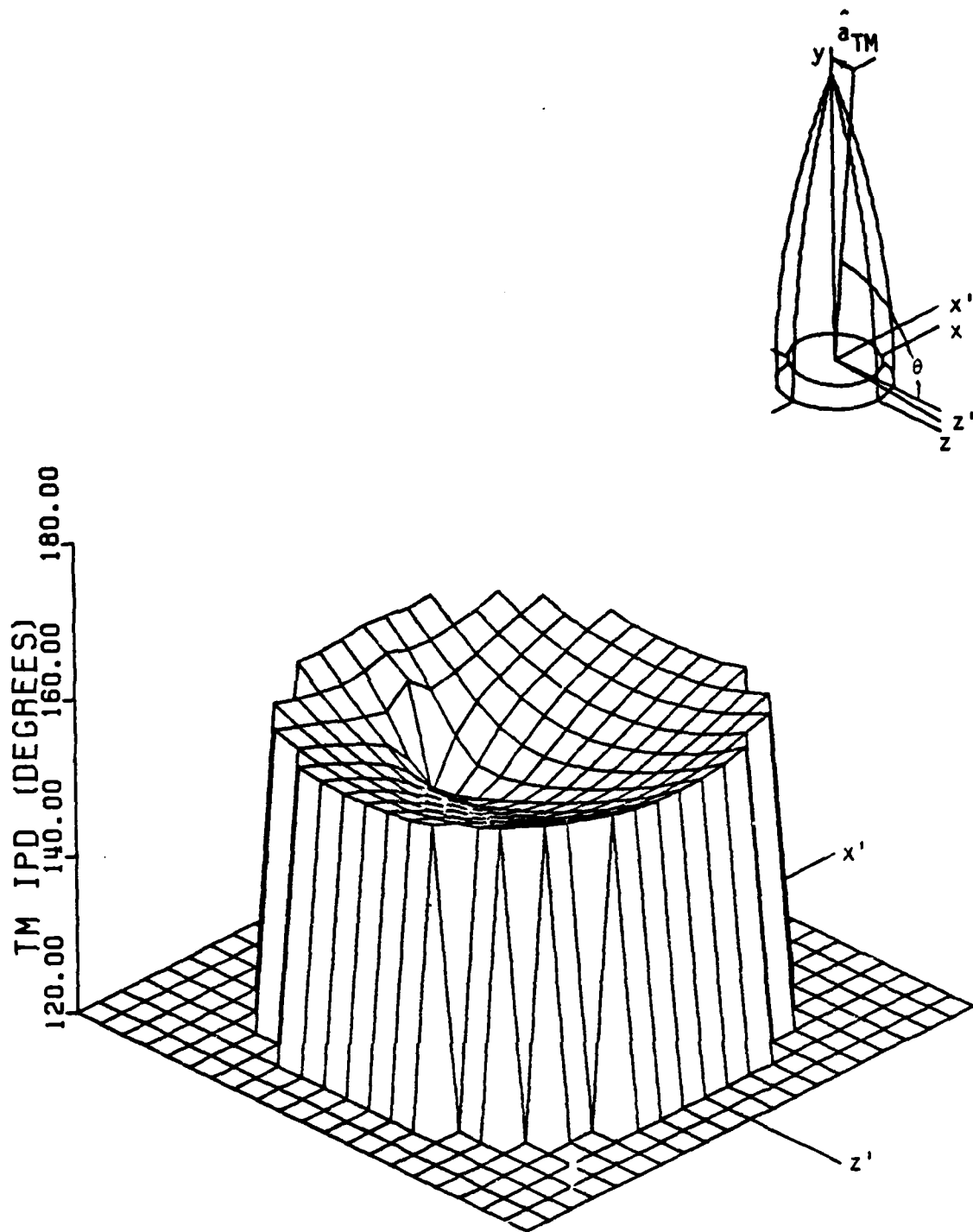


Figure 3-10. Insertion Phase Delay of TM Polarized Field with 85° Incidence Angle.

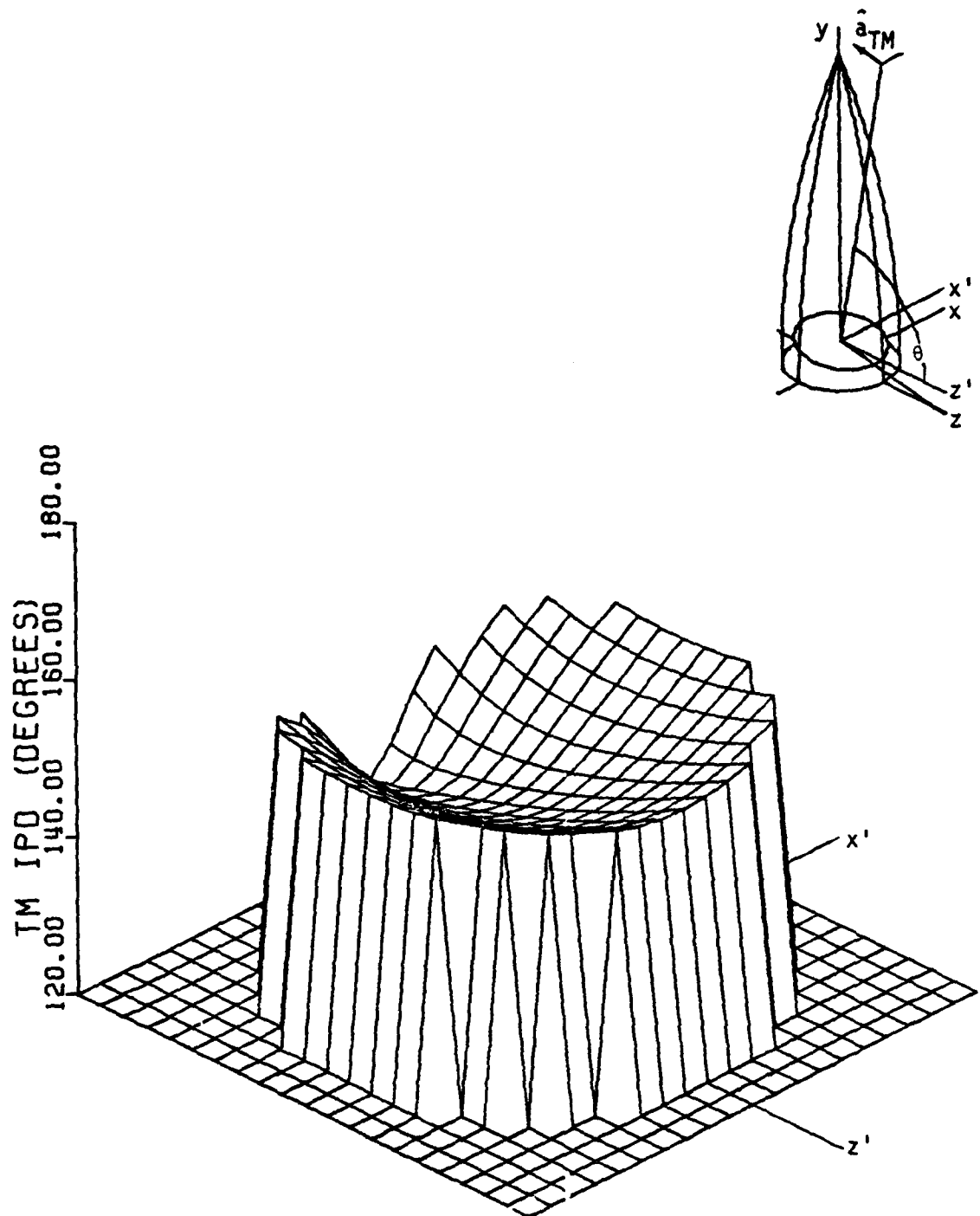


Figure 3-11. Insertion Phase Delay of TM Polarized Field with 80° Incidence Angle.

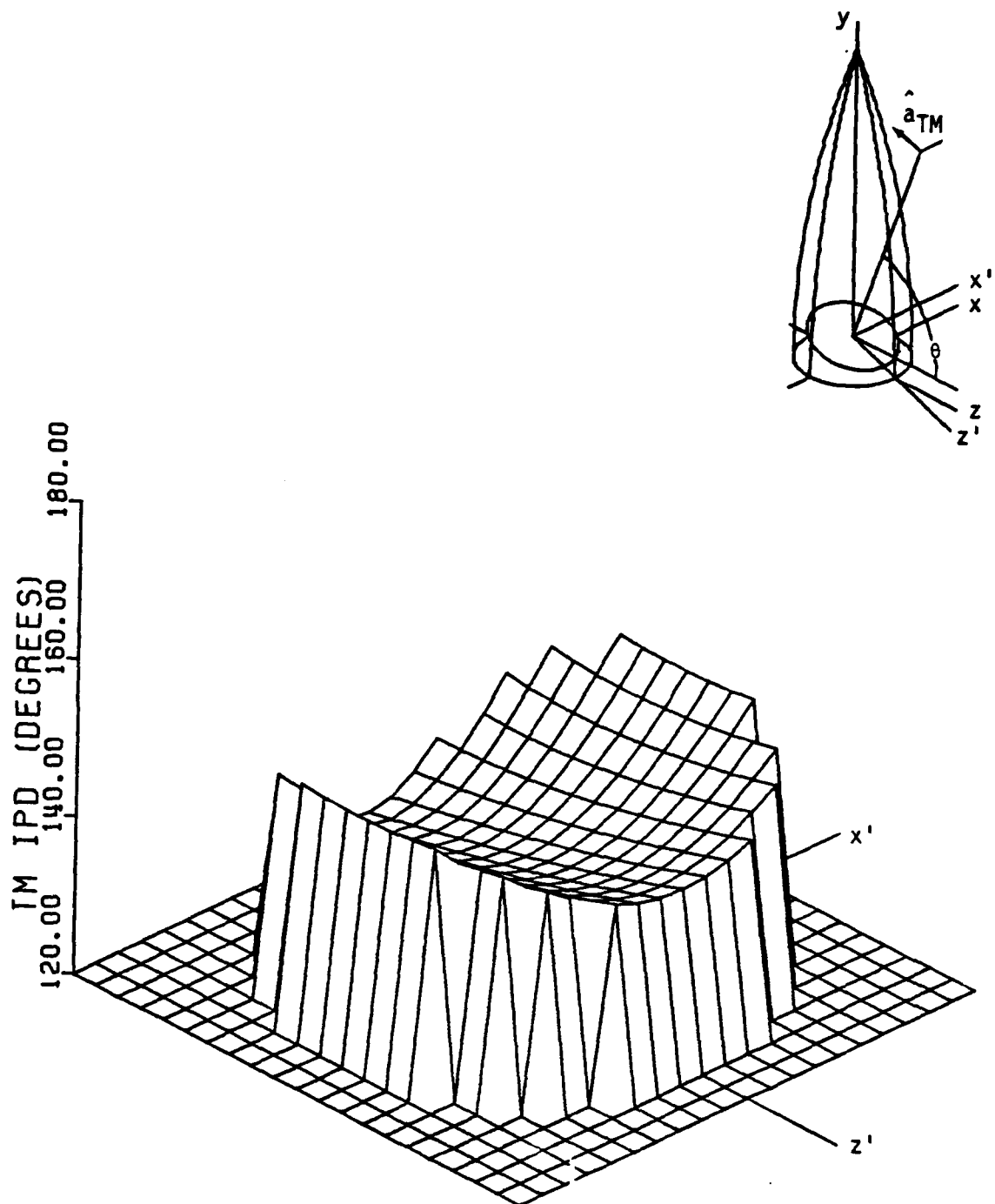


Figure 3-12. Insertion Phase Delay of TM Polarized Field with 70° Incidence Angle.

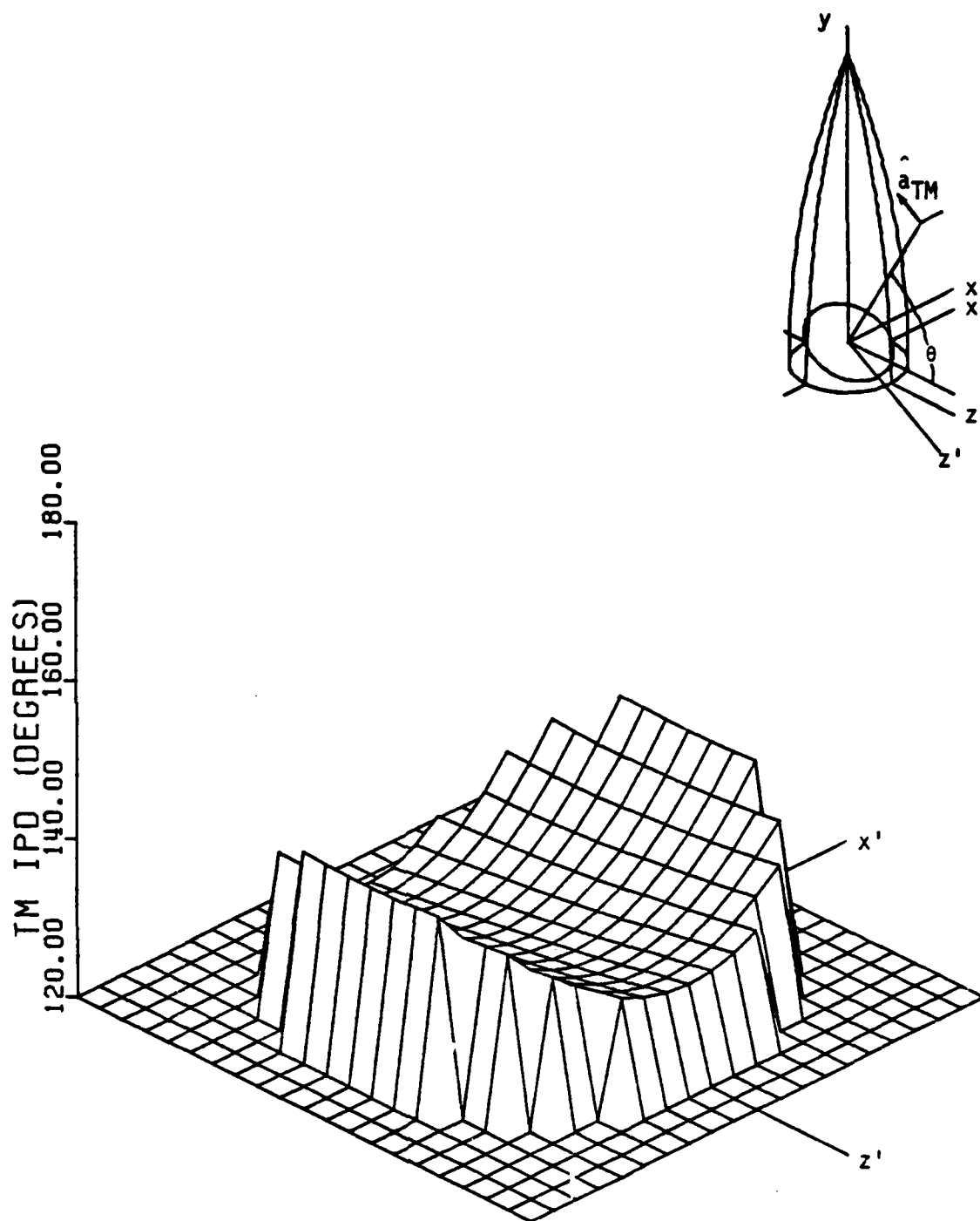


Figure 3-13. Insertion Phase Delay of TM Polarized Field with 60° Incidence Angle.

Another example will be considered to illustrate some additional properties of wavefront distortion due to transmission. In the previous example, it was noted that the insertion phase delay of the planar slab designed for 100% transmission at 75° is a monotonic increasing function of incidence angle over the range of angles encountered (less than 80°). This feature is responsible for the concave phase front over the aperture at normal incidence. The effect of changing the wall thickness is now to be considered.

In this example the radome wall is considered to be polyimide quartz, a common material used for radome construction due to its good mechanical and thermal properties along with good electrical characteristics. Polyimide quartz is non-magnetic, has a relative permittivity of about 3.2, and a loss tangent of about 0.008 at x-band. A wall thickness was selected for a 60° design angle using equation (2.99) and ignoring losses. The transmission coefficients for this wall are shown in Figure 3-14.

The first thing that should be noted about these transmission curves is that the magnitudes are not unity at the design angle. This is due to the non-zero loss tangent of the material which prevents 100% transmission. Next, the parallel polarization IPD is seen to be increasing for angles up to about 82° , but the perpendicular IPD increases for angles up to only 75° and then begins to decrease. This will be seen to have serious effects on phase front distortion and radar pointing errors.

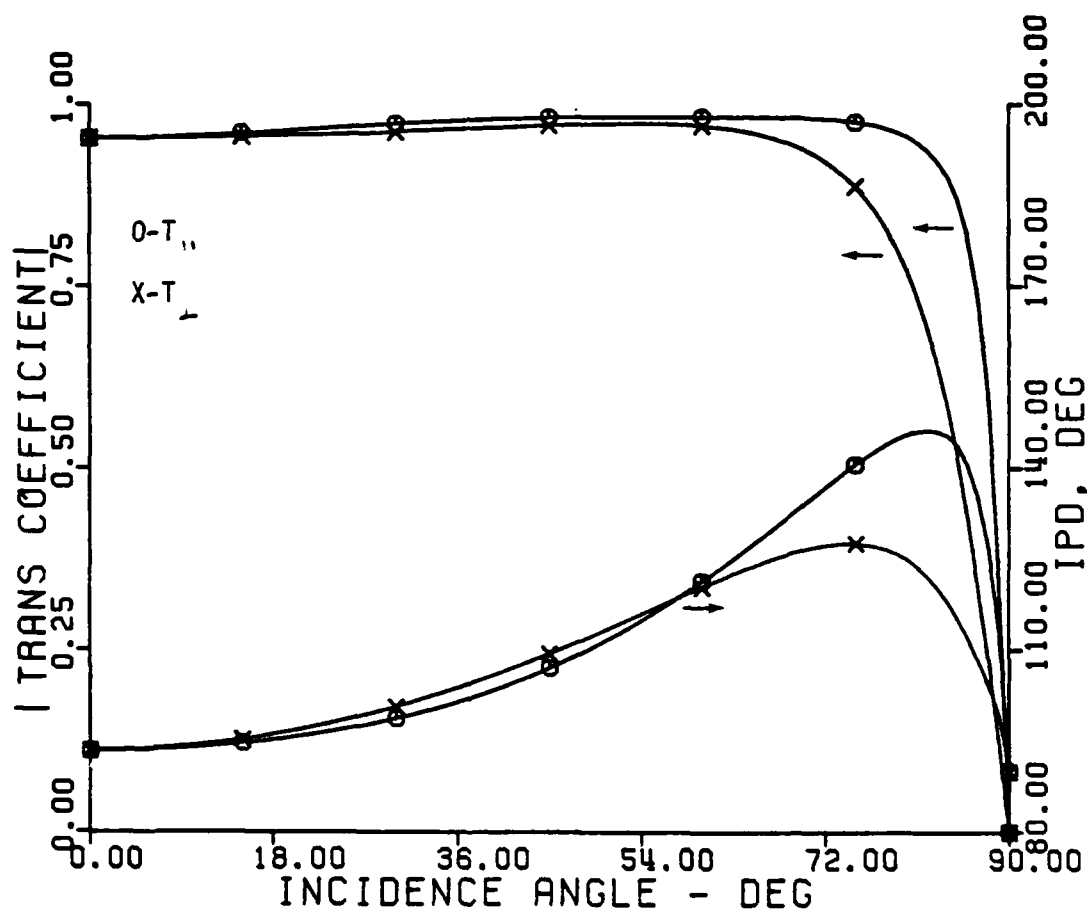


Figure 3-14. Transmission Coefficients of Polyimide Quartz Wall Designed for 60°.

The insertion phase delay through a radome constructed of this new wall material, but with all other parameters as before, is presented for the incidence angle $\theta = 80^\circ$. Figure 3-15 is for TE polarization and Figure 3-16 is for TM polarization plotted as before. A striking difference now exists between the two polarization states. The TE IPD now has an average negative slope in the z' direction but the slope is positive near the z' axis. The slope of the TM IPD is positive in the z' direction.

Since the pointing direction indicated by the radar is related to the slope of the phase front across the aperture, Figures 3-15 and 3-16 show that a reversal in the direction of pointing error can occur at a given incidence angle due to a change in the polarization of the incident field.

The large differences in the slopes of the phase fronts above are due to the differences in the IPD of the planar slab for parallel and perpendicular polarization. For minimum phase distortion the IPD of the two polarizations should be nearly equal over the entire range of incidence angles encountered. By this criterion the 75° design wall is better than the 60° design wall for the tangent ogive radome with fineness ratio of three. Radar pointing error curves confirm this.

So far, incident polarization states that are symmetrical about the radome's $x' = 0$ plane have been presented. This symmetry is not present for linear polarization in any but the pure TE or TM directions. Figure 3-17 illustrates what may be referred to as diagonal polarization for a ray traced to the aperture center. The incident polarization in this case has components in both the TE and TM directions.

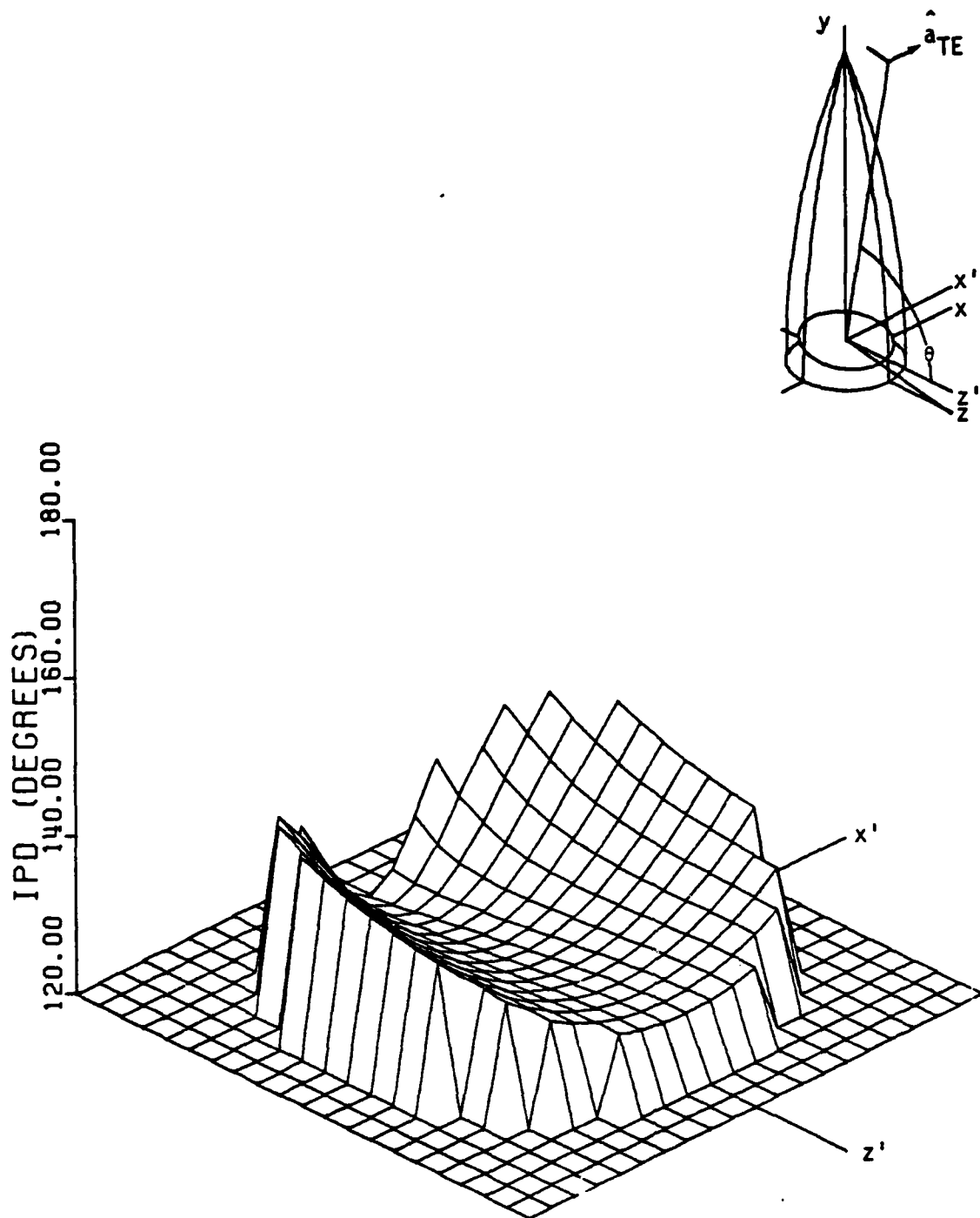


Figure 3-15. Insertion Phase Delay of TE Polarized Field Incident at 80° on Polyimide Quartz Radome.

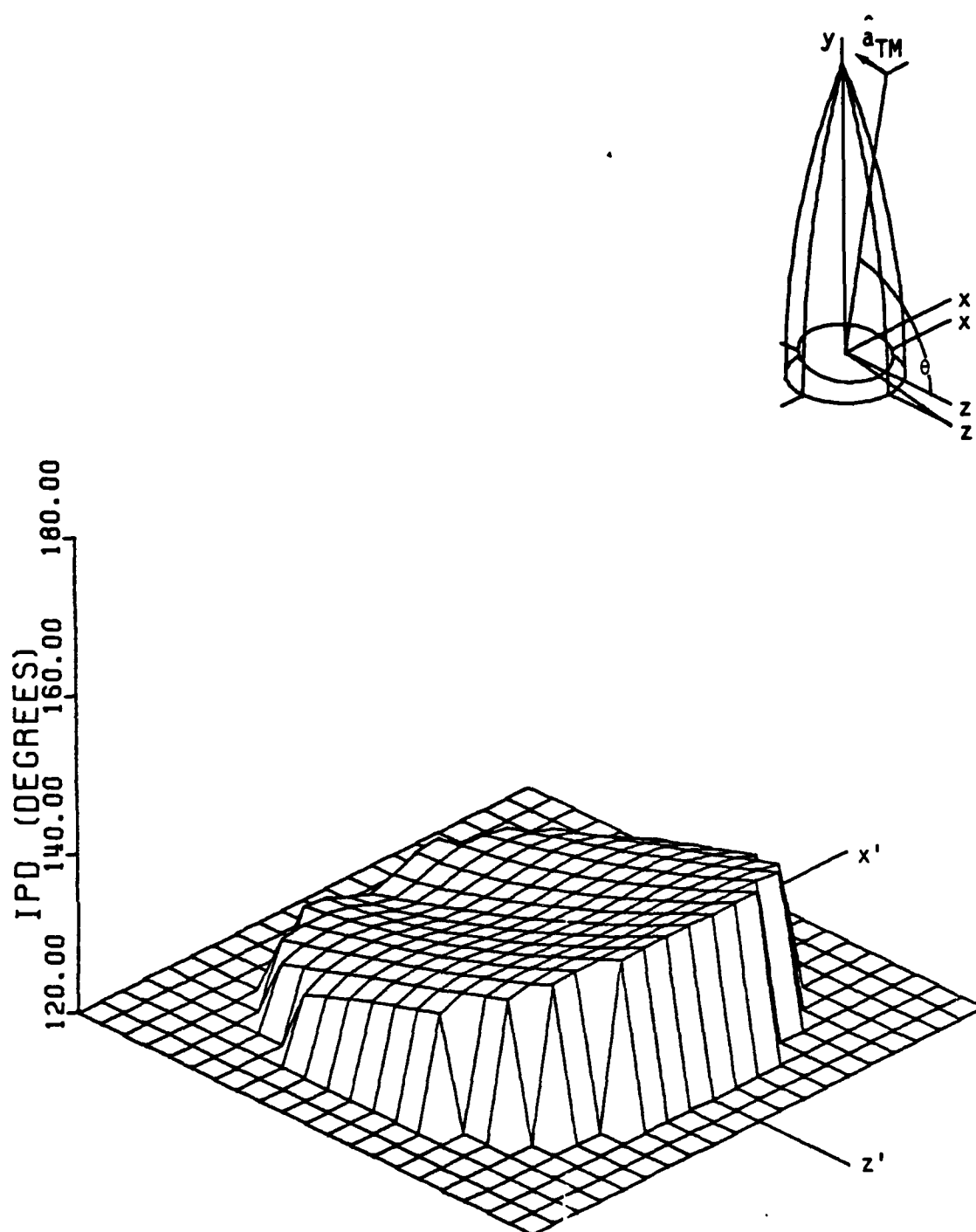


Figure 3-16. Insertion Phase Delay of TM Polarized Field Incident at 80° on Polyimide Quartz Radome.

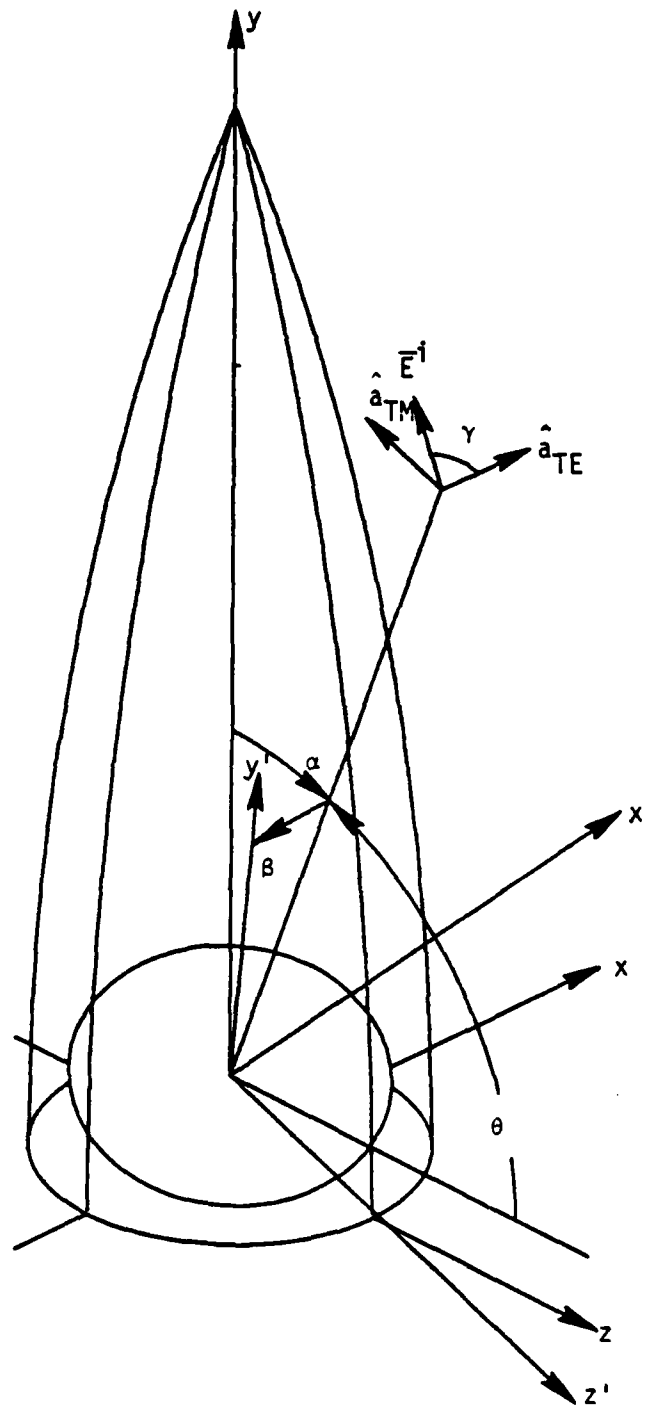


Figure 3-17. Outline of Tangent Ogive Radome Showing Both Scan Angles and the Polarization Angle.

A unit vector, \hat{a}_E , in the direction of the incident field can be expressed as

$$\hat{a}_E = \cos(\gamma) \hat{a}_{TE} + \sin(\gamma) \hat{a}_{TM} \quad , \quad (3.9)$$

where γ is the polarization angle as shown in Figure 3-17, and \hat{a}_{TE} and \hat{a}_{TM} are the previously defined unit vectors in the TE and TM directions respectively.

Since diagonal polarization is not symmetric with respect to the $x' = 0$ plane, there will be differences in the fields transmitted to the $x' > 0$ and $x' < 0$ halves of the antenna aperture. The aperture is free to rotate about its z' axis to track the incident field. (Figure 3-17 shows the aperture rotated through the angle β positively about the z' axis.) Radar response to diagonal polarization will be a pointing error in the β rotation direction as well as the previously mentioned pointing error in the α rotation direction. These pointing errors are related to the phase-front distortion in the x' and z' directions respectively.

To illustrate this phase-front distortion, the insertion phase delay over the antenna aperture is plotted for the polyimide quartz wall for several polarization angles. Figures 3-18, 3-19 and 3-20 show the phase front for polarization angles of 22.5° , 45° and 67.5° respectively. This series of figures have the same parameters as were used in Figures 3-15 and 3-16. The polarization angle is noted on the small inset figure as before.

This series of figures shows a continuous change in the phase front from TE polarization, as was shown in Figure 3-15, to TM polarization as

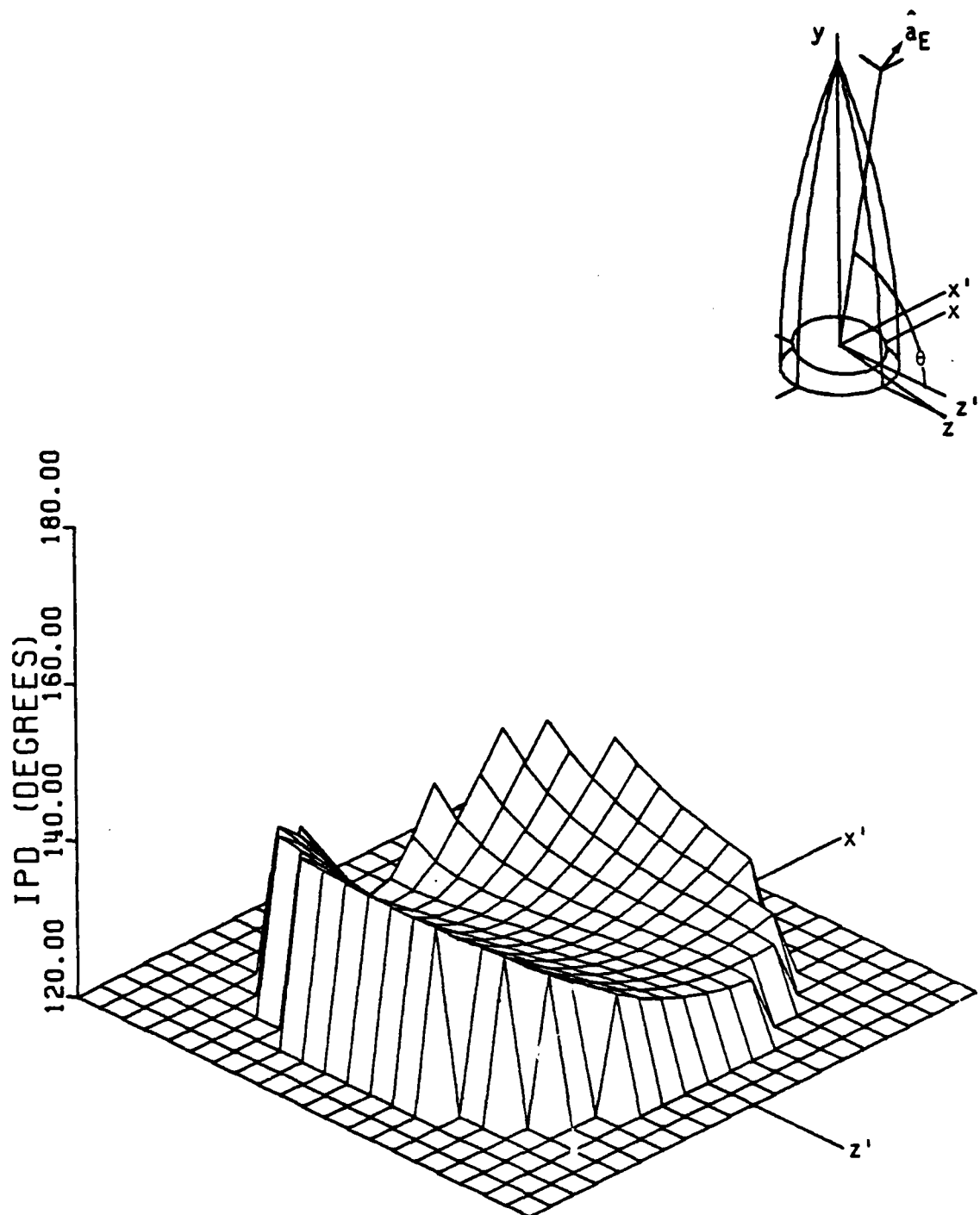


Figure 3-18. Insertion Phase Delay of 22.5° Polarized Field Incident at 80° on Polyimide Quartz Radome.

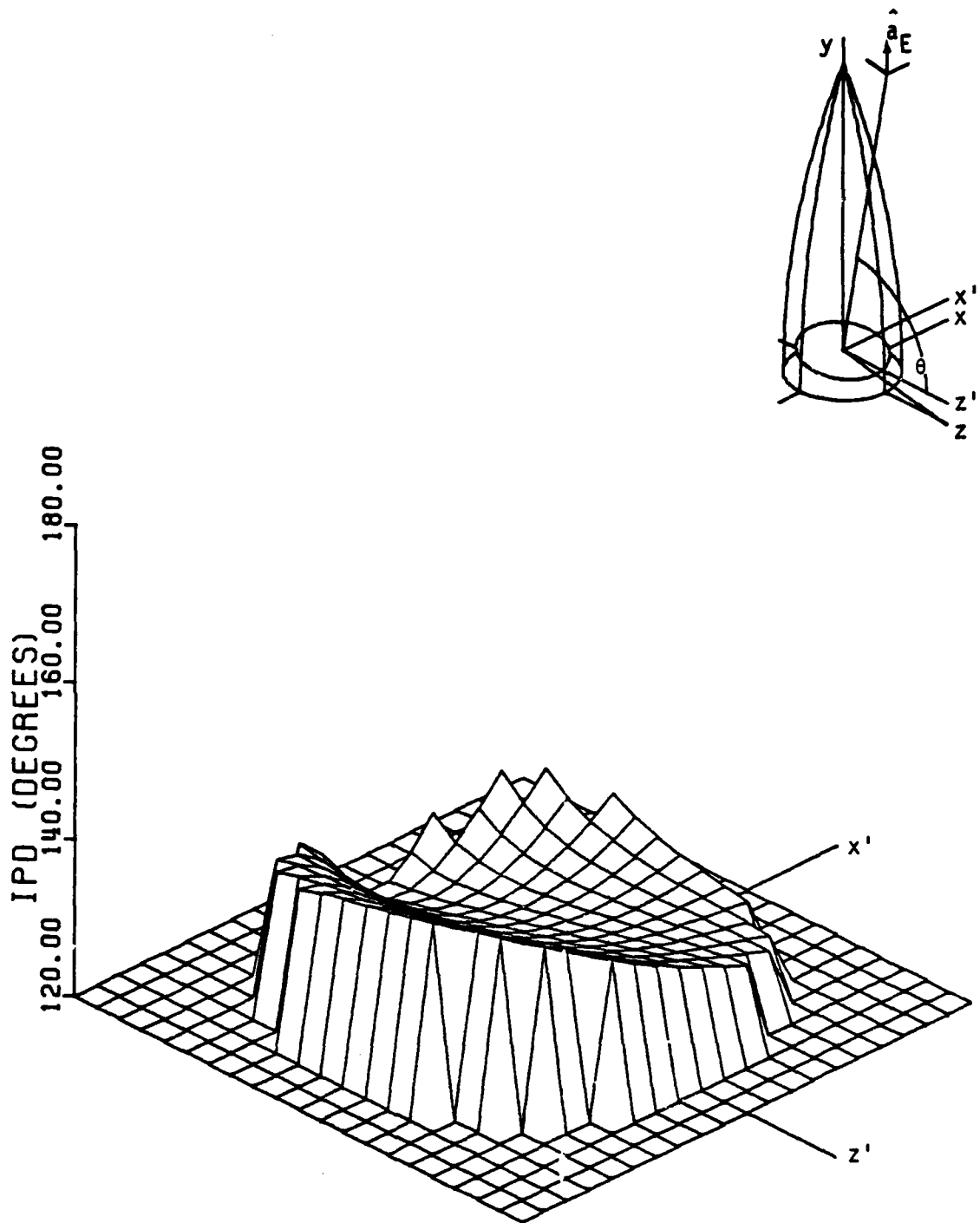


Figure 3-19. Insertion Phase Delay of 45° Polarized Field Incident at 80° on Polyimide Quartz Radome.

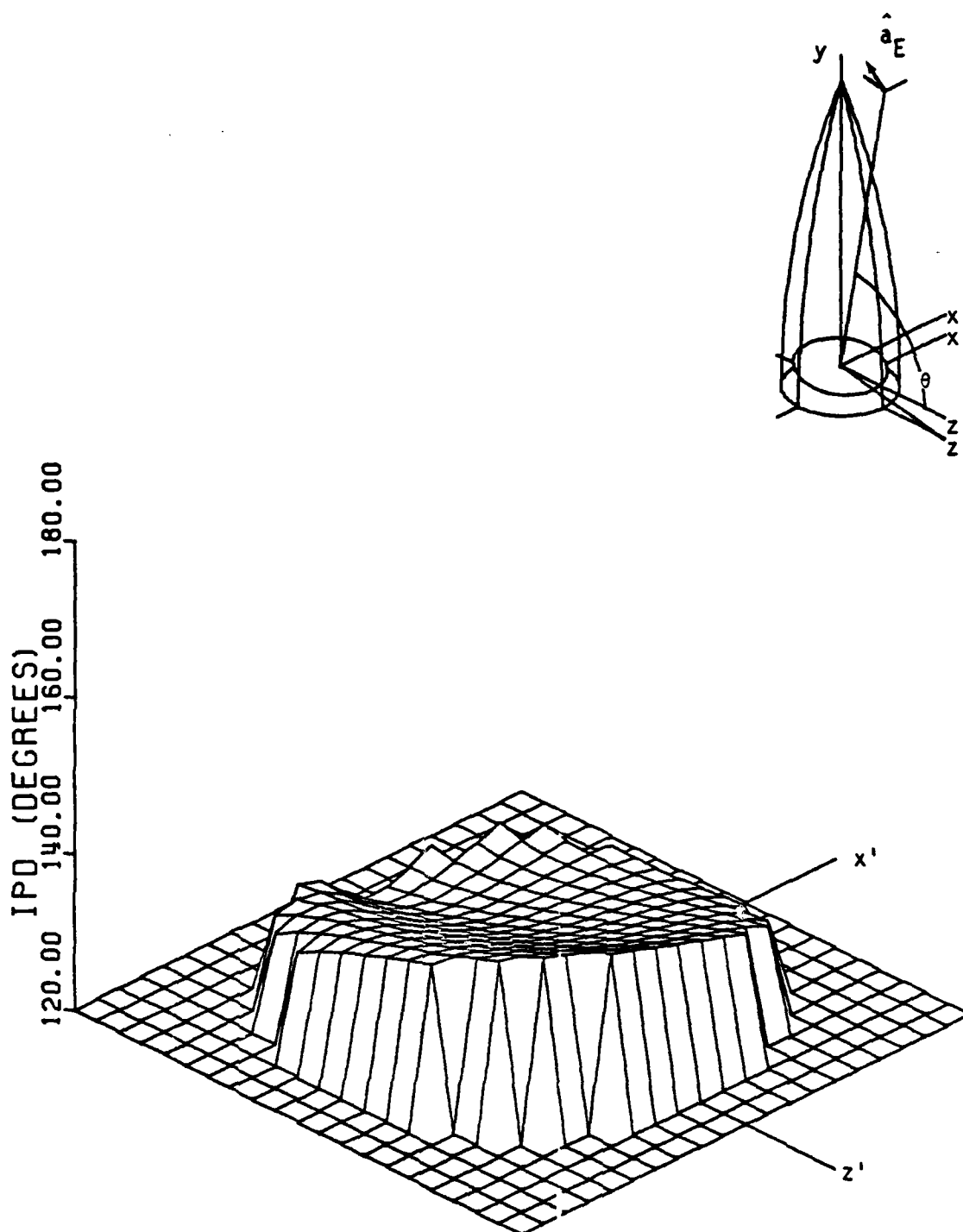


Figure 3-20. Insertion Phase Delay of 67.5° Polarized Field Incident at 80° on Polyimide Quartz Radome.

was shown in Figure 3-16. In fact, all of these figures may be taken together to represent the transition from 0° polarization (pure TE) to 90° polarization (pure TM). Note also that the maximum average phase slope in the x' direction appears at a polarization angle of 45° .

The phase-front plots presented in this section provide considerable insight into radome-induced radar pointing error. They will be referred to when pointing errors are considered, but before doing this another radome distortion mechanism is considered.

WAVEFRONT DISTORTION DUE TO INTERNAL REFLECTION

This section concerns the analysis of the electromagnetic energy that arrives at the antenna aperture after passing through the radome and being reflected from the interior of the radome wall a single time. Ray tracing is used to account for propagation, and the radome wall is approximated by planar dielectric slabs as before.

The geometry for internal reflection is illustrated in Figure 3-21. A direct ray is again shown passing through the radome wall to the aperture center. The second ray shown cannot enter the aperture directly, but enters the aperture after being reflected from the inside of the radome wall. The term internal reflection will be used to refer to illumination of the aperture by rays that are reflected from the interior of the radome wall.

Internal reflection contributes to radar pointing error and increased antenna sidelobe levels, because the internal reflected energy does not arrive at the aperture from the direction to the target.

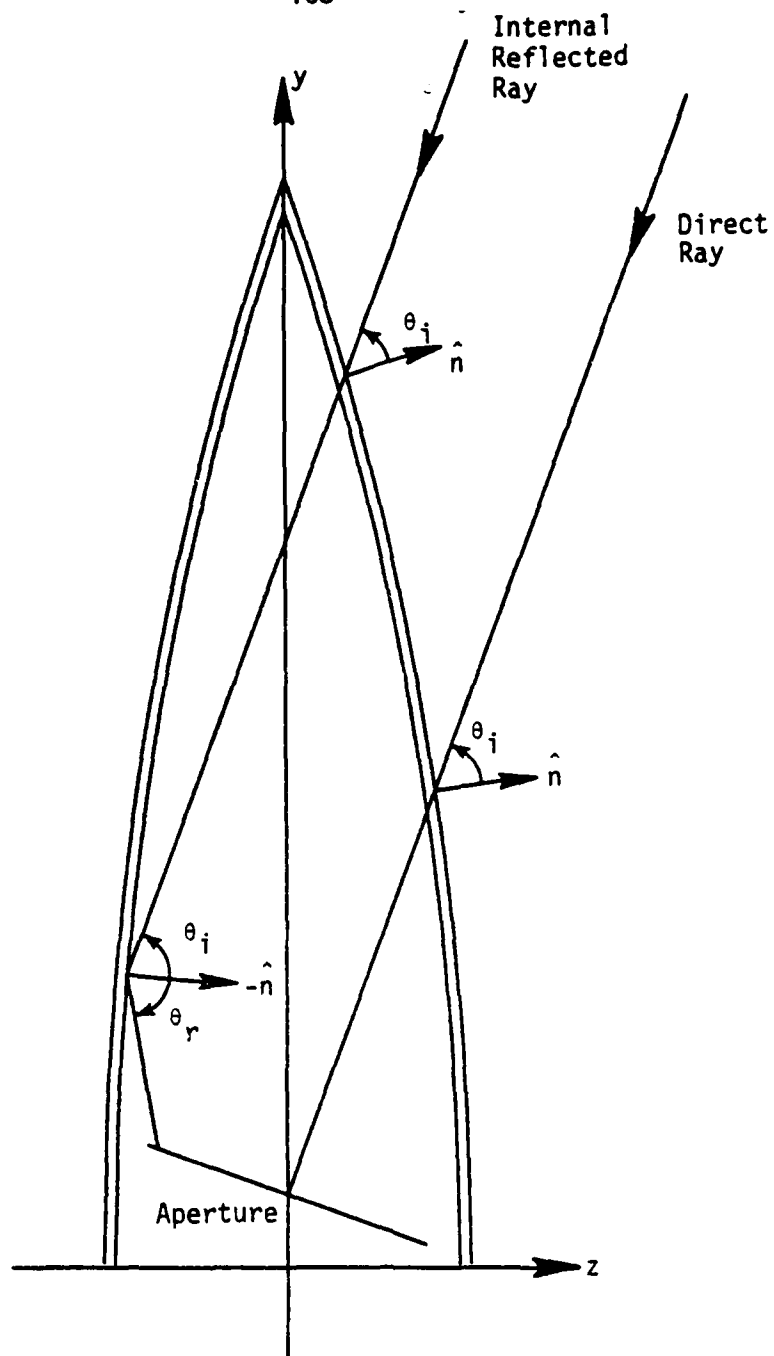


Figure 3-21. Outline of Tangent Ogive Radome Showing Internal Reflection.

The total field over the aperture is the superposition of the direct and reflected fields. For this reason internal reflection is sometimes referred to as the Lloyd's mirror effect due to its similarity with an optical experiment in which an interference pattern is obtained with a single light source by using the light direct from the source and light reflected from a planar mirror [40].

It has also been pointed out that the internal reflection phenomena is similar to holography [41]. Recall that holography involves recording the interference pattern of a reference beam and an object beam. In the radome case, the reference beam is the direct wave and the object beam is the internal reflected wave. The two waves interfere over the aperture which is analogous to the photographic plate used in optical holography. Use of this concept may provide a powerful tool for optimizing radome performance.

In this section, only the internal reflected field that is incident on the aperture will be obtained. The total field in the aperture and the radar response to internal reflection are considered in the following sections. The beginning point is to obtain the field that is incident on the inside wall. Note that internal reflection is impossible for on-axis incidence. Thus, internal reflection need not be considered until the incident field is far enough off axis to make ray reflection into the aperture possible.

In this study, it was decided to consider only the internal reflected rays that enter and are reflected at points on opposite halves of the radome. The reason for this can be seen by considering a ray that

enters and reflects from the same side of the wall (ray entry and reflection at points where $z < 0$ in Figure 3-21). Under this condition the ray incidence angle is extremely high at the entry point. Since the wall transmission coefficient is rapidly going to zero toward grazing incidence, little energy can enter the radome at these angles.

It must be mentioned, however, that these are precisely the conditions favorable for excitation of a surface wave on the radome. Consideration of surface waves are beyond the scope of this analysis, but some of their possible effects will be mentioned in the next section.

Under the conditions of opposite-wall transmission and reflection, the shadow of the radome tip in the $y = 0$ plane lies outside the radome. The angle at which this occurs is used in the computed calculations to signal the possibility of internal reflection. When internal reflection is possible, the intersection of the ray and radome must be found at two points: the transmission point and the reflection point.

The ray-radome intersection points are found by the numerical search procedure previously described. The transmission point is found from the root of the ray-radome difference equation with z coordinate between zero and the radome base radius. The reflection point is associated with the root to the left of zero, and inside the radome as shown in Figure 3-21. The radome generating parameters for the radome interior surface are used in finding the reflection point.

At the transmission point, the transmitted field is obtained from the incident field in exactly the same manner as for a direct ray. That is, the wall is modeled as a planar slab; the ray incidence angle is

found from the surface normal; the field is decomposed into parallel and perpendicular components; the transmission coefficients are found for the incident angle; and the transmitted field is given by the product of the incident field and the transmission coefficient. This transmitted field becomes the incident field at the reflection point.

At the reflection point, the radome wall is again modeled as a planar slab. The reflection coefficient and direction of the reflected ray are of interest at this point. The reflection coefficient is a function of incidence angle and polarization, thus these must be known. The incidence angle is determined in the same manner as for a transmitted ray; except now the inward unit vector normal to the radome wall is used.

The reflected field at the reflection point is obtained by decomposing the incident field into parallel and perpendicular components and then multiplying by the appropriate plane wave reflection coefficient. This reflected field then becomes the incident field at the aperture after propagation from the reflection point.

The reflected ray leaves the reflection point in the direction predicted by Snell's reflection law. Equation (2.109) gives an expression for a unit vector in the direction of the reflected ray when the vectors that apply to the present case are substituted.

Not all reflected rays will intersect the antenna aperture. Thus, it is important to know if a given ray will be incident on the aperture. Indeed, there is no point in performing the above calculations for rays that do not contribute to the radar response -- thus this condition is checked first. The method used is to ignore all rays that

reflect at points in back of the aperture and to ignore all rays that intersect the aperture plane at points outside the aperture perimeter.

The point at which a reflected ray intersects the aperture is important, because it determines the value of the aperture illumination function to be applied to that ray during aperture integration. The distance from the ray reflection point to the aperture intersection point is also important, because phase retardation occurs over this distance. The method used to find these two quantities is described next.

Suppose (x_r, y_r, z_r) are the rectangular coordinates of a ray reflection point and \hat{c} is a unit vector in the direction of the reflected ray as obtained from the incident ray direction and the radome surface normal by equation (2.109). The coordinates of a point (x, y, z) , on the ray trajectory are given by,

$$x = c_x s + x_r, \quad (3.10)$$

$$y = c_y s + y_r, \quad (3.11)$$

$$z = c_z s + z_r, \quad (3.12)$$

where s is the distance from (x_r, y_r, z_r) to (x, y, z) and c_x, c_y, c_z are the rectangular components of \hat{c} which are simply the direction cosines of the ray. The problem is to find s such that (x, y, z) lies in the antenna aperture plane.

The equation for the antenna aperture plane can be obtained in radome coordinates by inverting the matrix in (3.2) and solving for the points, $y' = 0$, since these points describe the aperture plane. The y coordinate of the aperture plane is

$$y = \frac{\tan \beta}{\cos \alpha} x - \tan \alpha z + y_g, \quad (3.13)$$

where α and β are the antenna rotation angles.

The distance, s , from the ray-reflection point to the ray-aperture plane intersection point is obtained by substituting (3.10), (3.11), and (3.12) into (3.13) and solving for s . This yields

$$s = \frac{x_r \frac{\tan \beta}{\cos \alpha} - y_r - z_r \tan \alpha + y_g}{-c_x \frac{\tan \beta}{\cos \alpha} + c_y + c_z \tan \alpha}. \quad (3.14)$$

The ray-aperture plane intersection point is obtained from (3.10), (3.11), and (3.12).

Before considering some examples, the procedure for finding the internally reflected field at the aperture is briefly summarized. The process begins by tracing the incident ray through the radome. The intersection points are found by a numerical technique. At the transmission point the incident ray is modified by the transmission coefficient. The transmitted ray becomes the incident ray at the reflection point on the opposite side of the radome. At the reflection point the ray is modified by the reflection coefficient and redirected according to Snell's reflection law. The ray then travels to the

antenna aperture. The phase of the internal reflected field at the aperture is determined by the transmission and reflection coefficients as well as the propagation distances involved.

A radome with constant wall thickness (designed for 100% transmission at 75° incidence) will again be used for an example. The transmission and reflection coefficients of this wall were presented in Figures 2-15 and 2-16. The radome is a tangent ogive with the same dimensions (length $30\lambda_0$, base diameter $10\lambda_0$) used before, and the antenna aperture has a radius of $4\lambda_0$. Incident fields with TE and TM polarization are considered.

In Figure 3-22 the magnitude of the internal reflected, TE polarized field over the antenna aperture is shown for the incident angle, $\theta = 70^\circ$. Recall that internal reflection does not occur for incidence angles near axial. Seventy degrees (or 20° off axis) represents the beginning of favorable conditions for internal reflection.

The magnitude of the incident field outside the radome is unity in Figure 3-22 and all similar figures to follow. Thus, the height of the reflected field surface provides a comparison of the relative magnitudes of the direct and reflected fields.

It should be noted in Figure 3-22 that the reflected field is confined to the left-rear edge of the aperture. The reason for this is apparent in Figure 3-21 where it is seen that favorable conditions for ray reflection exist only for rays to the left edge of the aperture at high incidence angles. As the incidence angle decreases, the reflected field spreads over the aperture.

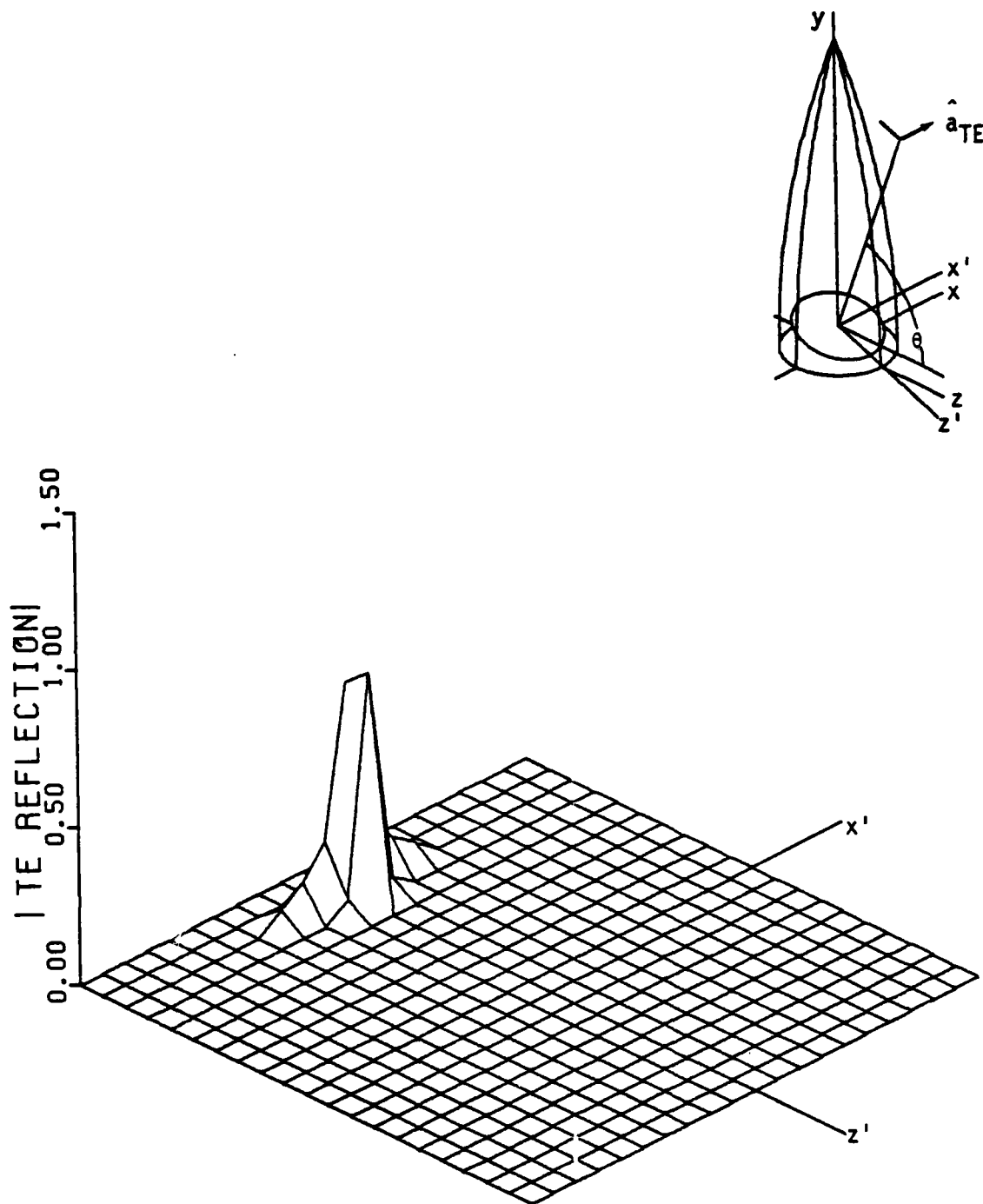


Figure 3-22. Magnitude of Internal Reflected, TE Polarized Field with 70° Incidence Angle.

Figures 3-23 through 3-25 show the reflected field for incidence angles beginning at 60° and decreasing in 10° increments. At 50° incidence, the reflected field covers the entire aperture. At incidence angles less than 40° internal reflection is no longer possible because the reflected rays either pass over the aperture or intersect the aperture from the rear. However, multiple internal reflection becomes a possibility at these low incidence angles.

Figures 3-22 through 3-25 were made by considering a set of rays spaced $\lambda_0/2$ in a square grid perpendicular to the direction of propagation. Each ray was traced through the radome, reflected, and checked for intersection with the rotated aperture. If a ray intersected the aperture, the complex value of its vector components were associated with the aperture grid point nearest the intersection point. Whenever two or more rays intersected the aperture in the same grid cell, they were coherently summed to produce the total field in that cell. Of course, a given grid cell in the aperture might have several or no rays intersecting it. The peaked appearance of some of these figures is a result of the ray spacing. Use of a finer grid would tend to fill the region between peaks.

The above approach is like considering the rays as centers of ray tubes which direct the flow of energy. If two or more ray tubes intersect at the aperture, the total field is the coherent sum of the fields

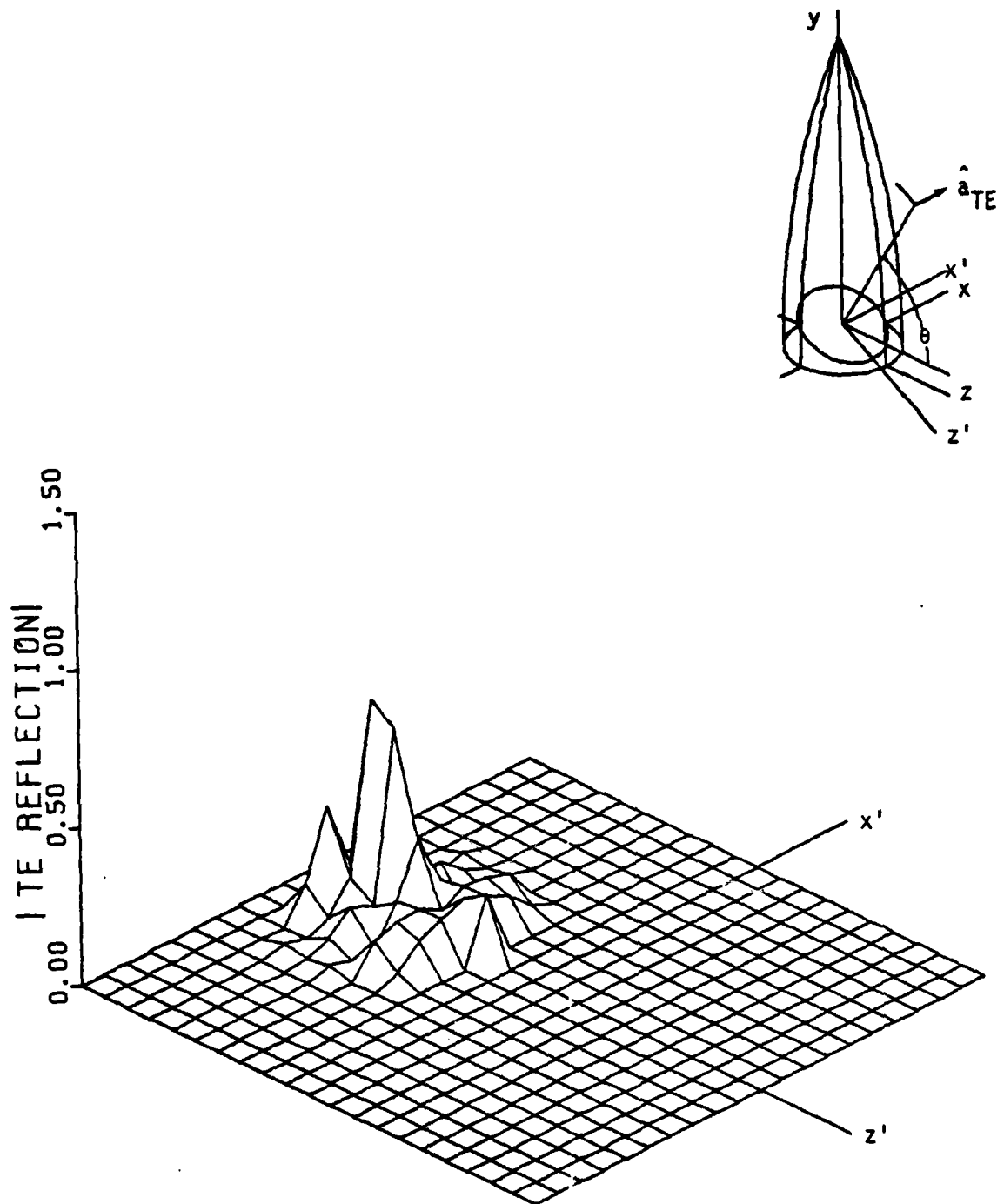


Figure 3-23. Magnitude of Internal Reflected, TE Polarized Field with 60° Incidence Angle.

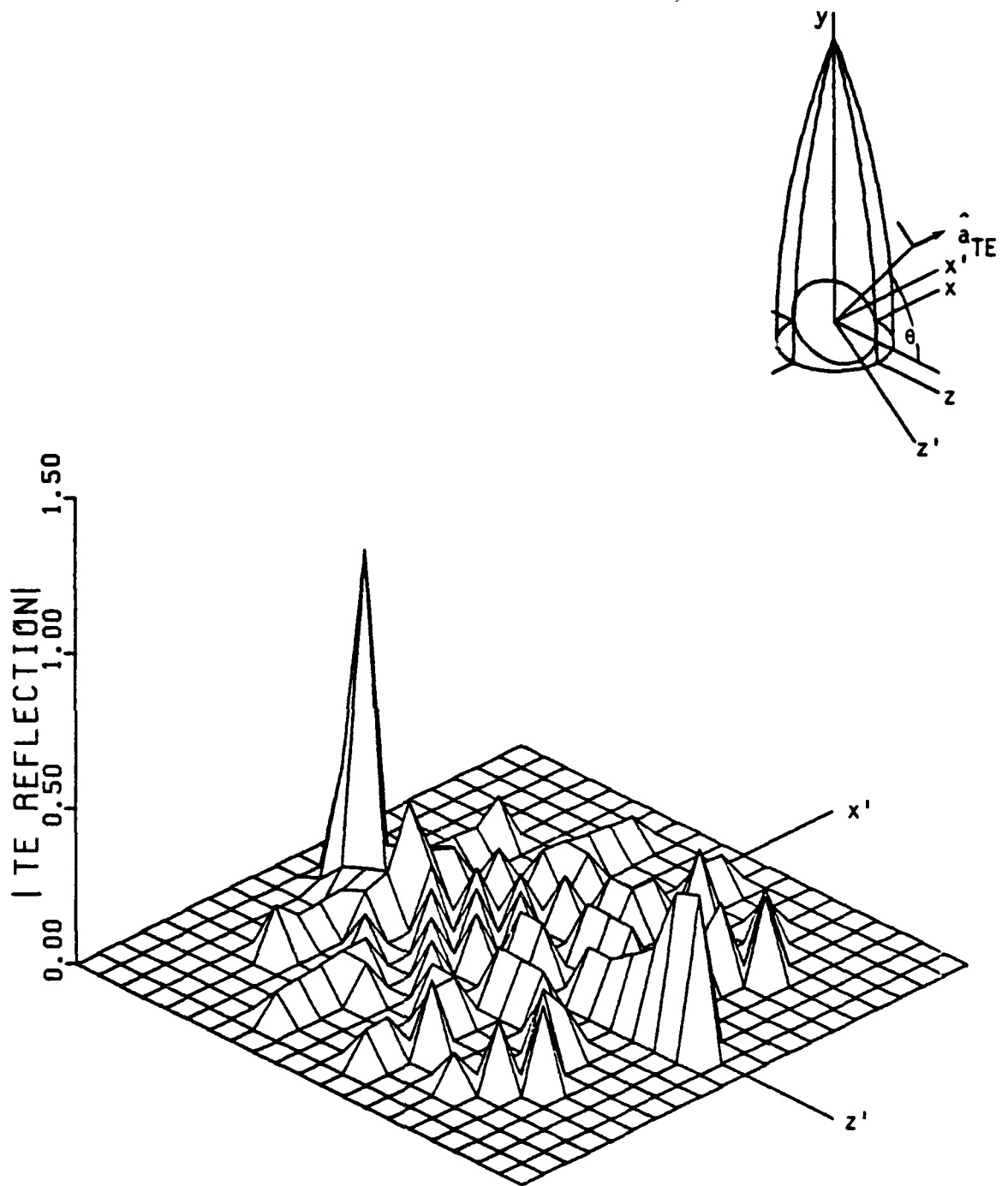


Figure 3-24. Magnitude of Internal Reflected, TE Polarized Field with 50° Incidence Angle.

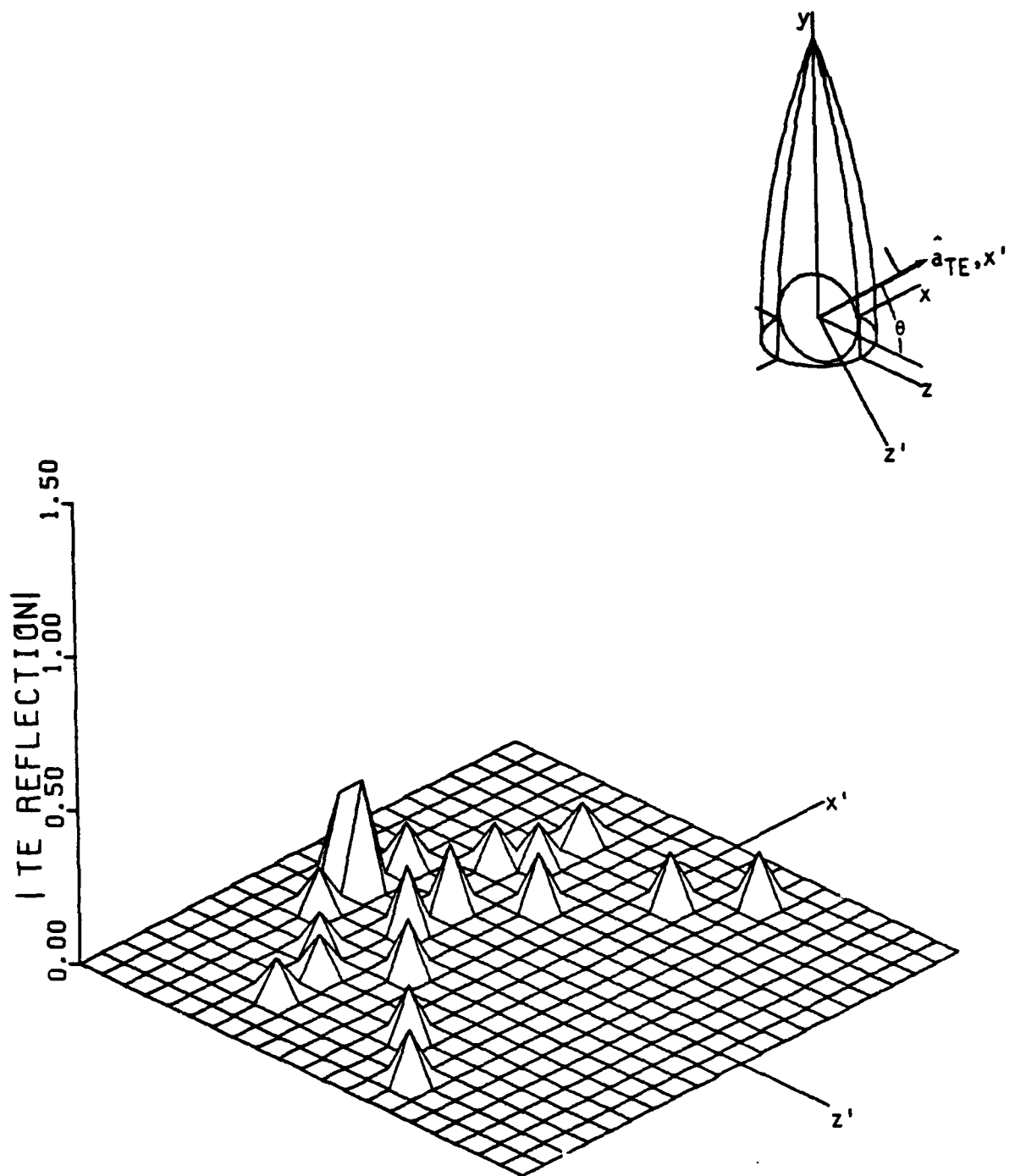


Figure 3-25. Magnitude of Internal Reflected, TE Polarized Field with 40° Incidence Angle.

in each ray tube. The total field magnitude may take on any value from zero to the sum of the individual ray magnitudes, depending on the amplitude, phase, and direction of the individual fields.

The left-rear edge of the aperture is seen to have a high reflected field magnitude for all angles of incidence. This is due to a focusing effect of the radome. The concave shape of the radome surface reflects rays to this region and the path lengths are such that the fields there interfere constructively.

Reflected fields for TM polarization are considered next. Figures 3-26 through 3-29 contain these data presented in the same manner as the TE case. By comparing these figures with the corresponding figures for the TE case, it is seen that the spatial distributions of these reflected fields are the same (since this is determined by geometry alone), but the magnitudes are considerable less.

The difference in the TE and TM reflected field magnitudes can be explained by the wall reflection coefficients and the polarization of the field at the reflection surface. At the points favorable for ray reflection, a TE polarized field is mostly perpendicularly polarized with respect to the wall; while a TM polarized field is mostly parallelly polarized. Upon referring to the wall reflection coefficients (Figure 2-6), one sees that the magnitude of the reflection coefficient for perpendicular polarization is larger than that for parallel polarization at the high incidence angles. This points out the need for a

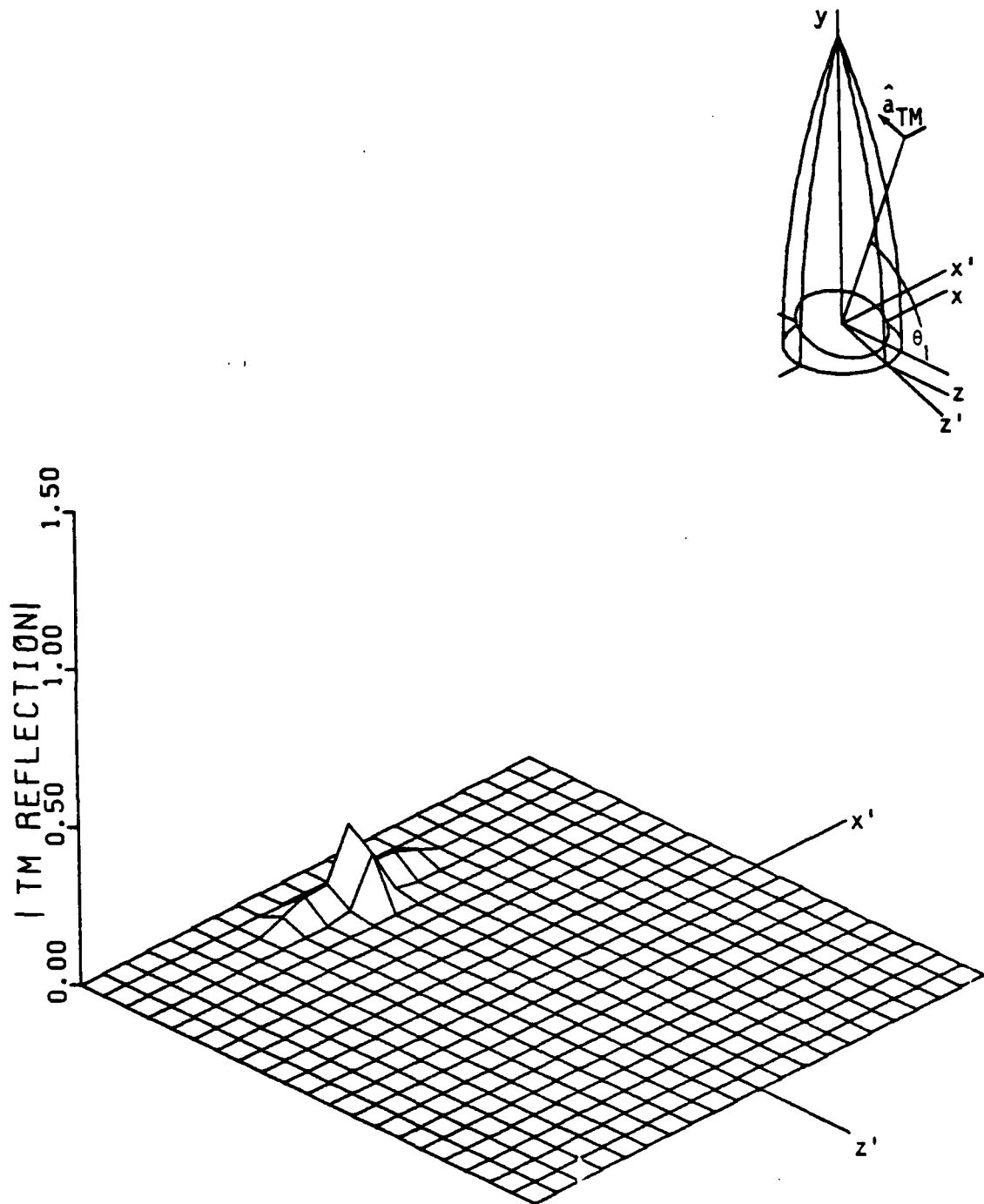


Figure 3-26. Magnitude of Internal Reflected, TM Polarized Field with 70° Incidence Angle.

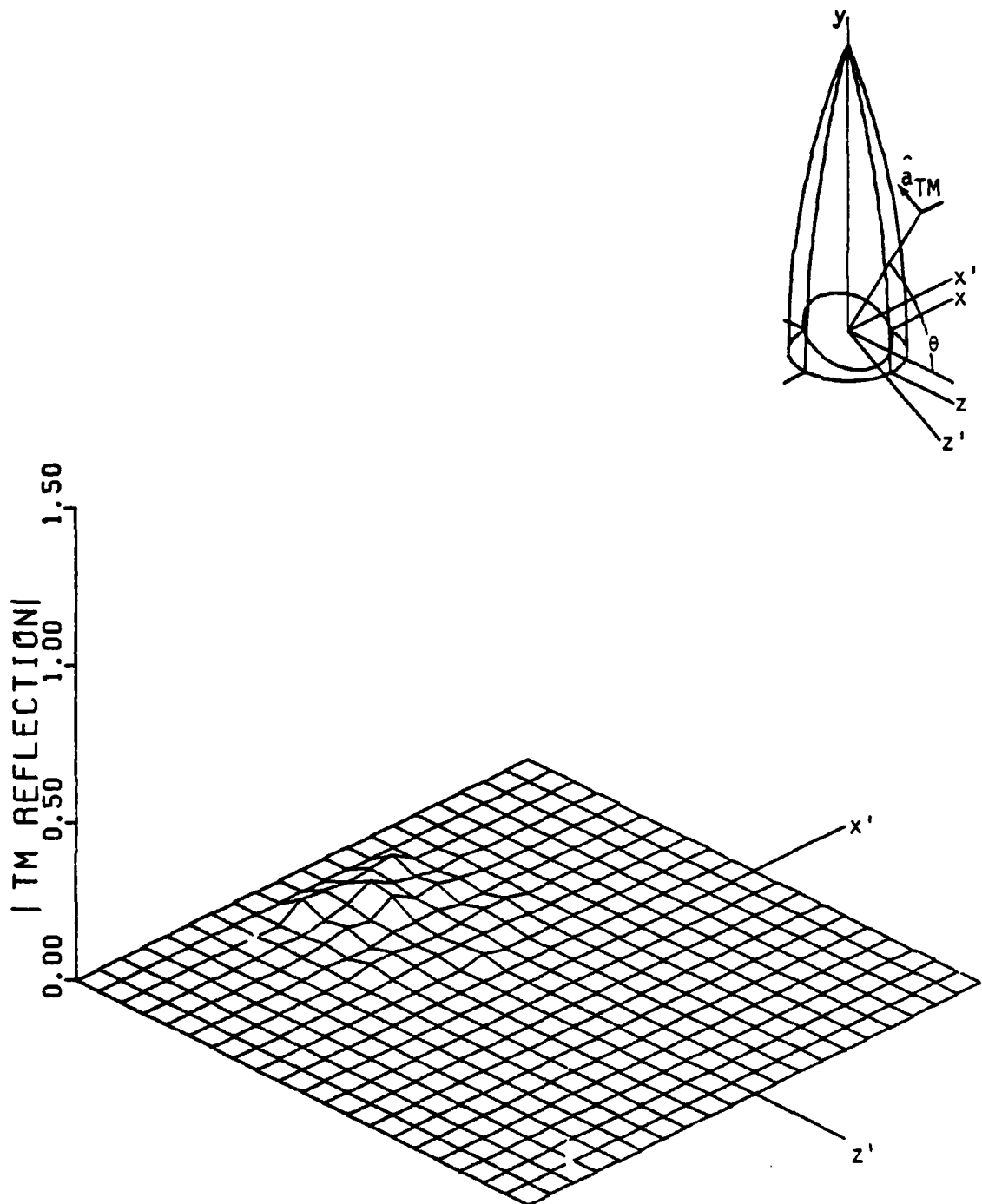


Figure 3-27. Magnitude of Internal Reflected, TM Polarized Field with 60° Incidence Angle.

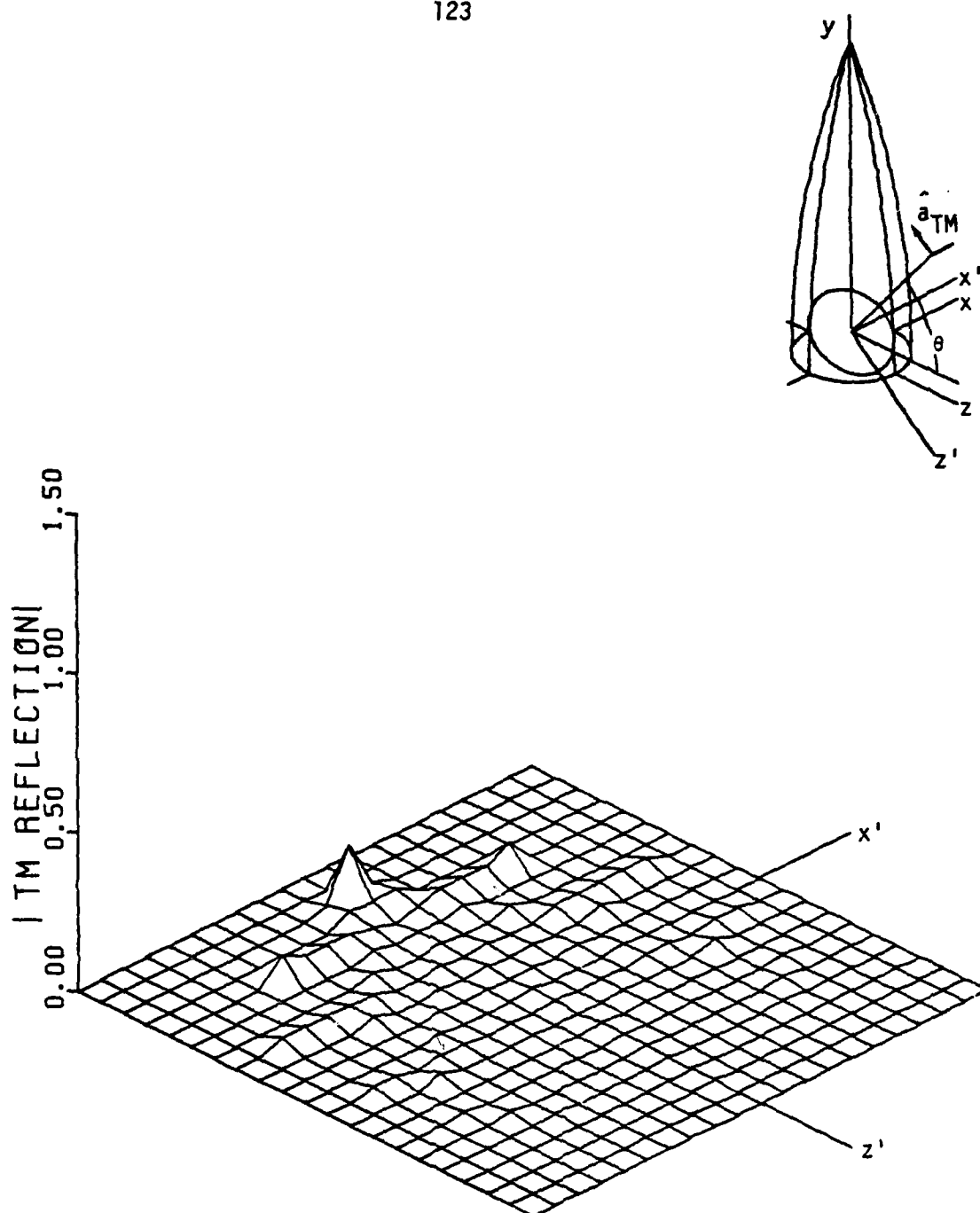


Figure 3-28. Magnitude of Internal Reflected, TM Polarized Field with 50° Incidence Angle.

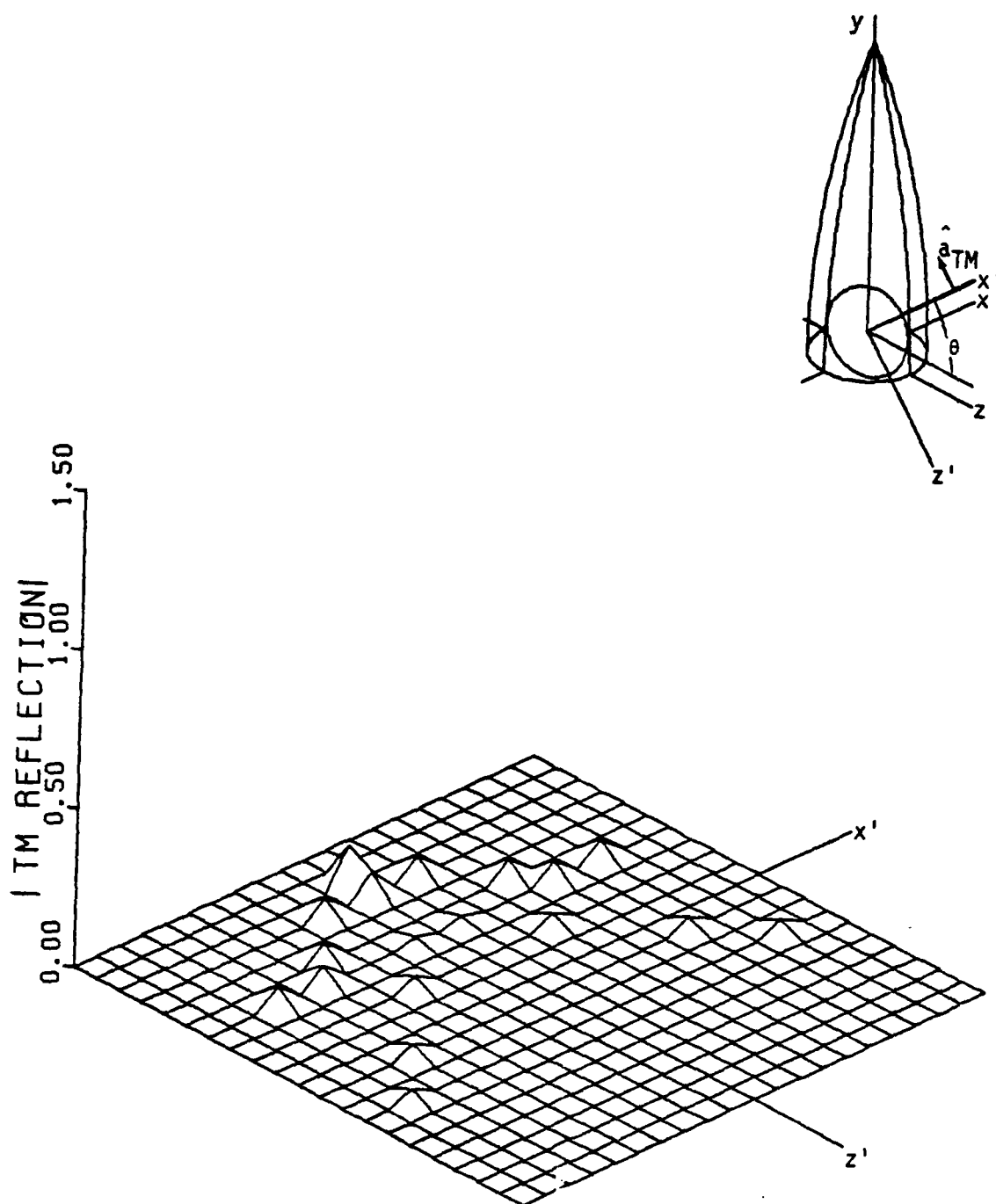


Figure 3-29. Magnitude of Internal Reflected, TM Polarized Field with 40° Incidence Angle.

wall with a high transmission coefficient (low reflection coefficient) at the ray reflection points as well as the transmission points.

This last point is further emphasized by considering the internal reflection properties of the polyimide quartz radome introduced in the last section. Recall that this wall was designed for 100% transmission at 60° incidence, but the design goal is not achieved due to loss. The reflection coefficients for this wall are given in Figure 3-30.

The magnitude of the internal reflected field over the aperture will be presented as in the last example with no changes other than the wall construction. Figure 3-31 shows the magnitude of the reflected field for TE polarization and 70° incidence. Note that a different scale is used for the magnitude and the peak is nearly ten times larger than the peak in Figure 3-22. Recall that the incident field outside the radome has magnitude of only one. The increased reflection coefficient of the wall together with the focusing effect have produced a field with magnitude of about six at the aperture edge.

The internal reflected field at 60° incidence is shown in Figure 3-32 again for TE Polarization. This figure also shows higher field magnitudes than the corresponding 75° wall case (Figure 3-23).

The 50° incidence angle case is shown in Figure 3-33. Comparison with Figure 3-24 shows that the internal reflections are less than for the case of Figure 3-24. This is because the incidence angle has now decreased to values where the wall reflection coefficient is small.

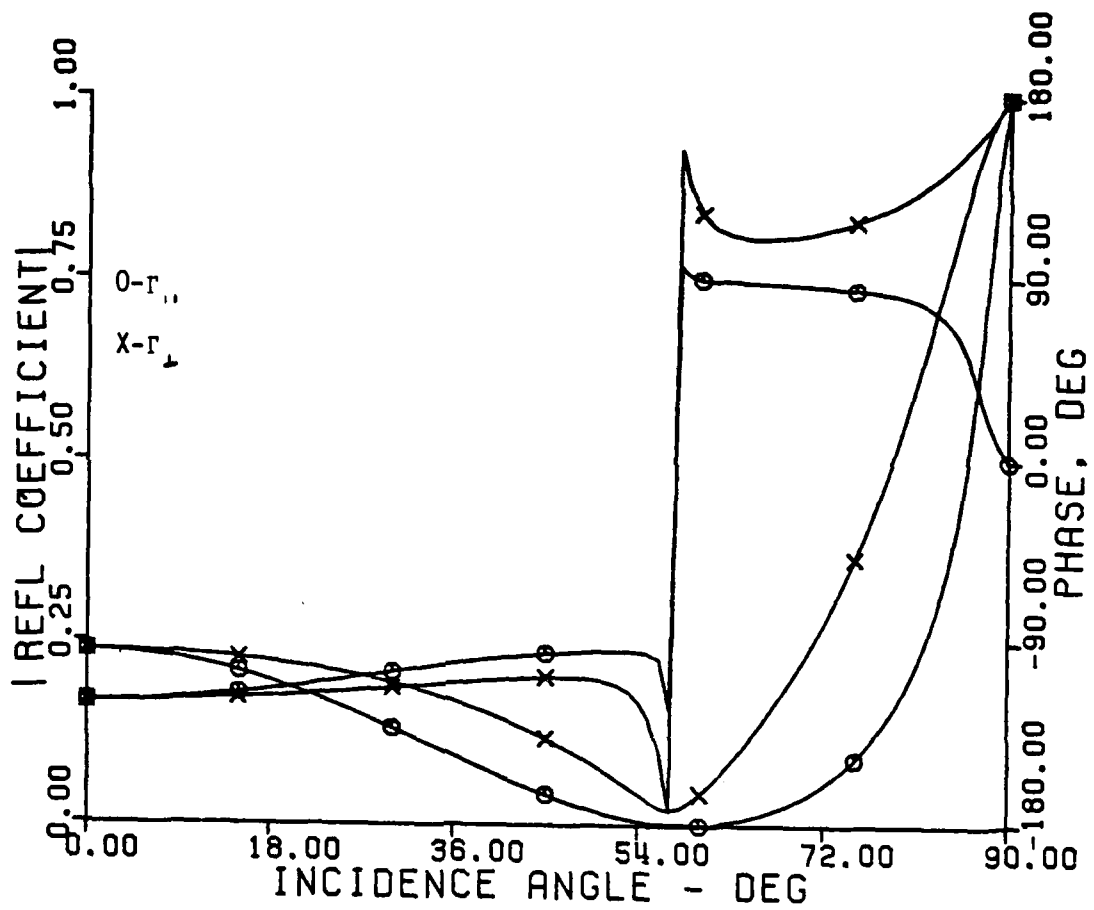


Figure 3- 30. Reflection Coefficients of Polyimide Quartz Wall Designed for 60°.

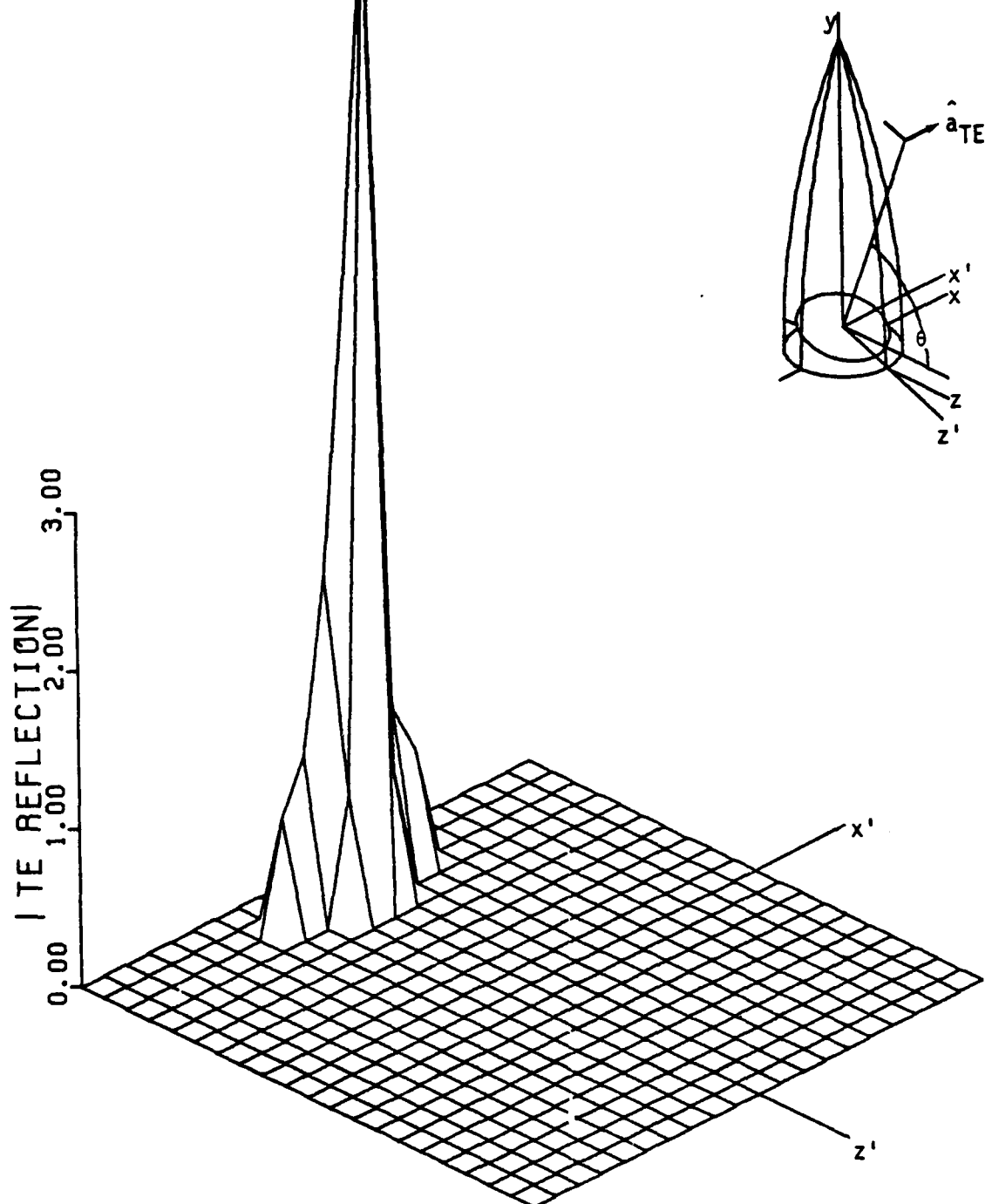


Figure 3-31. Magnitude of Internal Reflected, TE Polarized Field Incident at 70° on Polyimide Quartz Radome.

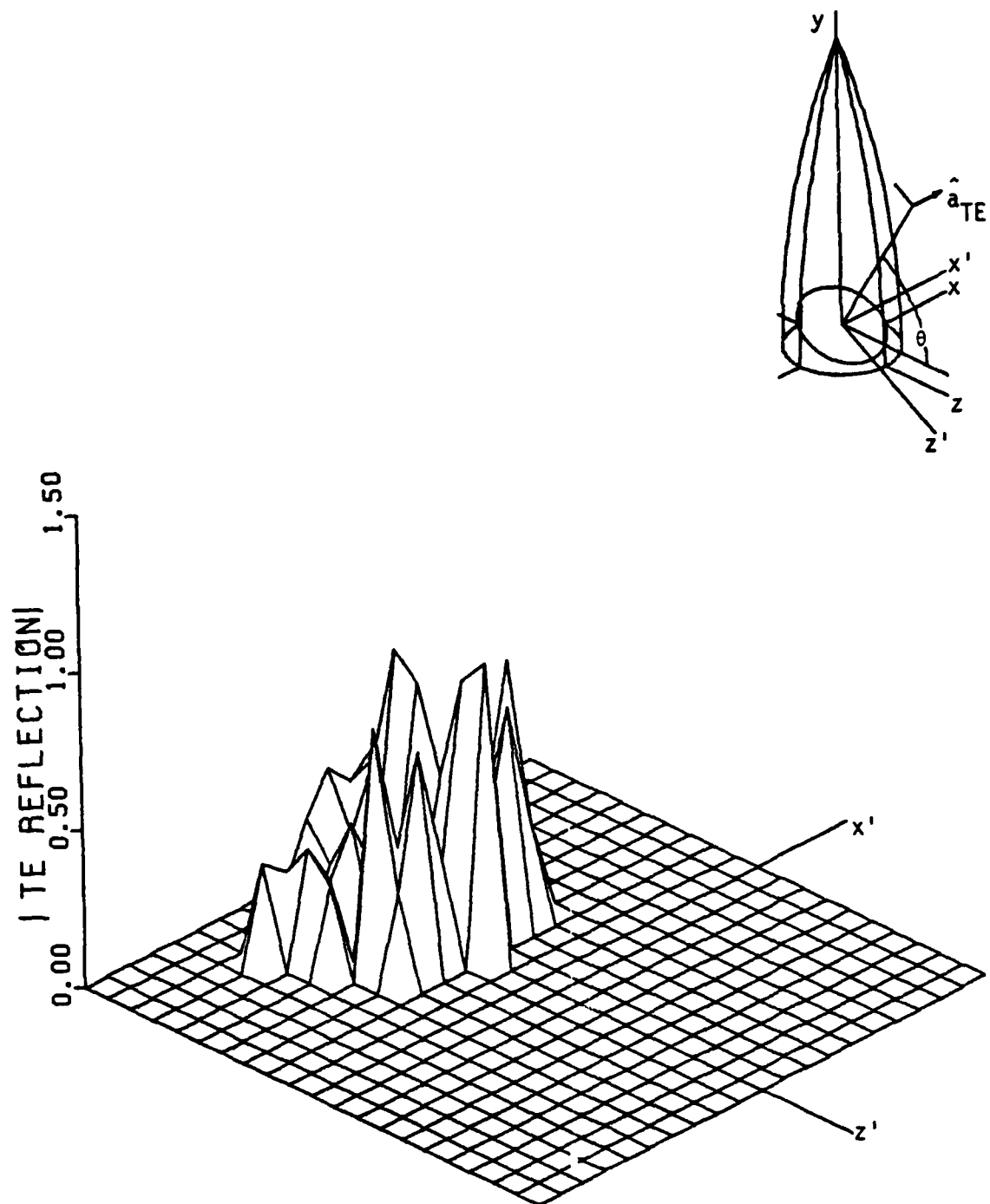


Figure 3-32. Magnitude of Internal Reflected, TE Polarized Field Incident at 60° on Polyimide Quartz Radome.

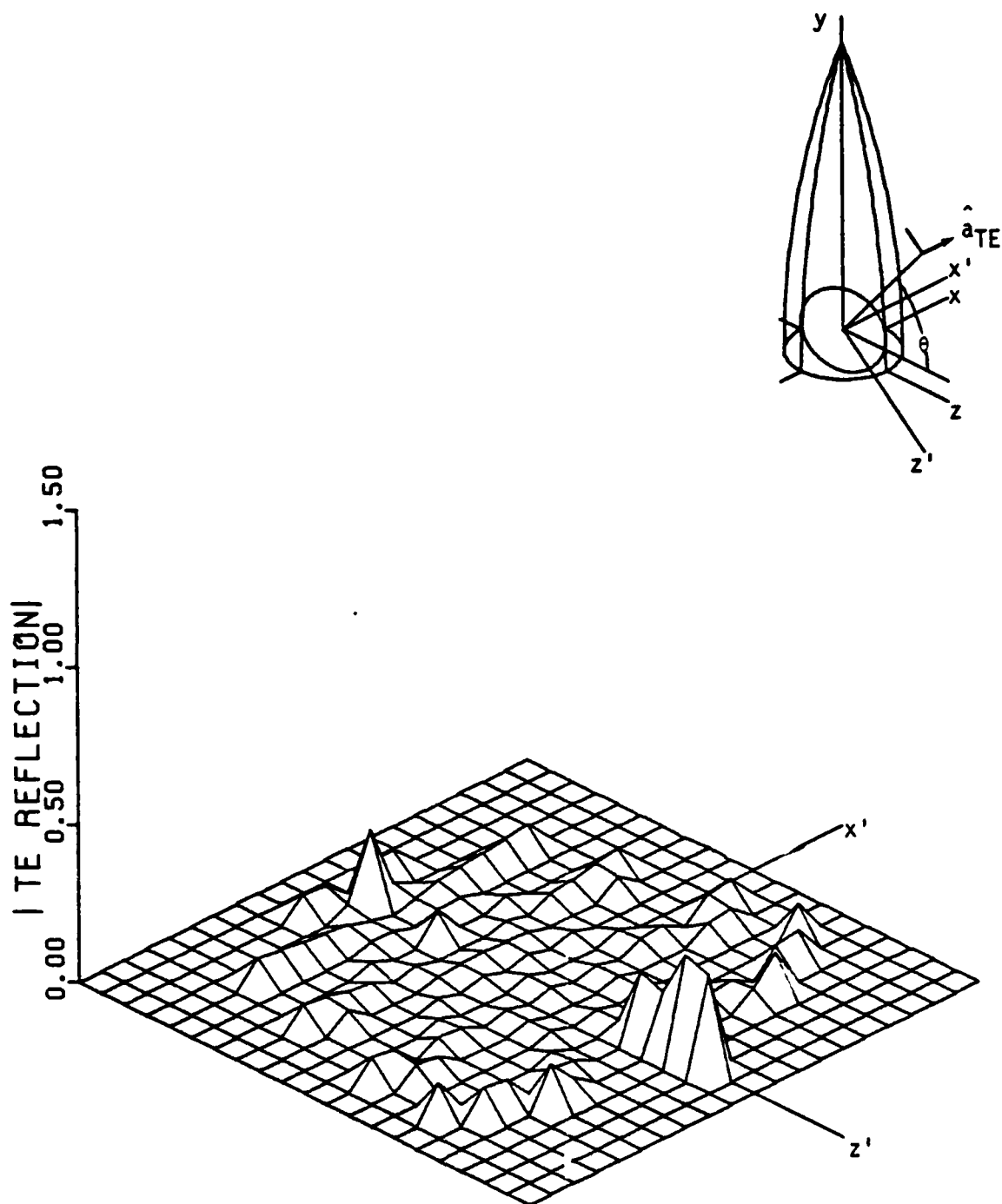


Figure 3-33. Magnitude of Internal Reflected, TE Polarized Field Incident at 50° on Polyimide Quartz Radome.

These last few figures indicate the reason why radome wall thickness is frequently tapered in practice. By varying the wall thickness, the radome can be made highly transparent in the region that fields enter and highly transparent in the areas that would contribute unwanted reflections.

The effect of internal reflection on radar pointing error will be presented after the next section which concerns the composite effects of radome-induced wavefront distortion.

COMPOSITE WAVEFRONT DISTORTION

The previous two sections have considered two factors that produce radome-induced wavefront distortion: transmission and internal reflection. The operating radome-radar system will have pointing errors due to these two sources and several others all acting together to produce a composite effect.

Primary emphasis in this study is placed on transmission and internal reflection; however, other factors may produce greater pointing error in some systems or at certain angles in any system. In this section some of the composite effects of transmission and internal reflection are discussed. Also, some of the possible sources of radome-induced pointing error that have been neglected in this study will be mentioned.

A radome produces amplitude and phase distortion in the wave transmitted directly through the radome to the antenna aperture.

Furthermore, for scan angles sufficiently far off axis (greater than about 14° for the tangent ogive with fineness ratio of three), the aperture is also illuminated by internal reflected fields that do not arrive from the general direction to the radar target. Both of these sources of aperture illumination contribute to the radar response.

The principle of superposition is used to determine the total incident field over the aperture. Thus the total field over the aperture is the coherent, vector sum of the direct and reflected fields. As such, the relative phase and direction of the fields are important along with the field amplitudes.

At low scan angles, the internal reflected energy is incident only at the edge of the aperture near the reflecting surface. This energy arrives in phase from the various reflecting points, so a large reflected-field amplitude is observed at the aperture.

At large scan angles, the internal reflected field spreads over the entire aperture. There is rapid phase variation of the reflected field over the aperture in this case because the arrival direction is far off the antenna axis. Later it will be seen that the radar has little response to these fields, since their sum over the aperture is small.

In addition to the internal reflected field, other factors contribute to the total field incident at an aperture in a real radome. One such factor is tip scattering. Even if the radome wall is homogeneous, the vertex of an ogive is a source of scattered energy. This phenomena,

which is much like edge diffraction, is due to the discontinuity in surface derivative at the vertex. Frequently a missile radome will contain a metal or ceramic insert in the tip to reduce rain erosion and improve strength. Such a tip insert can further enhance tip scatter because of the material discontinuity at the tip. Also some missile radomes contain a Pitot tube at the tip which is another source of unwanted scatter. The effects of any of these factors are difficult to estimate. Empirical investigation is likely to provide the greatest rewards in this area. Indeed, even the canonical problem of scatter from the vertex of a hollow dielectric cone has not been solved completely.

Another way energy may arrive at the antenna aperture is via a surface wave. A surface wave is a field that is bound to, and propagates along, a material's surface. Such fields attenuate exponentially away from the surface. Surface waves may be excited on a body by a wave that is incident near grazing, such as is often the case for a radome. Since the surface wave attenuates with distance away from the surface, it is likely that any effect on the radar system would be due to interaction with the edge of the antenna near the radome wall.

Additional scatterers inside the radome can contribute unwanted fields to the receiver. Such scatterers could include the antenna feed horn and supporting structure, tubing to Pitot tube, heating wires for a radome de-icer, metal behind the antenna, etc. Any of these items may contribute to distortion of the received wave.

Multiple scattering between the radome internal wall, or the wall and one of the above items, or between any two items mentioned above, or between the antenna and any other item, or any combination of these, may affect the received wave at the aperture.

In order to determine the radar response to all of the above factors, and others not mentioned, it would be necessary to solve a set of integral equations for the fields everywhere in and around the radome, taking into account all of the matter present and enforcing boundary conditions everywhere. Such equations are not likely to be formulated in the near future and can not be solved for practical size radomes because of the limitations of even the largest and fastest computers. For this reason, high-frequency approximations have proved most useful in radome analysis. They provide considerable insight into the physical phenomena involved, and they will likely continue to be used and improved.

Just as the case with antenna analysis and design, engineering practice and simplifying approximations must be used in radome analysis and design with systematic improvement being based on experiment. Transmission aberrations and internal reflection are considered to be the greatest source of radome-induced radar pointing error, but it must always be remembered that the radar response is the composite effect of many factors.

RADAR RESPONSE TO WAVEFRONT DISTORTION

The effect of a tangent ogive radome on the performance of a monopulse radar is considered in this section. Primary emphasis is given to the most undesirable effect of the radome--radar pointing error. Wavefront distortion produced by the radome has been discussed, therefore this section begins by considering how monopulse signals are obtained from the incident field at the antenna. Throughout this section, reference is made to the aperture phase and amplitude plots of earlier sections in order to relate the phenomena of wavefront distortion to radar pointing error. The effects of various wall thicknesses, aperture illumination functions, and polarizations are also compared.

In Chapter II the receiving properties of an aperture antenna were discussed. It was assumed that a uniform plane wave was incident on the aperture. The received signals were determined from the incident field and equivalent currents representing the antenna by means of the reciprocity theorem. The same procedure will now be used to find the received signals when the antenna is enclosed by a radome.

As explained in Chapter II, the voltage at the terminals of an aperture antenna, operating in the receive mode, is

$$V = (1 + \cos \theta)C \int_A \vec{E}^i \cdot \vec{J}_s \, ds, \quad (3.15)$$

where a uniform plane wave with electric field intensity, \vec{E}^i , is incident at the aperture; θ is the angle between the normal to the antenna aperture and the direction to the source of the incident field; \vec{J}_s is

the equivalent electric current for the antenna operating in the transmitting mode; C is a complex constant; the integration is over the antenna aperture; and V is either the sum or difference voltage, depending on whether the equivalent currents used are for the sum or difference pattern.

When radome-induced wavefront distortion is present, the incident field at the aperture is not planar and the angle, θ , in (3.15) becomes meaningless. However, since the distorted wavefront is well behaved over the aperture, a local angle of incidence can be found. The incident angle can then be brought inside the integration and considered as a variable, yielding

$$V = C \int_A (1 + \cos \theta) \bar{E}^i \cdot \bar{J}_s \, ds. \quad (3.16)$$

In order to obtain numerical results, this integral is approximated by a finite sum over the aperture with \bar{E}^i determined by the previously discussed ray tracing procedures. A rectangular grid of sample points is used in the aperture to find the voltage produced by the direct wave. This yields

$$V = C \sum_{m=-N}^N \sum_{n=-N}^N (1 + \cos \theta_{mn}) \bar{E}^i \cdot \bar{J}_s(m\Delta x', n\Delta x') \Delta s, \quad (3.17)$$

with $m^2 + n^2 \leq N^2$

where θ_{mn} is the incident angle at the mn -th sample, the functional dependence of $\bar{E}^i \cdot \bar{J}$ is indicated, Δs is $\Delta x' \Delta x'$, and N is given by

$$N = [D/(2\Delta x')] , \quad (3.18)$$

with D the aperture diameter, $\Delta x'$ the sample point spacing, and the brackets take the largest integer less than or equal to the quantity inside.

The contribution of internal reflected energy to the sum and difference signals is determined from the reflected rays that intersect the antenna aperture. As previously described, a set of regularly spaced rays are traced through the radome, reflected, and traced to the aperture plane. Those rays actually entering the aperture contribute to the sum and difference signals according to

$$V = C \sum \sum (1 + \cos \theta_{mn}) \bar{E}^i \cdot \bar{J}_s(x', z') \Delta s, \quad (3.19)$$

$$\text{with } (x')^2 + (z')^2 \leq D/2$$

where x' and z' are the aperture coordinates of the ray-aperture intersection point, θ_{mn} is the angle between the antenna normal and a reflected ray, and the summation extends over all possible singly reflected rays.

The surface current density, \bar{J}_s , above serves the dual role of sampling the tangential component of the incident field (through the dot product) and weighting the summation. The name, aperture illumination function, was given to the magnitude of \bar{J}_s , and two examples were presented in Chapter II: uniform and cosine taper. Radar pointing error for these two aperture illumination functions will be compared in the examples that follow.

Throughout this section the receiving antenna is assumed to be circular polarized. This is done so that the antenna will be sensitive to incident fields with any linear polarization. Actual missile radar systems may transmit and receive either linear or circular polarization, but the field scattered by the target will, in general, have time-varying polarization due to the complex geometry of the target. The assumption of a circular-polarized receiving antenna is made in order to compare the effects of various incident field polarizations.

A circular-polarized receiving antenna can be represented by an equivalent surface current density that rotates at an angular velocity, ω (the radian frequency of the fields), in the aperture plane. Jordan and Balmain [42] describe how a rotating unit vector in the direction of this current can be constructed. The rotating unit vector is composed of two orthogonal vectors having quadrature time dependence with left or right sense determined by their phase relationship (which vector leads).

For the aperture antenna under discussion here, two suitable orthogonal vectors in the aperture plane are \hat{x}' and \hat{z}' (see Figure 3-3). These vectors are combined to produce the rotating unit vector in the right-hand direction, \hat{a}_r , as given by

$$\hat{a}_r = \frac{1}{\sqrt{2}} (\hat{x}' - j\hat{z}'), \quad (3.20)$$

where propagation in the $-\hat{y}'$ direction (receiving) has been assumed. The square root of two factor is necessary to normalize \hat{a}_r , that is

make $\hat{a}_r \cdot \hat{a}_r = 1$. Recall that one vector is conjugated when taking dot products of complex vectors. (The "unit" vectors given by Jordan and Balmain have not been normalized.)

The left-hand unit vector is simply the conjugate of (3.20). It is not difficult to show that left and right circular polarizations are orthogonal. Left-circular polarization will not be considered here.

The equivalent surface current density, \bar{J}_s , for the aperture antenna can now be written as

$$\bar{J}_s = g(r, \phi) \hat{a}_r, \quad (3.21)$$

where g is the (scalar) aperture illumination function, either uniform or cosine taper here.

A computer program was written to perform the numerical aperture integration described in this section. The fields at the antenna are calculated by ray tracing. The radome wall transmission and reflection coefficients are calculated and stored at 3° intervals before any aperture integrations are performed. Whenever a transmission or reflection coefficient is required, the three closest stored values are interpolated with a second-order polynomial to provide the desired coefficient. This interpolation scheme was found to provide better than five decimal-place accuracy, which is well within the accuracy of other approximations used.

The complete program used for radome error calculation is listed in the Appendix.

This program has two options after monopulse signals have been computed. The first is to reposition the antenna to the angles indicated by the computed monopulse signals. Indicated errors are then recomputed and the antenna repositioned according to the new indicated angles. This procedure is repeated until the antenna is repositioned less than a user-specified amount. Radar pointing error is then the difference between the pointing angle of the antenna and the angle of the incident field.

The second option is to define radar pointing error as the angle indicated by the monopulse signal when the antenna has no pointing error. This option was included in the program when it was discovered that after the initial repositioning of the antenna according to the first option, the next indicated errors were consistently zero within numerical accuracy. Thus, both options provide the same results, but the second requires only about half the computer run time. The pointing errors presented throughout this work are the indicated errors according to the second option.

Some examples of radar pointing error are now considered. For each of these examples, the radome is considered to be a tangent ogive with constant wall thickness and fineness ratio of three. The radome base diameter is $10\lambda_0$ and the antenna aperture diameter is $8\lambda_0$. The antenna gimbal point is $2\lambda_0$ above the radome base plane ($y_g = 2\lambda_0$ in Figure 3-3). All these conditions are the same as for previously presented examples.

The antenna aperture can be rotated in two orthogonal angular directions: the α and β scan angles of Figure 3-17. Radar pointing error for a given scan direction is defined as the scan angle of the antenna minus the scan angle of the incident wave. Pointing errors in the α scan-angle direction are called in-plane pointing errors since they are in the plane formed by the incident field direction and the radome axis. Pointing errors in the β scan-angle direction are called cross-plane pointing errors.

A radome with the wall design for 100% transmission at 75° is considered first. The transmission and reflection coefficients for this wall were given in Figures 2-15 and 2-16. The incident field is polarized in the principal polarization directions, TE and TM, but the right-hand circular component of these fields is detected at the aperture.

The in-plane pointing error for this case is shown in Figure 3-34. The aperture illumination function is uniform. Pointing error is shown as a function of the α scan angle and the effect of including internal reflection is illustrated. Note that internal reflection has no effect on pointing error for scan angles up to about 14° since internal reflection is not possible for these angles.

In the TM case, the internal reflected fields cause almost no change in pointing error. But in the TE case, internal reflection causes a oscillation in the pointing error about the no-reflection value. As was seen in Figures 3-22 through 3-29, TE polarization

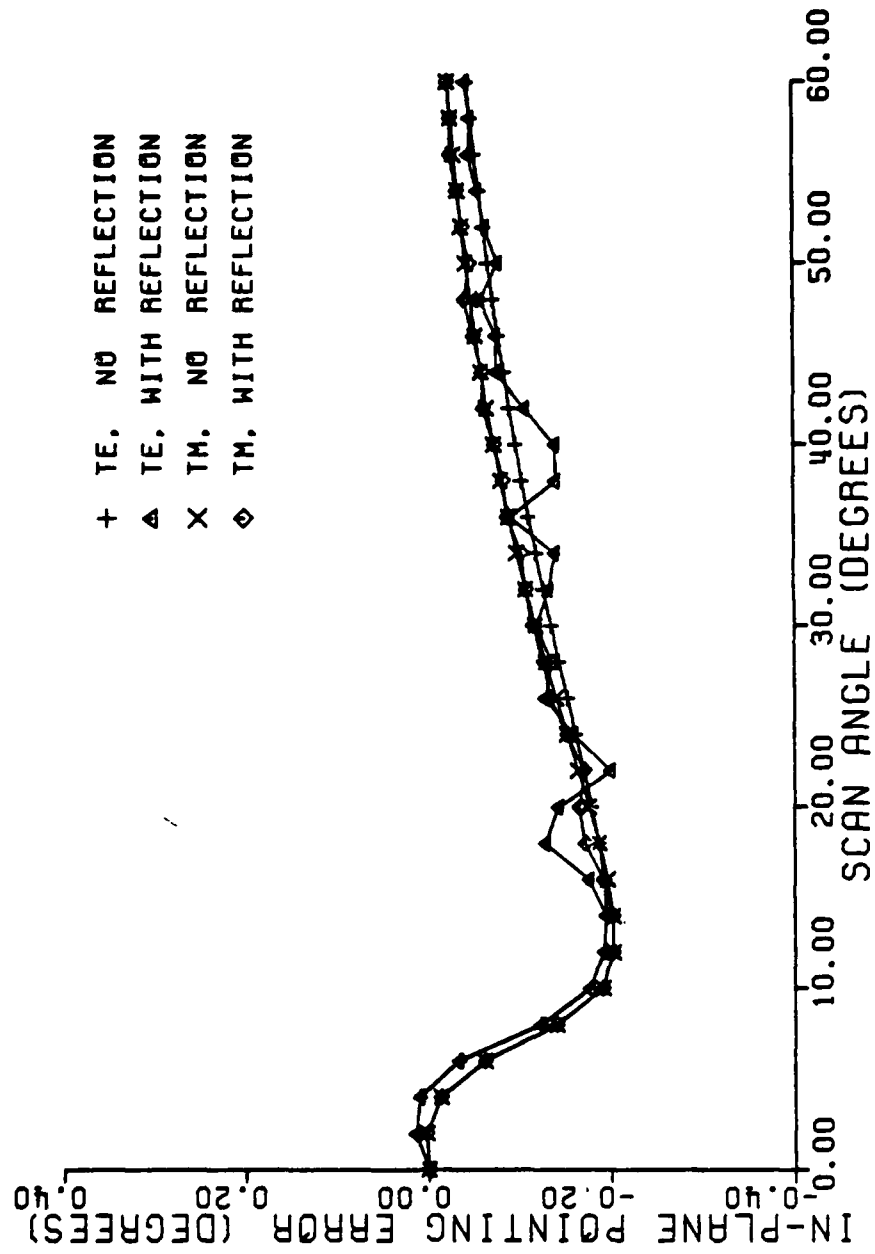


Figure 3-34. In-Plane Radar Pointing Error for Radome with 75° Wall Design and Uniform Aperture Illumination Showing Effect of Internal Reflection.

produces much larger reflections to the aperture than TM polarization. The perturbation of the TE pointing error is thus related to the interference between this larger reflection and the direct wave.

It is also noted in Figure 3-34 that the pointing errors are negative for all scan angles (except TE at 0° to 6°). This is due to the slope of the phase front of the incident field at the aperture. As was shown in Figure 3-5 through 3-8 and 3-10 through 3-13, the average slope of the phase front over the aperture is positive in the z' direction when the aperture has zero pointing error. This means that the aperture must scan in the negative α direction in order to become aligned with the average phase slope, so the radar pointing error is negative.

Next, consideration is given to the effects of substituting a different wall design in the above example. The wall design for 60° incidence previously presented will be used. The transmission and reflection coefficients for this wall were given in Figures 3-14 and 3-30. In-plane radar pointing error for this wall design, but with all other parameters the same as for Figure 3-34, are presented in Figure 3-35.

Note the differences. Beginning with zero pointing error on axis, the TE error curve increases while the TM error curve decreases. Maximum error is larger and occurs at a lower scan angle than for the 75° wall design. It was shown in Figures 3-15 and 3-16 that for the 60° wall design and 10° scan angle, the average phase slope across the

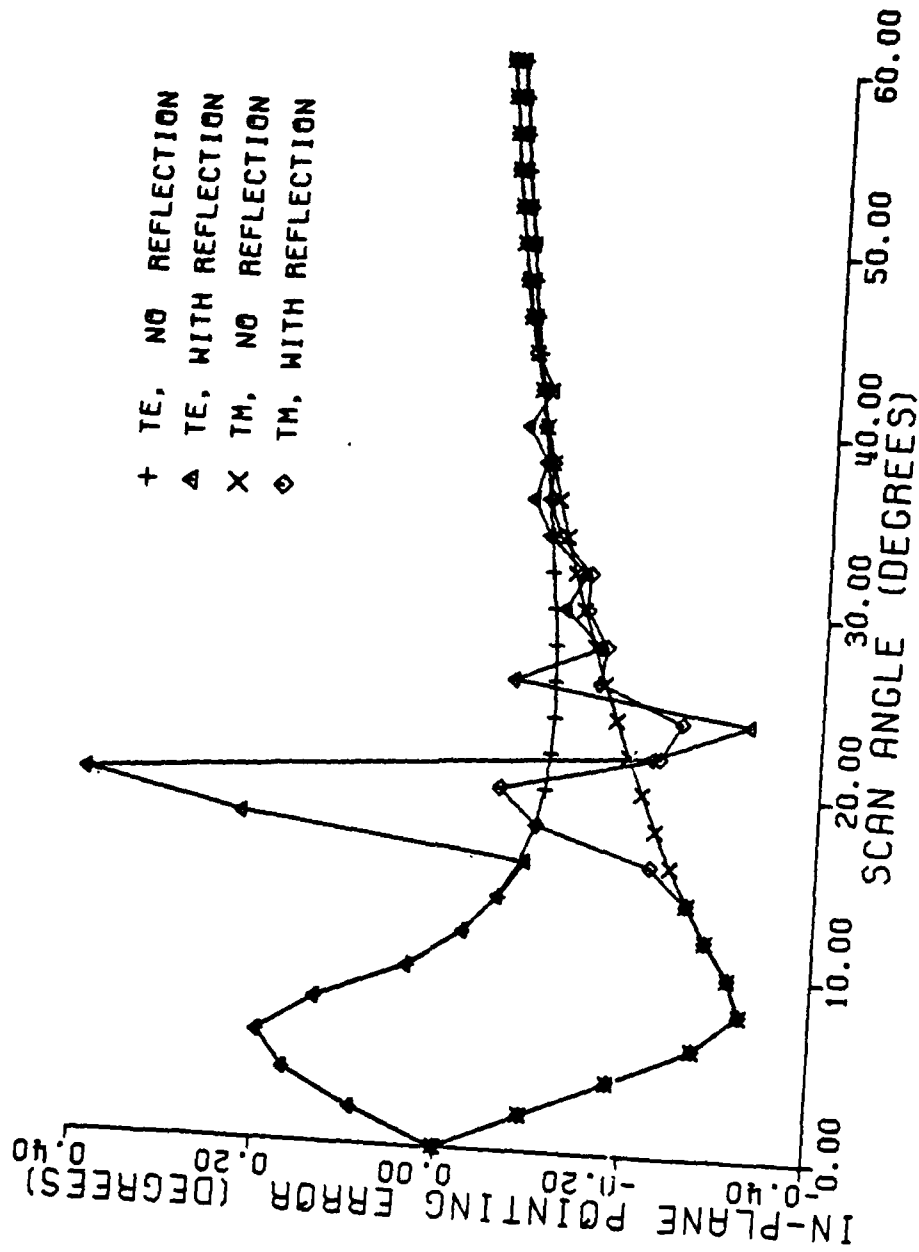


Figure 3-35. In-Plane Radar Pointing Error for Polyimide Quartz Radome with 60° Wall Design and Uniform Aperture Illumination Showing Effect of Internal Reflection.

aperture in the z' direction had different signs for TE and TM polarization. These different phase slopes lead to radar pointing errors in different directions. This could have serious implications for the tracking radar, since the indicated direction to the target could change by a large amount simply because of a change in the incident polarization.

The effect of internal reflection in Figure 3-35 again begins at a scan angle of about 12° . But now instead of causing a small perturbation on the no-reflection error curve, internal reflection causes large deviations from this curve. TE polarization is again seen to have the greater sensitivity to internal reflection effects. The large reflected fields that illuminate the aperture, as seen in Figures 3-31, are responsible for these large errors.

At large scan angles, say greater than 45° , internal reflection produces little effect on radar pointing error. As previously discussed, the reflection surface becomes highly transparent at the larger scan angles, thus less reflected energy is entering the aperture. Also at the larger scan angles, the reflected field has several cycles of phase variation over the aperture; thus, the integrated response to internal reflection is smaller. This last effect is similar to the response to a plane wave that enters the aperture through a side-lobe of the antenna pattern.

The effect of the aperture illumination function on radome-induced pointing error is considered next. In Chapter II it was noted that uniform aperture illumination produces a far-field antenna pattern

with a narrower main lobe than cosine tapered illumination, but higher sidelobe levels are associated with uniform illumination. When receiving, the aperture illumination function serves to weight the incident fields during aperture integration.

In-plane radar pointing error for the two principle polarizations and both aperture illuminations are shown in Figure 3-36 for the 75° wall design and in Figure 3-37 for the 60° wall design. Internal reflection is included for both figures. In each figure it is seen that cosine taper reduces the effect of internal reflection. This is because cosine taper reduces the contribution of fields near the aperture edge to the aperture integration.

However, at low scan angles, the radar pointing error is greater for the cosine-tapered illumination. This is thought to be due to the effect of fields near the shadow of the radome tip. In this shadow region the field is highly distorted because of the large variation of incidence angle in the tip region. At low scan angles, the tip shadow is near the aperture center (the region given highest weight by cosine taper), thus the aperture is responding to the most distorted part of the incident field.

So far, only polarization in the pure TE and TM directions has been considered for the incident field. Radar response to a diagonal, linearly-polarized incident field is now considered. Such a field has both TE and TM components as given by equation (3.9). The polarization angle, γ , indicated in Figure 3-17 will be used as a parameter. Diagonal

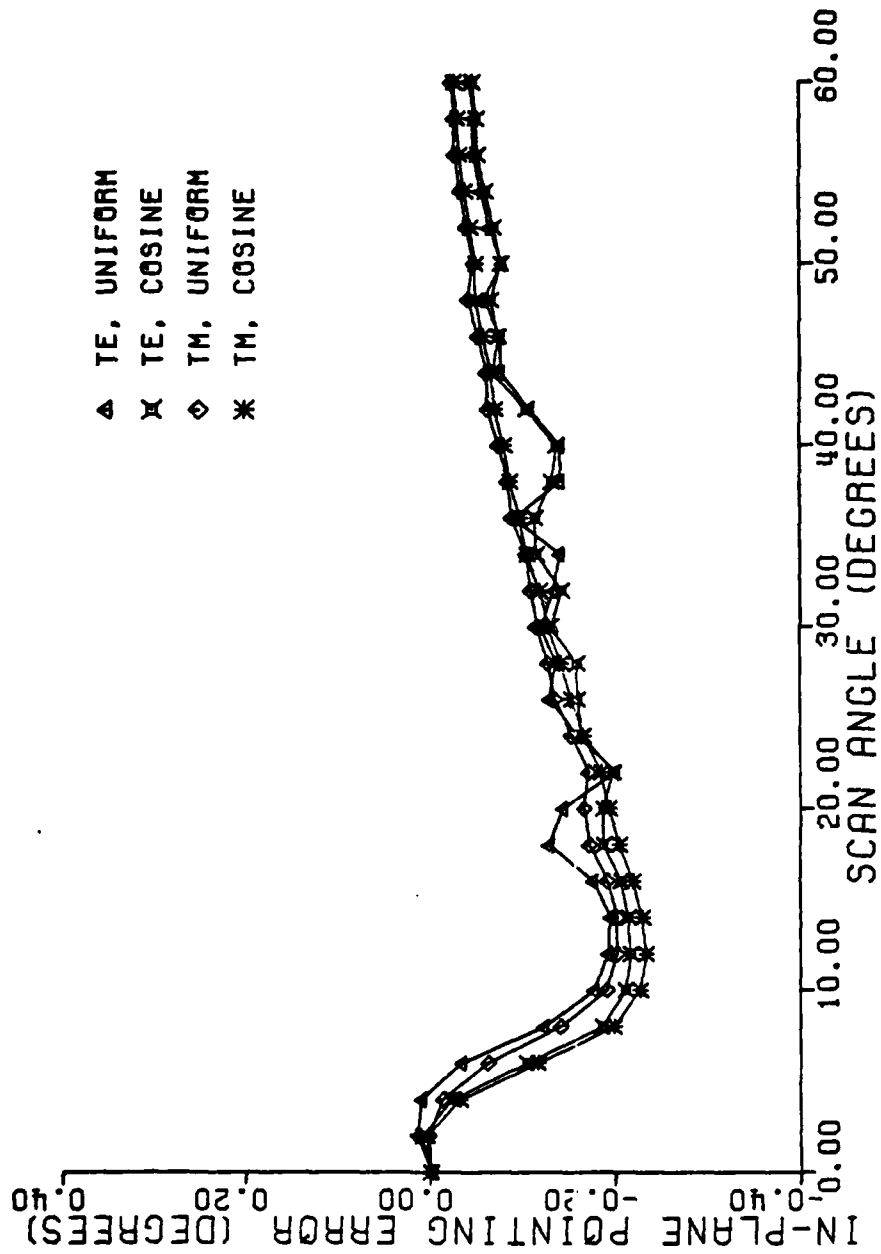


Figure 3-36. In-Plane Radar Pointing Error for Radome with 75° Wall Design Illustrating Effect of Aperture Illumination Function.

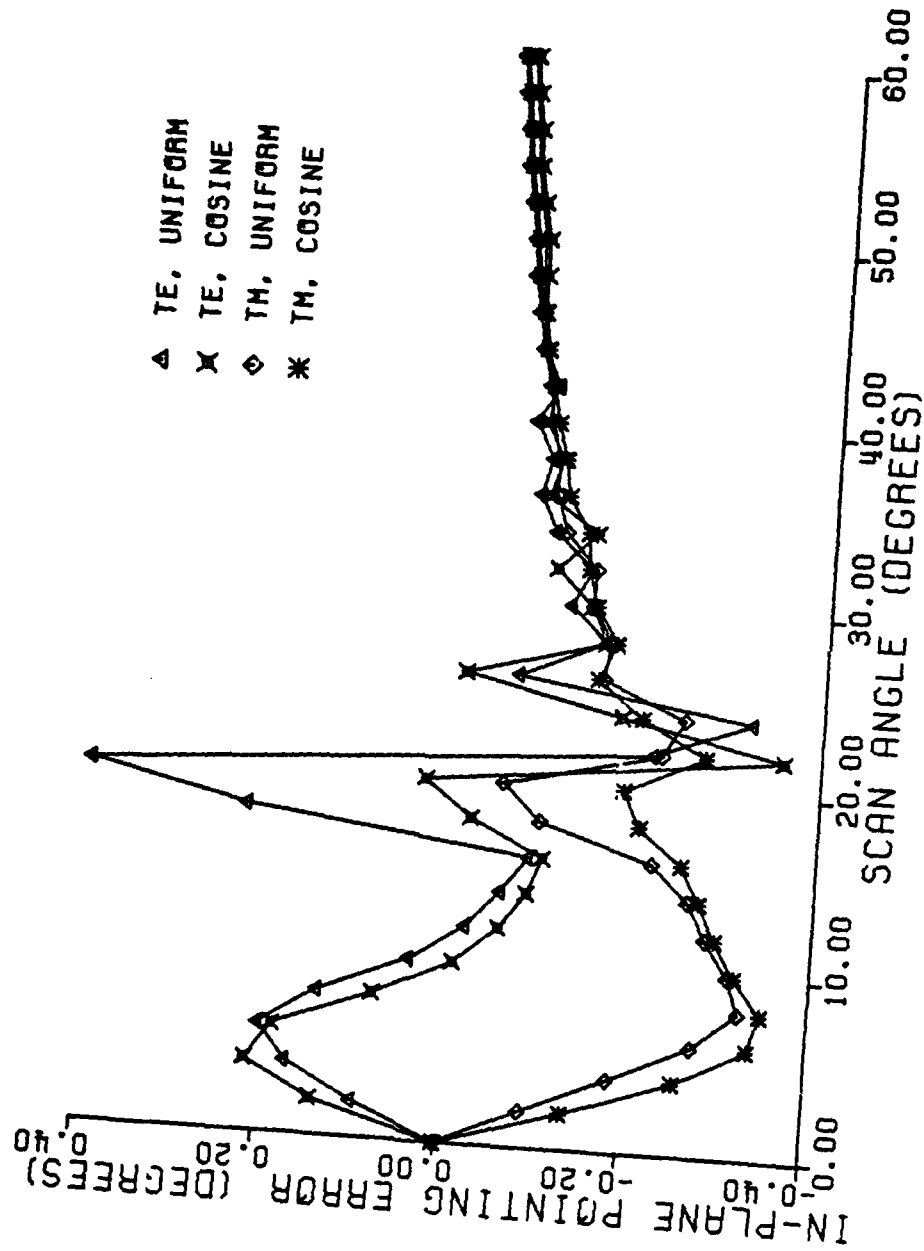


Figure 3-37. In-Plane Radar Pointing Error for Polyimide Quartz Radome with 60° Wall Design
Illustrating Effect of Aperture Illumination Function.

polarization leads to both in-plane and cross-plane radar pointing errors, as would be expected from the phase-front plots presented earlier.

In-plane radar pointing error versus scan angle, α , is shown in Figure 3-38 for the 75° wall design and in Figure 3-39 for the 60° wall design. Error curves are plotted for the polarization angles indicated. Uniform aperture illumination is used for both figures; and the effect of internal reflection is included. In Figure 3-38, it is seen that little variation in pointing error occurs as the polarization is changed. This is due to the near-equal insertion phase delay of the 75° wall design for parallel and perpendicular polarization. Thus, the phase delay in passing through the radome wall will be about the same whatever the incident polarization.

Something very different happens with the 60° wall design. The opposite-sign errors for TE polarization ($\gamma = 0^\circ$) and TM polarization ($\gamma = 90^\circ$) have been pointed out. Pointing error is now observed to take on intermediate values between these two as the polarization angle changes. The phase front across the aperture for $\alpha = 10^\circ$ was shown in Figures 3-15 through 3-20 for each of the linear polarization angles considered. It is interesting to see how the phase slopes relate to the radar pointing errors.

In addition to an average slope in the z' direction across the aperture, diagonal polarization leads to an average slope in the x'

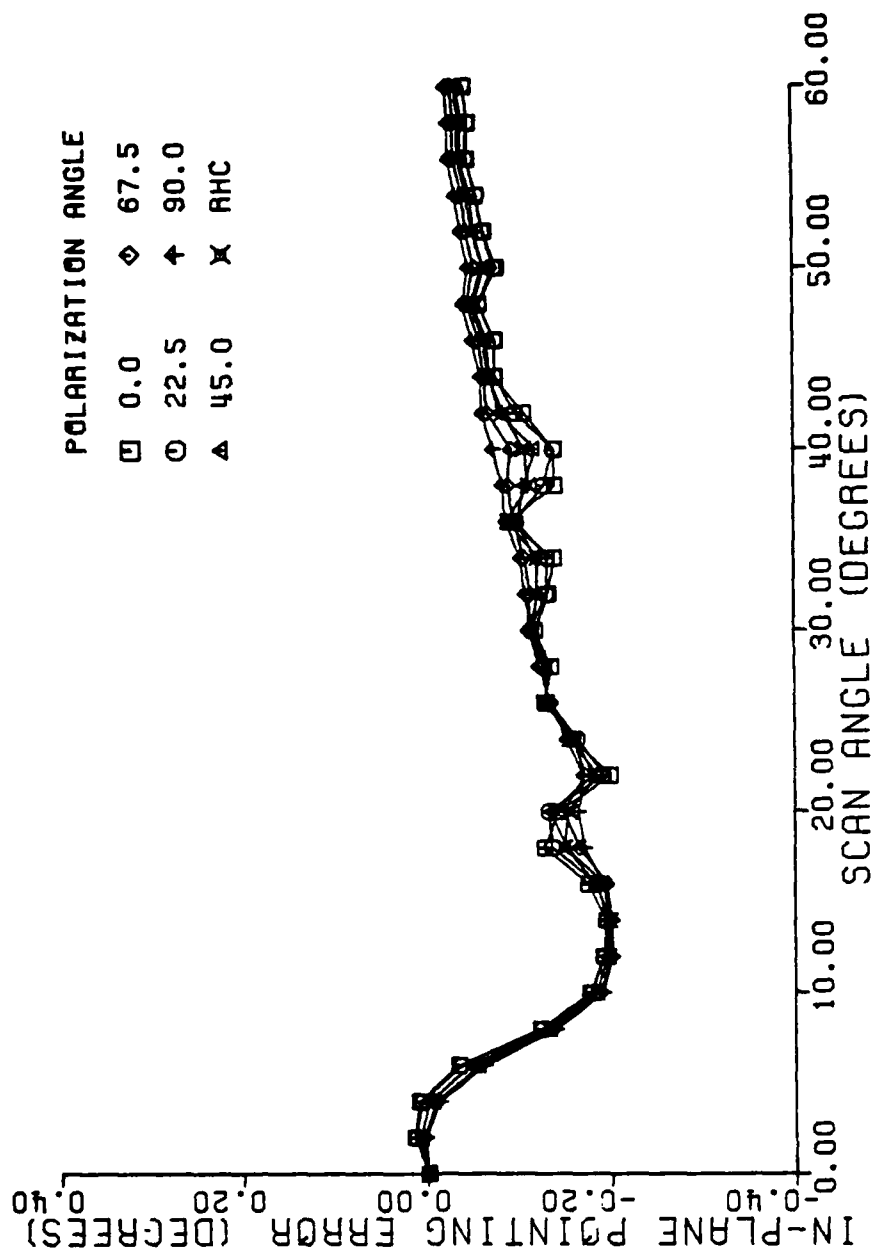


Figure 3-38. In-Plane Radar Pointing Error for Radome with 75° Wall Design and Various Incident Polarization.

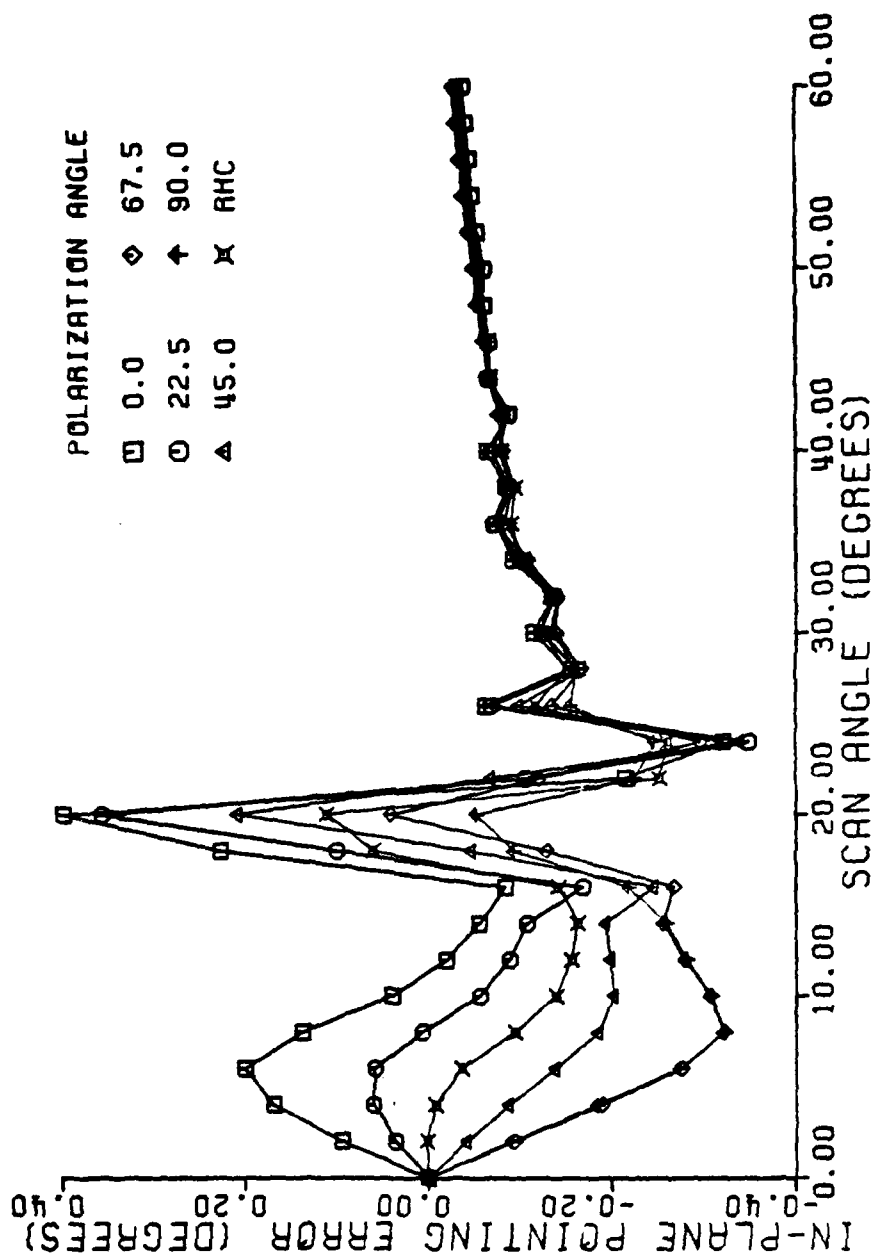


Figure 3-39. In-Plane Radar Pointing Error for Radome with 60° Wall Design and Various Incident Polarization.

direction. This average phase slope in the x' direction produces radar pointing error in the β scan angle or cross-plane pointing error. Monopulse signals are formed for the β scan direction in the same manner as for the α scan direction. The tracking radar measures the angle to the target in both the α and β directions simultaneously and repositions the antenna to obtain zero indicated error signals in both angles.

The antenna has zero cross-plane error when $\beta = 0$ according to the convention adopted for the incident field (see Figure 3-17). The cross-plane pointing error is thus taken to be the β scan angle of the antenna when the cross-plane monopulse signal is zero.

Cross-plane pointing error versus α scan angle is presented for the two radomes previously used for examples. Figure 3-40 is for the 75° wall design and Figure 3-41 is for the 60° wall design. Note that both radomes have zero error at $\alpha = 0$, but the cross-plane error for the 75° wall design rises slow and almost monotonically, while that of the 60° wall design rises to a peak at about $\alpha = 10^\circ$ and then decreases to small errors past $\alpha = 30^\circ$.

At first thought, it would seem that Figures 3-40 and 3-41 contain mistakes since the cross-plane error is not zero for 0° and 90° polarization, the symmetrical polarization states. The aperture phase front plots did show these fields as being symmetrical about $x' = 0$. But that which was plotted in these figures was the component of the field at the aperture with the same polarization as the incident field. Radome-induced distortion has mirror symmetry about the $x = 0$ plane. A TE or TM polarized antenna also has symmetry about the $x' = 0$ plane. However,

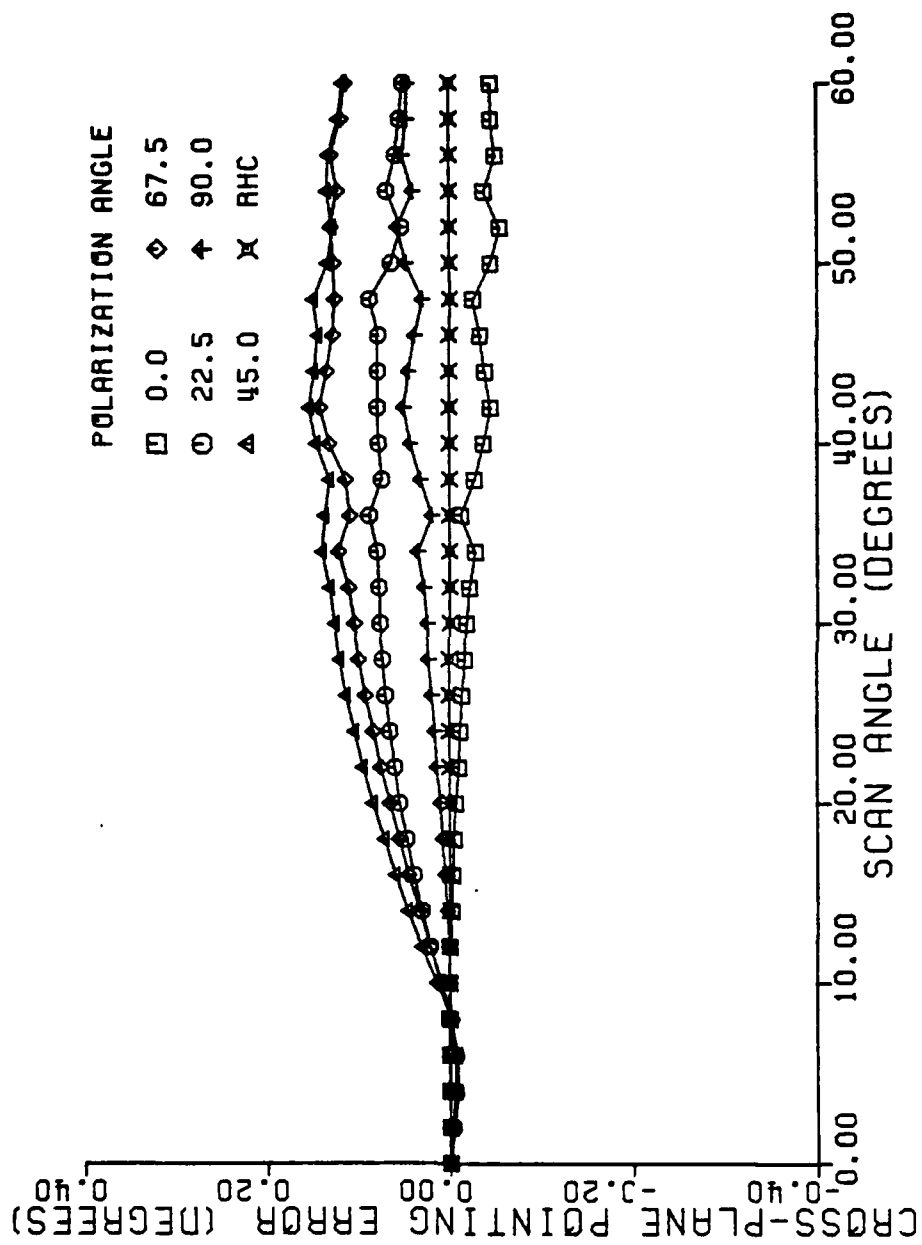


Figure 3-40. Cross-Plane Radar Pointing Error for Radome with 75° Wall Design and Various Incident Polarization.

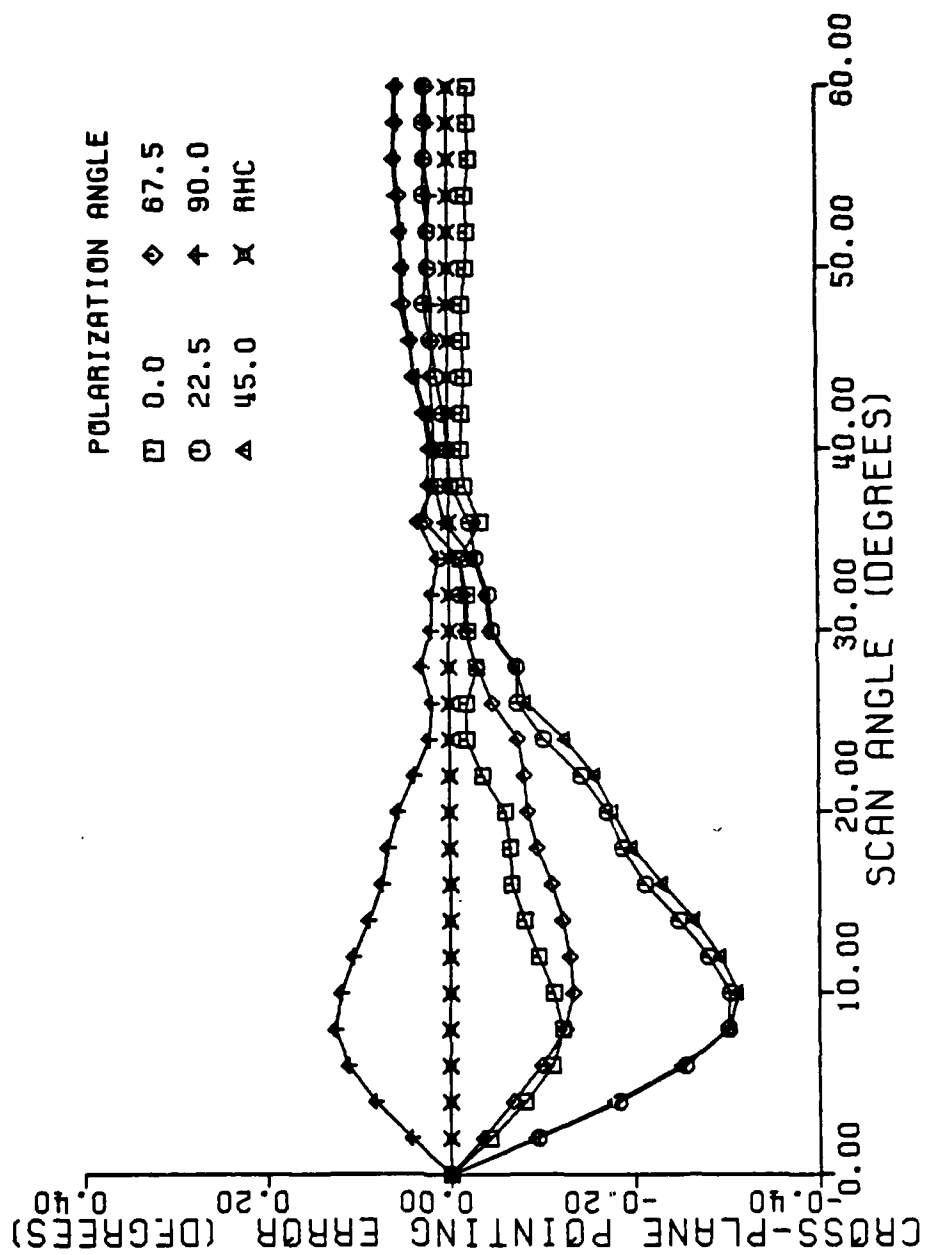


Figure 3-41. Cross-Plane Radar Pointing Error for Radome with 60° Wall Design and Various Incident Polarization.

a TE polarized antenna would have no cross-plane error at any scan angle when a TE polarized incident field is present; likewise a TM antenna has no cross-plane error when a TM field is incident.

The errors plotted in Figures 3-40 and 3-41 are for a right-hand circular-polarized receiving antenna. The circular-polarized antenna does not have mirror symmetry about the $x' = 0$ plane. Thus the circular-polarized antenna does not have zero pointing error even when symmetrically distorted fields are present.

A circular-polarized antenna has been used here so that the same antenna will receive all incident linear polarizations. If a linear-polarized antenna were used, the received signal level would drop substantially for cross-polarized incident fields. The radar pointing error due to a poor signal-to-noise ratio is likely to be much greater than the radome-induced pointing errors.

Pointing error curves for incident fields having the same polarization as the receiving antenna (RHC) are shown in Figures 3-38 through 3-41. For this case, no cross-plane error is present (again due to symmetry considerations). Both Figures 3-40 and 3-41 show that the pointing error for 0° polarization and 90° polarization are almost equal and opposite. Since circular polarization is made up of equal parts of these two polarizations, the net pointing error is zero.

It is also noted in the cross-plane error curves that maximum error is for 45° polarization at all scan angles. This is the polarization angle with maximum asymmetry.

In this chapter some fundamental concepts have been applied to obtain approximations for radome-induced distortion. Although the approach taken has been quite simple, it provides good insight into radome behavior. Throughout the chapter the relation of wavefront distortion to pointing error was stressed. Several of the factors necessary for a good radome have also been pointed out. Next, a technique to compensate for pointing error and some additional information available from monopulse are considered.

IV. RADOME-INDUCED RADAR POINTING ERROR CORRECTION

In this last major chapter, an error compensation technique is presented. The technique is easily implemented and should be quite effective in the digital-computer-controlled radar systems of today and the future. The second section of the chapter treats the relation of the complex indicated angle and radome-induced wavefront distortion. The relation of the complex indicated angle to some other sources of distortion has been presented in the literature, but treatment of the radome problem is thought to be new.

ERROR COMPENSATION

The concept of error compensation is very simple: if the error characteristics of a system are known a priori as a function of system parameters, then the error can be removed from the measured output to yield an error-free measurement. Of course, a sufficiently simple system is required so that each output can be uniquely associated with a given input. This is the case for radome-induced radar pointing errors.

The traditional approach to radome-induced error reduction is trial and error. Beginning with a wall design optimized for other system considerations (strength, erosion resistance, thermal properties, etc.), the pointing errors are then measured. Next the radome is "patched-up" by applying layers of dielectric tape to parts of the radome interior. The errors are measured again and the process is repeated until a con-

figuration having acceptable error characteristics is found. It is obvious that this procedure requires considerable experimental time spent by very experienced personnel. All this adds up to high costs.

In 1976 Loyet [43] presented a scheme for digitally compensating an angle tracking system for radome-induced error. The technique involves measuring the error characteristics of the system only once. The measured errors are then stored as a function of scan angle. In flight the radar is allowed to track normally, but the angle sent to the guidance computer is the actual angle of the antenna minus the pointing error for that angle as obtained by interpolating the stored error values.

There are several advantages of this technique over the traditional method. The system need be measured only once, thus range time is saved. No high-level expertise is required, as for patching. The technique is easy to implement with a microprocessor, which adds negligible weight to the system and can be tucked away in any unused space. By increasing the number of stored error values, the pointing error can be reduced to arbitrarily low levels; while some error always remains due to patching.

The remainder of this section presents a compensation scheme based on the error calculations of the previous chapter. An angle compensator will be easier to implement if little error is already present; thus a radome design having low initial error characteristics should be selected as a starting point. For the example to be considered here, the tangent ogive with constant wall thickness designed for 75° incidence will be used. The in-plane pointing error for this radome with the previously used antenna were presented in Figure 3-38.

Compensation for pointing error is accomplished by subtracting the pointing error at a given scan angle from that scan angle to obtain a new estimate of the target direction. The new estimate is given by,

$$\alpha' = \alpha - \alpha_e, \quad (4.1)$$

where α' is the new estimate of the α scan angle to the target, α is the scan angle of the tracking null, and α_e is the in-plane pointing error at α .

The scan angle to the target takes on a continuous range of values, but the errors can only be stored for a finite number of angles. To obtain the error for an arbitrary scan angle some sort of interpolation is necessary. Two methods suggested by Loyet for doing this are 1. to fit a polynomial to the nearest data points and 2. to fit an analytic expression to the entire set of data. The approach taken here is to simply perform linear interpolation between the nearest two data points to obtain a value for α_e . A scheme using second-order interpolation of the three nearest data points was found to offer no significant improvement.

The in-plane pointing error curve for 45° polarization was selected for the reference error curve. As seen in Figure 3-38, this error curve is near the average overall polarization angles. Reference data was stored for 6° increments beginning at $\alpha = 0$. Figure 4-1 shows the error in α' obtained by (4.1) as outlined above. This figure should be compared with the original error curve, Figure 3-38. The difference in ordinate scales is over six.

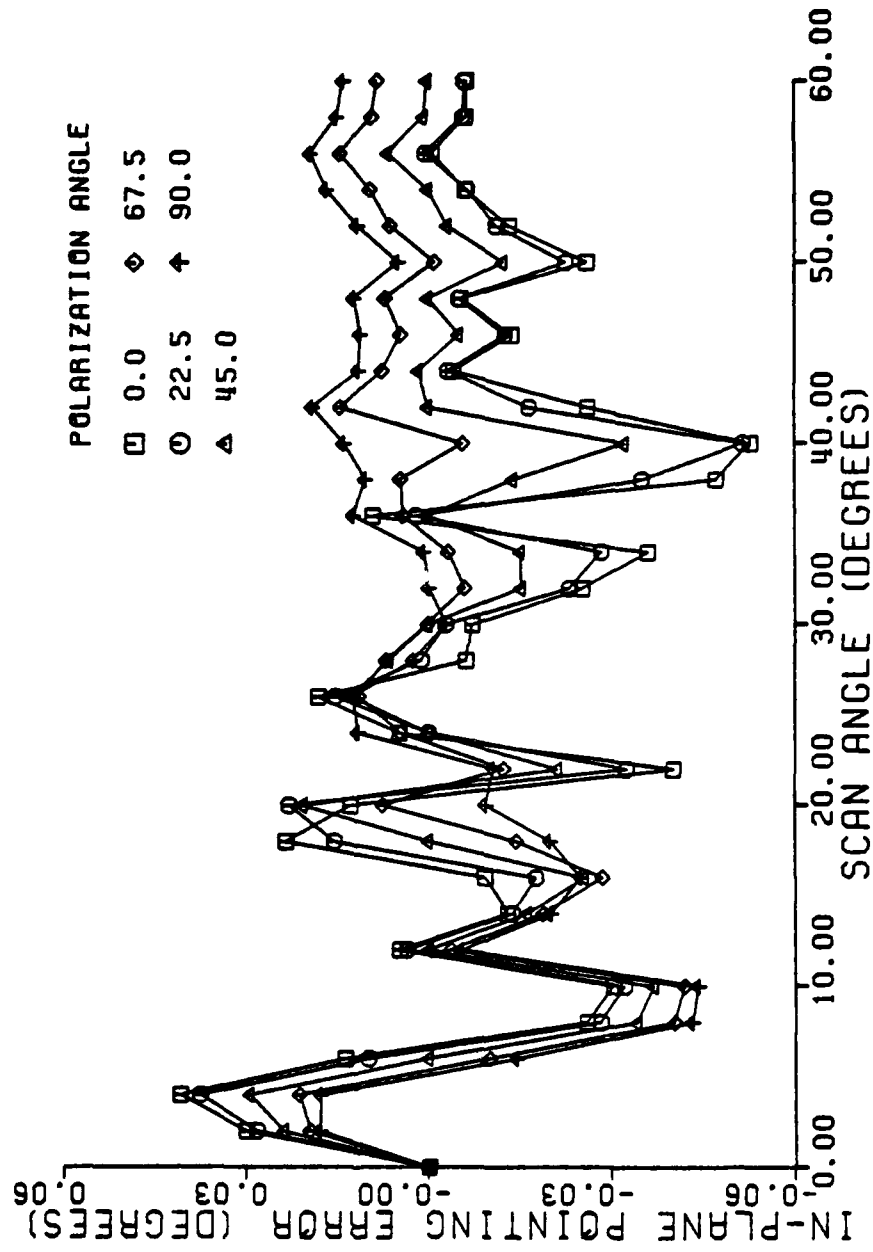


Figure 4-1. Remaining In-Plane Radar Pointing Error After Compensation.

Again error curves are shown for five polarization directions (γ in Figure 2-17). The error for 45° polarization is zero every 6° , and the other curves are generally on opposite sides of the 45° curve depending on whether γ is more or less than 45° .

The new pointing errors are smaller than the original at all scan angles except near zero where the compensation scheme actually increases the error. This is because linear interpolation of the error between 0° and 6° gives a negative error curve, while the actual error is positive. A better interpolation scheme might begin at $\alpha = 4^\circ$ and not apply error correction to angles less than 4° . Details such as this would need to be worked out for an actual system. This example is presented only to illustrate the method.

Another benefit of the error compensator is that the residual error curve is more rapidly varying and noise-like. This actually improves the system performance. Recall that one of the primary functions of the radar is to provide angle time-rate of change to the guidance computer. In the tracking scenario, the target is initially far off axis and moves toward the axis throughout the flight.

When the slope of the error curve is positive the radar will over estimate the angle rate of the target. Oscillatory flight characteristics may result as the missile trajectory is changed to intercept what appears to be a target with a high angle rate. When the error slope is negative, the target's angle rate is under estimated. This results in a sluggish missile response to target motion. Thus, the uncorrected system will over estimate the angle rate at the beginning of flight, while near the end of flight the rate will be under estimated.

Kuehne and Yost [44] have shown through computer simulation of missile flights that greatest accuracy is achieved when the radar pointing error changes slope frequently. Under these conditions, periods of target-angle-rate over estimation are rapidly followed by periods of under estimation and vice-versa. Filtering by the guidance loop and missile dynamics can reduce the effects of this type error. Thus the error tends to average to zero instead of having effects that accumulate with time.

The simple error correction technique presented here has great promise and should receive further attention in both system simulation studies and experimental verification.

This section will conclude with some comments on cross-plane errors. Cross-plane errors result from asymmetry in polarization and aperture illumination function. After the above discussion of in-plane error correction, the next question is logically--can the same thing be done for cross-plane errors?

Recall from the cross-plane error curves, Figures 3-40 and 3-41, that at a given α -scan angle the error is a function of polarization angle (γ in Figure 3-17). The cross-plane error is a zero-mean function of γ at any fixed scan angle. It can be shown that the cross-plane error curve versus γ has half-wave symmetry with period, π , that is,

$$\beta_e(\gamma) = -\beta_e(\gamma + \pi/2), \quad (4.2)$$

where β_e is the cross-plane error, γ is the polarization angle, and α is fixed. This is for a linear-polarized incident field and a circular-

polarized receiving antenna. For a linear-polarized receiving antenna the cross-plane error would be odd.

If the polarization of the received wave were linear with a rapidly changing radome direction with zero mean, the cross-plane error indicated by the radar would be zero. Also if the received wave were same-sense circular polarized there would be no cross-plane error, as seen before. Further consideration of the cross-plane error problem must be coupled with some knowledge of the scattering properties of the target.

As a last comment, it is noted that a very "smart" radar system could resolve the polarization of the incident field by use of a dual polarized antenna and necessary signal processing. Having determined this, error correction could be made as outlined before.

COMPLEX INDICATED ANGLE AND WAVEFRONT DISTORTION

In this section, a somewhat more general measure of radar pointing angle is discussed. This measure is known as the complex indicated angle (CA). In Chapter II, the incidence angle of a plane wave impinging on a radar antenna was determined from the ratio of the sum and difference output voltages by

$$\theta = K^{-1} \operatorname{Re}\left\{\frac{-j\Delta}{\Sigma}\right\}, \quad (4.3)$$

where θ is the incidence angle measured from boresight, K is the slope of the normalized difference pattern at boresight, and Δ and Σ are the difference and sum voltages respectively. {see (2.40)}

The real operator (Re) in (4.3) is not necessary when a plane wave is incident on the antenna, since it was shown in Chapter II that Δ and Σ are in phase quadrature in this case. However, when the incident field is not a plane wave, the phase of Δ and Σ generally differs by something other than 90° . In this case, the angle indicated by the radar may be considered as the complex quantity,

$$CA = K^{-1} \left[\frac{-j\Delta}{\Sigma} \right] . \quad (4.4)$$

Since a complex indicated angle is due to a non-planar wave at the antenna, the term "direction to the target" may have no meaning. However, the real and imaginary parts of the CA are due to specific attributes of the incident wave and, therefore, do provide information about the incident field.

Sherman [45] was the first to study the complex indicated angle. This work considered a distorted wave at the antenna due to the interference of two far-field targets with different amplitude, phase and direction. He showed that by processing the CA from several radar returns, the direction to each of the two targets could be determined although the targets were unresolvable with an ordinary monopulse radar. Sherman [46] further extended the theory of the CA to include the effects of multipath providing the second target return signal.

Peebles and Goldman [47] also considered the CA method for targets with multipath by examining the effects of the terrain surface reflection coefficient and system noise. They showed that the CA method provides

significant improvement in target location when the signal-to-noise ratio is greater than 20dB and the surface is almost planar. Subsequent experimental work [48] indicated that the assumption of a planar terrain was a severe limitation to the CA method for multipath because the roughness of the actual terrain led to diffuse scattering which caused ambiguities in the locations of the target and image.

To see how the complex angle method works for two targets or a target and its image over a planar terrain, consider two unequal amplitude plane waves incident on a monopulse antenna near boresight at angles θ_1 and θ_2 as measured from boresight. By the principle of superposition, the total sum and difference output voltages are the superposition of the voltages produced by the two plane waves acting alone. Thus, the complex angle is

$$CA = K^{-1} \left[\frac{-j\Delta_1 - j\Delta_2}{\Sigma_1 + \Sigma_2} \right] \quad (4.5)$$

where subscripts identify the source of the signals.

Since the signals arrive from near boresight, the difference voltages may be written in terms of the sum voltages and the angles of arrival by the use of (2.40).

This yields,

$$CA = K^{-1} \left[\frac{\theta_1 \Sigma_1 + \theta_2 \Sigma_2}{\Sigma_1 + \Sigma_2} \right] \quad (4.6)$$

Dividing numerator and denominator of (4.6) by Σ_1 simplifies the expression for CA to

$$CA = K^{-1} \left[\frac{\theta_1 + \theta_2 a \exp(j\phi)}{1 + a \exp(j\phi)} \right] \quad (4.7)$$

where Σ_2/Σ_1 has been expressed as an $\exp(j\phi)$. This is the general form for the complex angle produced by two plane waves.

Several things are to be noted about CA. First, if signal 2 vanishes, ($a=0$) then the radar indicates the direction to the source of 1, θ_1 . Likewise if 1 vanishes, the indicated angle is in the direction of source 2. However, if both signals are present, the CA is truly complex and CA depends on the ratio of amplitudes and the phase difference as well as the angles of arrival. The real part of CA is no longer an indicator of the direction of arrival of either wave and in fact, it may indicate the "source" to be well outside the angular region subtended by the two targets, a fact confirmed by glint and multipath studies.

The complex angle technique for resolution is based on the observation that the CA (4.7) is a bilinear transformation [49] of $\exp(j\phi)$. Hence, as $\exp(j\phi)$ traces a circle in the complex plane as ϕ varies through 360° , the CA also traces a circle in the complex plane. The radius of the CA circle is determined by the constant a .

The method proposed by Sherman was to display the CA on a properly calibrated oscilloscope screen. Since the relative phase of the two target returns, ϕ , will be rapidly varying due to the motion of the targets, the spot on the screen would trace a circle. The constant a is then determined from the circle radius.

Equation (4.7) could then be solved for θ_1 and θ_2 by decomposing the complex equation into two real equations.

Although the above approach gives the mechanics of the complex angle technique, it is only a signal analysis approach and gives little insight into the structure of the fields that are incident on the aperture. Radome-induced wavefront distortion is the source of a complex indicated angle which is far more complicated than the two plane wave case. In order to understand how this arises, it is necessary to begin at the aperture.

To illustrate how the CA arises for radome distortion, the aperture integrations used in Chapter III will be reduced to one dimension and the incident field will be assumed to have only one vector component. With these restrictions, the aperture integration (3.15) reduces to

$$\Sigma = \int_{-w}^w f(x)g(x)dx, \quad (4.8)$$

$$\Delta = \int_{-w}^w f(x)g_d(x)dx, \quad (4.9)$$

where $f(x)$ is the incident field; $g(x)$ is the sum illumination function, $g_d(x)$ is the difference illumination function, and $2w$ is the aperture width. Recall that g must be even and g_d must be odd. Also g and g_d are assumed to be real.

The incident field, $f(x)$, is a complex function and can be decomposed into the sum of even and odd functions according to

$$f = f_{re} + jf_{ie} + f_{ro} + jf_{io}, \quad (4.10)$$

where subscripts e and o are for even and odd, subscripts r and i indicate real and imaginary, and each f_{xx} is real. The sum and difference signals can be written as

$$\Sigma = \Sigma_r + j\Sigma_i \quad (4.11)$$

$$\Delta = \Delta_r + j\Delta_i \quad (4.12)$$

where

$$\Sigma_r = \int f_{re} g dx, \quad (4.13)$$

$$\Sigma_i = \int f_{ie} g dx, \quad (4.14)$$

$$\Delta_r = \int f_{ro} g dx, \quad (4.15)$$

$$\Delta_i = \int f_{io} g dx, \quad (4.16)$$

the limits of integration are as for (4.8) and full advantage has been taken of the properties of even and odd functions integrated over symmetrical limits. The complex angle is now expressed by

$$CA = K^{-1} \frac{\Delta_i - j\Delta_r}{\Sigma_r + j\Sigma_i} \quad (4.17)$$

which can be rewritten as

$$CA = K^{-1} \frac{(\Sigma_r \Delta_i - \Sigma_i \Delta_r) - j(\Sigma_i \Delta_i + \Sigma_r \Delta_r)}{\Sigma_r^2 + \Sigma_i^2} \quad (4.18)$$

Recall that in the case of the single off-axis plane wave the even and odd components are in phase quadrature and (4.18) predicts a purely real CA.

Examination of the imaginary part of (4.18) reveals that CA becomes complex when the sum and difference voltages are no longer in phase quadrature. This may arise in the case of two or more plane waves incident on

the aperture or because of radome distortion. One of the goals of this study has been to determine if the imaginary part of the CA would provide additional information that could be used to reduce radar pointing error due to radomes. After examination of the simulation results of the previous chapter, it was concluded that the imaginary part of CA could not be uniquely related to radar pointing error but appeared to correlate with phase front curvature. Thus, this quantity is not considered useful for pointing error correction.

V. CONCLUSION

A high-frequency analysis of the tangent ogive radome has been presented. Geometric optics has been used to account for propagation of the electromagnetic field inside the radome that is due to a plane wave incident on the exterior. Transmission and reflection of the field at the radome surface was obtained by treating the wall and the wave as locally planar and applying plane-wave transmission and reflection coefficients. The principles of monopulse radar were also reviewed.

It was shown that radar pointing error results from distortion in the incident field at the antenna. Such distortion is caused by the transmission properties of the wall and by reflections from the wall interior. Both these distortion mechanisms were seen to be functions of incident angle and polarization. Pointing errors were found for both scan planes of the antenna aperture. It was seen that asymmetry of the incident polarization leads to cross-plane errors while in-plane errors exist for any polarization state.

Complex angle processing for the purpose of pointing angle reduction was investigated based upon the simulation described above. It was concluded that the complex angle could not be uniquely related to radar pointing error, but rather appeared to correlate with phase front curvature. This quantity is not considered useful for pointing error correction.

A simple, but effective, method to compensate for pointing error was demonstrated. This technique could be applied to any radome with good results.

This analysis has considered some of the fundamental factors that give insight into radome performance. Evaluation of the results presented can only be based on experiments that both validate and indicate areas for improvement. Such experiments would certainly include comparisons of this work with measured pointing errors and with plots of the fields inside the radome. A very interesting area for future work, both analytical and experimental, is the effect of the radome tip. Tip effects may well account for many differences in measured and theoretical results.

REFERENCES

- [1] F. Jay (Editor-In-Chief), IEEE Standard Dictionary of Electrical And Electronic Terms, Second Edition. New York: IEEE, 1977, p. 555.
- [2] M. I. Skolnik, Introduction to Radar Systems. New York: McGraw-Hill, 1962, p. 344.
- [3] W. M. Cady, M. B. Karelitz, and L. A. Turner (Eds.), Radar Scanners and Radomes. New York: McGraw-Hill, 1948.
- [4] S. Silver (Ed.), Microwave Antenna Theory and Design. New York: McGraw-Hill, 1949.
- [5] G. Tricoles, "Radiation Patterns and Boresight Error of a Microwave Antenna Enclosed in an Axially Symmetric Dielectric Shell," J. Opt. Soc. Am., Vol. 54, pp. 1094-1101, September 1964.
- [6] ———, "Application of ray tracing to predicting the properties of a small, axially symmetric, missile radome," IEEE Trans. Antennas and Propagation, Vol. AP-14, pp. 244-246, March 1966.
- [7] D. T. Paris, "Computer-aided radome analysis," IEEE Trans. Antennas and Propagation, Vol. AP-18, pp. 7-15, January 1970.
- [8] ———, "Digital computer analysis of aperture antennas," IEEE Trans. Antennas and Propagation (Communications), Vol. AP-16, pp. 262-264, March 1968.
- [9] D. C. F. Wu and R. C. Rudduck, "Plane wave spectrum-surface integration technique for radome analysis," IEEE Trans. Antennas and Propagation, Vol. AP-22, pp. 497-500, May 1974.
- [10] M. I. Skolnik (Editor-In-Chief), Radar Handbook. New York: McGraw-Hill, 1970, Chapter 14.
- [11] H. Jasik (Ed.), Antenna Engineering Handbook. New York: McGraw-Hill, 1961, Chapter 32.
- [12] T. E. Tice and J. D. Walton, Jr. (Eds.), Techniques for airborne radome design," Air Force Avionics Laboratory, Tech. Rept. AFAL-TR-66-391, Vols. I and II, December 1966.
- [13] J. D. Walton, Jr. (Ed.), Radome Engineering Handbook. New York: Marcel Dekker, 1970.

- [14] O. Tornani (Ed.), "Radomes, advanced design," North Atlantic Treaty Organization, Advisory Group for Aerospace Research and Development, Advisory Report AGARD-AR-53, March 1973.
- [15] R. H. Cary (Ed.), "Avionic Radome Materials," North Atlantic Treaty Organization, Advisory Group for Aerospace Research and Development, Advisory Report AGARD-AR-75, October 1974.
- [16] M. I. Skolnik, Introduction to Radar Systems. New York: McGraw-Hill, 1962, pp. 175-184.
- [17] D. K. Barton, Radar System Analysis. Englewood Cliffs. NJ: Prentice-Hall, 1964, pp. 269-275.
- [18] D. R. Rhodes, Introduction to Monopulse. New York: McGraw-Hill, 1959.
- [19] D. K. Barton (Ed.), Radars, Volume 1, Monopulse Radar. Dedham, MA: Artech House, 1974.
- [20] D. D. Howard, "Radar target angular scintillation in tracking and guidance systems based on echo signal phase front distortion," Proc. National Electronics Conference, Vol. XV, pp. 840-849, 1959.
- [21] G. C. Evans, "Influence of ground reflections on radar target-tracking accuracy," Proc. IEEE, Vol. 113, pp. 1281-1286, August 1966.
- [22] R. S. Berkowitz and S. M. Sherman, "Information derivable from monopulse radar measurements of two unresolved targets," IEEE Trans. Aerospace and Electronics Systems (Correspondence), Vol. AES-7, pp. 1101-1013, September 1971.
- [23] P. C. Clemmow, The Plane Wave Spectrum Representation of Electromagnetic Fields. Oxford, England: Pergamon Press, 1966.
- [24] R. J. Sims and E. R. Graf, "The reduction of radar glint by diversity techniques," IEEE Trans. Antennas and Propagation, Vol. AP-19, pp. 462-468, July 1971.
- [25] W. V. T. Rusch and P. D. Potter, Analysis of Reflector Antennas. New York: Academic Press, 1970.
- [26] A. W. Love (Ed.), Reflector Antennas. New York: IEEE Press, 1978.
- [27] R. E. Collin and F. J. Zucker (Eds.), Antenna Theory, Part 1. New York: McGraw-Hill, 1969, Chapter 4.
- [28] R. F. Harrington, Time-Harmonic Electro-magnetic Fields. New York: McGraw-Hill, 1961, pp. 100-103.

- [29] Ibid. pp. 106-110.
- [30] Ibid. p. 117.
- [31] V. H. Rumsey, "The reaction concept in electromagnetic theory," Phys. Rev., Ser. 2, Vol. 94, pp. 1483-1491, June 15, 1954.
- [32] A. Papoulis, The Fourier Integral and Its Applications. New York: McGraw-Hill, 1962, pp. 11-13.
- [33] D. K. Barton and H. R. Ward, Handbook of Radar Measurement. Englewood Cliffs, NJ: Prentice-Hall, 1969, p. 19.
- [34] R. E. Collin, Field Theory of Guided Waves. New York: McGraw-Hill, 1960, pp. 87-94.
- [35] L. A. Robinson, "Electrical properties of metal-loaded radomes," Wright Air Development Division Tech. Rept. 60-84, February 1960. ASTIA-AD 249410.
- [36] R. F. Harrington, op. cit., pp. 98-100.
- [37] F. A. Jenkins and H. E. White, Fundamentals of Optics Fourth Edition. New York: McGraw-Hill, 1976, pp. 28-29.
- [38] F. Jay, op. cit., p. 67.
- [39] "System 360 Scientific Subroutine Package, Version III, Programers Manual," IBM Application Program GH20-0205-4 Fifth Edition, pp. 217-218, August 1970. Subroutine RTMI.
- [40] M. V. Klein, Optics. New York: John Wiley and Sons, 1970, p. 189.
- [41] G. Tricoles and N. H. Farhat, "Microwave holography: applications and techniques," Proc. IEEE, Vol. 65, pp. 108-121, January 1977.
- [42] E. C. Jordan and K. G. Balmain, Electromagnetic Waves and Radiating Systems Second Edition. Englewood Cliffs, NJ: Prentice-Hall, 1968, pp. 459-460.
- [43] D. L. Loyet, "Digitally compensated angle tracking system," Proc. Thirteenth Symposium on Electromagnetic Windows, Georgia Institute of Technology, pp. 115-119, September 21-23, 1976.
- [44] B. E. Kuehne and D. J. Yost, "When are boresight error slopes excessive?" Proc. Fourteenth Symposium on Electromagnetic Windows, Georgia Institute of Technology, pp. 59-64, June 21-23, 1978.

- [45] S. M. Sherman, "Complex indicated angles in monopulse radar," Ph.D. Dissertation, University of Pennsylvania, December, 1965.
- [46] S. M. Sherman, "Complex indicated angles applied to unresolved radar targets and multipath," IEEE Trans. Aerospace and Electronics Systems, Vol. AES-7, pp. 160-170, January, 1971.
- [47] P. Z. Peebles and L. Goldman, "Radar performance with multipath using the complex angle," IEEE Trans. Aerospace and Electronics Systems, Vol. AES-7, pp. 171-178, January, 1971.
- [48] D. D. Howard, S. M. Sherman and D. N. Thompson, "Experimental results of the complex indicated angle technique for elevation measurements in the multipath region," Proc. 19th Tri-Service Symposium, pp. 329-346, July, 1973.
- [49] R. V. Churchill, J. W. Brown, and R. F. Verhey, Complex Variables and Applications, 3rd Ed. New York: McGraw Hill, 1974, pp. 78-80.
- [50] S. L. Watkins, "Masked Three-Dimensional Plot Program with Rotations," Communications of the ACM., Vol. 17, pp. 520-523, September, 1974.

APPENDIX

This appendix contains a complete listing of the FORTRAN program used to compute radome-induced radar pointing error. The program is extensively documented and even a cursory reading of the comment cards reveals much about the computations that are performed.

The program requires approximately three seconds for an IBM 370, Model 155 to execute one aperture integration over an $8\lambda_0$ diameter aperture with $\frac{1}{2}\lambda_0$ spaced rays, including reflected rays. Subroutine RTMI, called by subroutine INTRSC, is contained in the IBM Scientific Subroutine Package (SSP) [39] and, therefore, is not contained in this listing.

The surface plots presented in Chapter III were generated by a modified version of a plotting program presented by Watkins [50].

MAIN 1

```

C
C THIS PROGRAM COMPUTES RADAR POINTING ERROR
C FOR A CIRCULAR POLARIZED ANTENNA UNDER A
C TANGENT OGIVE RADDOME
C
C THE INCIDENT FIELD IS LINEAR POLARIZED
C RADAR POINTING ERROR IS CALCULATED FOR VARYING
C ANGLES OF INCIDENCE AND POLARIZATION DIRECTION
C
REAL ARG(90),ERRRCA(90),ERRRCB(90)
REAL CAAMP1(90),CAAMP2(90),CAPHS1(90),CAPHS2(90)
COMPLEX EXI,EYI,EZI,EPEX,EPEY,EPEZ,EPAX,EPAY,EPAZ
COMPLEX TPER,TPAR,RPER,RPAR,CEXP,CMPLX,J/(0.,1.)/
COMPLEX SUMA,SUMB,DIFA,DIFB
COMPLEX EXT,EYT,FZT,ETTM,EXR,EYR,EZR,ERTM
COMPLEX PHASE,EXITE,EYITE,EZITE,EXITM,EYITM,EZITM
COMPLEX FMAG1,FMAG2,PHASOR,CAA,CAB
COMPLEX SPANML,EPANX,EPANY,EPANZ,ERGT
REAL NX,NY,NZ,MONDSF(3),PI/.314159321/
INTEGER LABEL(2)/'ALPH','BETA'/
EQUIVALENCE (XP,XM),(ZP,ZM),(COSANG,AZ),(SINANG,AY)
C
COMMON/RDATA/ AL2,C,XM2,TTHETA,RAD,ARC
COMMON/MESPOS/ XM,YM,ZM
COMMON /HEIGHT/ APRAD,IMS,RHCAP
COMMON/TH/THIK
C
PHASOR(X)=CMPLX(COS(X),SIN(X))
C
DTR=PI/180.
RTD=180./PI
SQRT2=SQRT(2.0)
C
INITIALIZE TRANSMISSION COEFFICIENT ARRAYS
CALL INIT(31)
C
ALL DIMENSIONS IN MAIN ARE NORMALIZED TO WAVELENGTH
BETAK=2.*PI
C
RADDOME PARAMETERS (OUTER SURFACE)
RAD RADDOME RADIUS AT BASE
W RADDOME DIAMETER AT BASE
APCOUT RADDOME GENERATING ARC
FINSS RADDOME HEIGHT/DIAMETER
YG DISTANCE OF GIMBAL POINT FROM BASE PLANE
C
READ RADDOME AND ANTENNA PARAMETERS
READ (5,201) RAD,FINSS,YG,APDIA

```

```

201 FORMAT(4F10.0)
RADIN=RAD-THIK
RADIN2=RADIN*RADIN
W=2.*RAD
ARCOU=(FINISS*FINISS+0.25)*W
ARCIN=ARCOU-THIK
C=ARCOU-RAD
HIGH=SQRT((2.*ARCOU-RAD)*RAD)

```

```

C
C   WRITE RADOME PARAMETERS
C   WRITE(6,105) W,HIGH,FINISS
105 FORMAT(' ', 'RADOME DATA',/, ' BASE=',F7.4,/,
# ' HEIGHT=',F7.4,/, ' FINISS RATIO=',F6.2,/)

```

```

C
C   READ COMPUTATION OPTIONS
C   READ(5,202)NANG,IMS,IREFOS,MAXPNT,NANGE,IREFL,
#DELANG,DELZ,ERRMAX

```

```

202 FORMAT(I2,5I1.3X,3F10.0)
APRAD=APDIA/2.

```

```

DELX=DELZ
NUMELZ=APDIA/DELZ+1.5
NUMELX=NUMELZ
FIRSTZ=DELZ*(NUMELZ/2)
MONDSF(1)=1.028/(1.617*APDIA)
MONDSF(2)=1.2965/(1.9117*APDIA)
ERRMAX=ERRMAX*DTR

```

```

WRITE(6,103)YG,APDIA,IMS,IREFOS,IREFL
103 FORMAT(' ', 'ANTENNA GIMBAL POINT =',F4.2, ' LAMDA',/
# ' APERTURE DIAMETER =',F4.2, ' LAMDA',/, ' IMS=',I2,
#/, ' IREFOS =',I2,/, ' IREFL=',I2)

```

```

C
C   IF IREFOS=1 ANTENNA IS REPOSITIONED UNTIL REAL(CA)<
C   ERRMAX. AND ERROR IS GIMBAL ANGLE-INCIDENT ANGLE

```

```

C
C   IF IREFOS=0 ANTENNA IS NOT REPOSITIONED AND ERROR IS
C   REAL(CA) WHEN GIMBAL ANGLE IS AT INCIDENT ANGLE

```

```

C   DANGE=90.0/(NANGE-1)*DTR

```

```

C
C   DO 700 ITETM=1,NANGE
C   ANGE=(ITETM-1)*DANGE
C   SINANG=SIN(ANGE)
C   COSANG=COS(ANGE)
C   DO 400 IANG=1,NANG

```

```

C
C   COMPUTE ANGLE OF INCIDENT WAVEFRONT
C   ANGI=90.-(IANG-1)*DELANG
C   WRITE(6,104) ANGI

```


MAIN 3

```

104 FORMAT(' ', 'INCIDENT ANGLE=', F6.2, 'DEGREES')
    ARG(IANG)=90.0-ANGI
    ANGI=ANGI*DTR
    TTHETA=TAN(ANGI)
C
C    COMPUTE DIRECTION COSINES OF INCIDENT RAYS
C    OUTWARD DIRECTION ASSUMED POSITIVE
    AX=0.0
    AY=SIN(ANGI)
    AZ=COS(ANGI)
C
C    FIND DIRECTION OF UNIT AMPLITUDE INCIDENT E-FIELD
C    TE TO Y CASE: EXI=1.0, EYI=0.0, EZI=0.0
C
C    TM TO Y CASE: EXI=0.0, EYI=+COS(ANGI), EZI=-SIN(ANGI)
    EXITEO=1.0
C
    FYITMO=COS(ANGI)
    EZITMO=-SIN(ANGI)
C
C    SET INITIAL POINTING ANGLE TO INCIDENT ANGLE
    ALPHA=90.0*DTR-ANGI
    BETA=0.0
C
    DO 300 IPOINT=1,MAXPNT
C
    COSALF=COS(ALPHA)
    SINALF=SIN(ALPHA)
    COSBET=COS(BETA)
    SINBET=SIN(BETA)
    TANALF=TAN(ALPHA)
C
C    SUMA AND DIFA ARE MONOPULSE SIGNALS IN THE
C    IN-PLANE DIRECTION (ALPHA SCAN ANGLE)
C
C    SUMB AND DIFB ARE MONOPULSE SIGNALS IN THE
C    CROSS-PLANE DIRECTION (BETA SCAN ANGLE)
C
C    ZERO SUM AND DIF
    SUMA =(0.,0.)
    SUMB =(0.,0.)
    DIFA =(0.,0.)
    DIFB =(0.,0.)
C
    ARC=ARCCOT
    AL2=ARC*ARC
C
C    PERFORM APERTURE INTEGRATION OF DIRECT FIELD

```

MAIN 4

```

DO 50 IX=1,NUMELX
XMO=FIRSTZ-(IX-1)*DELX
C (XM,YM,ZM) ARE RADOME COORDINATES OF INTEGRATION POINT
C (XMO,O.,ZMO) APERTURE COORDINATES OF INTEGRATION POINT
C
DO 150 LI=1,NUMELZ
ZMO=FIRSTZ-(LI-1)*DELZ
C
C CHECK FOR MEASUREMENT POINT OUTSIDE APERTURE
RHOAP=SQRT(ZMO*ZMO+XMO*XMO)
IF(RHOAP.GT.APRAD)GO TO 150
C
C ROTATE ANTENNA SAMPLE POINTS FOR THE GIMBALED ANTENNA
XM=COSBET*XMO
YM=COSALF*SINBET*XMO-SINALF*ZMO+YG
ZM=SINALF*SINBET*XMO+COSALF*ZMO
C
C FIND INTERSECTION OF RAY AND RADOME
ZR1=SQRT(RAD*RAD-XM*XM)
CALL INTRSC(X,Y,Z,ZM,ZR1)
C
C FIND SURFACE NORMAL AT RAY-RADOME INTERSECTION
CALL NORM(X,Y,Z,NX,NY,NZ)
C
C DETERMINE INCIDENT ANGLE OF RAY AT TRANSMISSION POINT
THETA1=ARCOS(AY*NY+AZ*NZ)
C
C FIND BINORMAL
B=(N X A)/ABS(N X A)
CALL CROSS(NX,NY,NZ,O.O,AY,AZ,BX,BY,BZ)
C
C COMPUTE COMPLEX INCIDENT FIELDS AT ANTENNA
PHASE=PHASOR(BETAK*(ZM*AZ+YM*AY))
C
EXITE=EXITFO*PHASE
EYITM=EYITMO*PHASE
EZITM=EZITMO*PHASE
C
FXI=EXITE*COSANE
EYI=EYITM*SINANE
EZI=EZITM*SINANE
C
C FIND PARALLEL AND PERPENDICULAR COMPONENTS
C OF INCIDENT FIELD AT TRANSMISSION POINT
CMAG1=BX*FXI+BY*EYI+BZ*EZI
EPFX=BX*CMAG1
EPFY=BY*CMAG1

```

AD-A085 263

AUBURN UNIV ALA ENGINEERING EXPERIMENT STATION

F/G 17/9

INVESTIGATION OF COMPLEX ANGLE PROCESSING TO REDUCE RADOME INDU--ETC(U)

OCT 79 D G BURKS, E R GRAF

DAAK40-77-C-0022

UNCLASSIFIED

AU-EE-0022

NL

3 OF 3

AD-A085-263



END

DATE

FILED

6-80

DTIC

MAIN 5

```

C      EPEZ=BZ*EMAG1
C      EPAX=EXT-EPEX
C      EPAY=EYI-EPEY
C      EPAZ=EZI-EPEZ
C
C      FIND TRANSMISSION COEFFICIENTS
C      CALL TRANST(THETA1,TPER,TPAR)
C
C      EXT=EPEX*TPER+EPAX*TPAR
C      EYT=EPEY*TPER+EPAY*TPAR
C      EZT=EPEZ*TPER+EPAZ*TPAR
C
C      FIND TM COMPONENT OF TRANSMITTED RAY
C      ETTM=COSANG*EYT-SINANG*EZT
C
C      COMPUTE RHC COMPONENT AT ANTENNA
C
C      ERGHT=(EXT-J*ETTM)/SORT2
C
C      SUMA=SUMA+WSUM(ZM0)*ERGHT
C      DIFA=DIFA+WDIF(ZM0)*ERGHT
C      SJMB=SJMB+WSUM(XM0)*ERGHT
C      DIFB=DIFB+WDIF(XM0)*ERGHT
C
C      150 CONTINUE
C      50 CONTINUE
C
C      WILL WALL REFLECTIONS BE CONSIDERED?
C      IF (IREFL.NF.1)GO TO 2000
C
C      COMPUTATION OF REFLECTION DATA BEGINS HERE
C
C      CHECK FOR OPPOSITE WALL TRANSMISSION-REFLECTION
C      TIPSHD=ATAN(HIGH/RAD)
C      IF(ANG1.GT.TIPSHD)GO TO 2000
C
C      ARC=ARCIN
C      AL2=ARC*ARC
C      ZFIRST=-IFIX(HIGH/TTHETA/DELZ)*DELZ
C      XFIRST=-IFIX(RAD/DELX)*DELX
C      NUMXP=W/DELX+.5
C      DELZP=DELZ/SIN(ANG1)
C      NUMZP=-ZFIRST/DELZP+.5
C      YM=0.0
C
C      DO 1050 IZR=1,NUMZP
C      ZP=ZFIRST+(IZR-1)*DELZP

```

MAIN 6

```

C      DO 1050 IXR=1,NUMXP
C      XP=XFIRST+(IXR-1)*DELX
C
C      DETERMINE IF (XP,0.,ZP) IS INSIDE RADOME
C      IF(XP*XP+ZP*ZP.LE.RAD*RAD)GO TO 1050
C
C      DETERMINE IF RAY CAN INTERSECT RADOME
C      IF(XP*XP.GE.RADIN2)GO TO 1050
C      IF(SQRT(AL2-(C+ABS(XP))**2).LE.-ZP*TTHETA)GO TO 1050
C
C      FIND RAY REFLECTION POINT
C      ZL1=-SQRT(RADIN2-XP*XP)
C      CALL INTRSC(XR,YR,ZR,ZL1,0.0)
C
C      FIND OUTWARD NORMAL AT REFLECTION POINT
C      CALL NORM(XR,YR,ZR,NX,NY,NZ)
C
C      FIND UNIT VECTOR IN DIRECTION OF REFLECTED RAY
C      ADOTN2=2.0*(AY*NY+AZ*NZ)
C      CX=ADOTN2*NX
C      CY=ADOTN2*NY-AY
C      CZ=ADOTN2*NZ-1/Z
C
C      DETERMINE IF ANGLE OF INCIDENCE OF REFLECTED RAY IS
C      GREATER THAN 90. DEGREES AT ANTENNA APERTURE
C      DIRECTION OF INCIDENT FIELD ASSUMED FOR ANTENNA NORMAL
C      IF(CY*AY+AZ*CZ.GT.0.0)GO TO 1050
C
C      FIND REFLECTED RAY-ANTENNA APERTURE PLANE INTERSECTION
C      DIST IS REFLECTION POINT-INTERSECTION POINT DISTANCE
C      DIST=(YG-YR-ZR*TANALF)/(CY+CZ*TANALF)
C      XEND=CX*DIST+XR
C      YEND=CY*DIST+YR
C      ZEND=CZ*DIST+ZR
C
C      DETERMINE IF INTERSECTION IS INSIDE APERTURE
C      RHDAP=SQRT(XEND*XEND+ZEND*ZEND+(YEND-YG)**2)
C      IF(RHDAP.GE.APRAD)GO TO 1050
C
C      FIND RAY TRANSMISSION POINT
C      ZP1=-ZL1
C      CALL INTRSC(XT,YT,ZT,0.0,ZR1)
C
C      DEFINE INCIDENT FIELD MAGNITUDES
C      EXI=(1.0,0.0)*COSANE
C      EYI=CMPLX(EYITM,0.0)*SINANE
C      EZI=CMPLX(EZITM,0.0)*SINANE

```

MAIN 7

```

C
C FIND INCIDENCE ANGLE AT TRANSMISSION POINT
CALL NDRM(XT,YT,ZT,ANXT,ANYT,ANZT)
ANGTRN=ARCOS(AY*ANYT+AZ*ANZT)
C
C FIND TRANSMISSION COEFFICIENT AT TRANSMISSION POINT
CALL TRANST(ANGTRN,TPER,TPAR)
C
C FIND BINORMAL AT TRANSMISSION POINT
BT=(ANT X A)/ABS(ANT X A)
CALL CROSS(ANXT,ANYT,ANZT,0.0,AY,AZ,BXT,BYT,BZT)
C
C FIND PARALLEL AND PERPENDICULAR COMPONENTS
C OF INCIDENT FIELD AT TRANSMISSION POINT
C
EMAG1=BXT*EXI+BYT*EYI+BZT*EZI
EPEX=BXT*EMAG1
EPEY=BYT*EMAG1
EPEZ=BZT*EMAG1
C
EPAX=EXI-EPEX
EPAY=EYI-EPEY
EPAZ=EZI-EPEZ
C
C WEIGHT TRANSMITTED FIELDS WITH INSERTION TRANSMISSION
C COEFFICIENTS: TRANSMITTED FIELDS BECOME INCIDENT
C FIELDS AT REFLECTION POINT
C
EXI=EPEX*TPER+EPAX*TPAR
EYI=EPEY*TPER+EPAY*TPAR
EZI=EPEZ*TPER+EPAZ*TPAR
C
C FIND INCIDENCE ANGLE AT REFLECTION POINT
ANGREF=ARCOS(-NY*AY-NZ*AZ)
C
C FIND REFLECTION COEFFICIENT AT RAY REFLECTION POINT
CALL TRANSP(ANGREF,RPER,RPAR)
C
C COMPUTE COMPLEX INCIDENT FIELDS AT REFLECTION POINT
PHASE=PHASOR(BETAK*(ZR*AZ+YR*AY))
C
EXI=EXI*PHASE
EYI=EYI*PHASE
EZI=EZI*PHASE
C
C FIND BINORMAL AT REFLECTION POINT
BR=(-N X A)/ABS(-N X A)
CALL CROSS(-NX,-NY,-NZ,0.0,AY,AZ,BXR,BYR,BZR)

```

MAIN 8

```

C      FIND PARALLEL AND PERPENDICULAR COMPONENTS
C      OF INCIDENT FIELD AT REFLECTION POINT
C
      EMAG2=BXR*EXI+BYR*EYI+BZR*EZI
      EPEX=BXR*EMAG2
      FPEY=BYR*EMAG2
      EPEZ=BZR*EMAG2
C
      EPAX=EXI-EPEX
      EPAY=EYI-EPEY
      EPAZ=EZI-EPEZ
C
      FIND NJRMAL PART OF INCIDENT FIELD PARALLEL COMPONENT
      EPANML=EPAX*NX+EPAY*NY+EPAZ*NZ
      EPANX=EPANML*NX
      EPANY=EPANML*NY
      EPANZ=EPANML*NZ
C
      WEIGHT REFLECTED FIELDS WITH REFLECTION COEFFICIENTS
      EXR=EPEX*RPER+RPAR*(EPAX-2.0*EPANX)
      EYR=EPEY*RPER+RPAR*(EPAY-2.0*EPANY)
      EZR=EPEZ*RPER+RPAR*(EPAZ-2.0*EPANZ)
C
      COMPUTE INCIDENT FIELD AT APERTURE BY ACCOUNTING FOR
      PHASE SHIFT FROM REFLECTION POINT
      PHASE=PHASOF(-BETAK*DIST)
      EXR=EXR*PHASE
      EYR=EYR*PHASE
      EZR=EZR*PHASE
      ERTM=EYR*SINALF-EZR*COSALF
C
      FIND RHC COMPONENT OF REFLECTED FIELD
      ERGHT=(EXR-J*ERTM)/SQRT2
C
      COMPUTE OBLIQUITY FACTOR
      OBLIQ=0.5-0.5*(AY*CY+AZ*CZ)
      ZEND=ZEND/COSALF
      WGTSA=WSUM(ZEND)*OBLIQ
      WGTDA=WDIF(ZEND)*OBLIQ
      WGTSB=WSUM(XEND)*OBLIQ
      WGTDB=WDIF(XEND)*OBLIQ
C
      SUMA=SUMA+ERGHT*WGTSA
      DIFA=DIFA+ERGHT*WGTDA
      SUMB=SUMB+ERGHT*WGTSB
      DIFB=DIFB+ERGHT*WGTCB
1050 CONTINUE

```

MAIN 9

```

C
2000 CONTINUE
C
      PRINT102,SUMA,SUMB,DIFA,DIFB
102  FORMAT(' ',SUMA=' ',2E15.6,5X,SUMB=' ',2E15.6,/
      #,' DIFA=' ',2E15.6,5X,' DIFB=' ',2E15.6)
C
C      COMPUTE COMPLEX INDICATED ANGLES
      CAA=-MONOSF(IMS)*J*DIFA/SUMA
      CAB=+MONOSF(IMS)*J*DIFB/SUMB
C
      CAAMPA=CABS(CAA)*RTD
      CAAMPB=CABS(CAB)*RTD
      CAPHSA=ATAN2(AIMAG(CAA),REAL(CAA))*RTD
      CAPHSB=ATAN2(AIMAG(CAB),REAL(CAB))*RTD
C
      WRITE(6,108) CAAMPA,CAPHSA,CAAMPB,CAPHSB
108  FORMAT(' ',ALPHA COMPLEX ANGLE = ',E12.4,' AT',F6.1,
      #,' DEGREES',/, ' BETA COMPLEX ANGLE = ',E12.4,' AT',
      #F6.1,' DEGREES')
C
      CAAMP1(IANG)=CAAMPA
      CAAMP2(IANG)=CAAMPB
      CAPH1(IANG)=CAPHSA
      CAPH2(IANG)=CAPHSB
      ALFERR=REAL(CAA)
      BETERR=REAL(CAB)
      ADEG=ALFERR*RTD
      BDEG=BETERR*RTD
      PRINT109,ADEG,BDEG
109  FORMAT(' ',ALPHA INDICATED ERROR=' ',F10.6,' DEGREES',/,
      #,' BETA INDICATED ERROR=' ',F10.6,' DEGREES')
C
      IF(IREPOS)750,750,751
C
751  ALPHA=ALPHA+ALFERR
      BETA=BETA+BETERR
      ERFORA=(ALPHA-PI/2.0+ANG1)*RTD
      ERRORB=BETA*RTD
      IF(ABS(ALFERR).LT.ERRMAX.AND.ABS(BETERR).LT.ERRMAX)
      #GO TO 350
C
300  CONTINUE
      GO TO 350
C
750  ERFORA=ADEG
      ERRORB=BDEG
350  PRINT106,ERFORA,ERRORB,IPoint

```

THIS PAGE IS BEST QUALITY PRACTICABLE
FROM COPY FURNISHED TO DDC

MAIN 10

```

106 FORMAT(' ', 'ALPHA POINTING ERROR= ', F8.5, ' DEGREES',
#/, ' BETA POINTING ERROR= ', F8.5, ' DEGREES, OBTAINED ',
# 'AFTER ', I3, ' ITERATIONS', //)
C
ERRRCA(IANG)=ERRORA
ERRRCB(IANG)=ERRORB
C
400 CONTINUE
ANGE=ANGE*RTD
PRINT107, ANGE
107 FORMAT(' ', 'E ANGLE= ', F6.3, ' DEGREES')
C
CALL LPL0T(ARG,ERRRCA,CAPHS1,NANG,LABEL(1),1)
CALL LPL0T(ARG,ERRRCB,CAPHS2,NANG,LABEL(2),1)
CALL LPL0T(ARG,CAAMP1,CAPHS1,NANG,LABEL(1),1)
CALL LPL0T(ARG,CAAMP2,CAPHS2,NANG,LABEL(2),1)
700 CONTINUE
C
STOP
END

```

NORM 17

```

SUBROUTINE NORM(X,Y,Z,NX,NY,NZ)
C
C THIS SUBROUTINE COMPUTES THE OUTWARD SURFACE
C REAL NX,NY,NZ,NR
COMMON/RDATA/ AL2,C,XM2,TTHETA,RAD,ARC
C
X=X+1.E-20
Z=Z+1.E-20
R=SQRT(X*X+Z*Z)
NY=Y/ARC
NR=SQRT(1.-NY*NY)
NX=X/R*NR
NZ=Z/R*NR
RETURN
END

```

THIS PAGE IS RELEASED
FROM GOV. POL. FILE

INTRSC 11

```

C      SUBROUTINE INTRSC(X,Y,Z,XL1,XR1)
C      THIS SUBROUTINE COMPUTES THE RAY-RADOME INTERSECTION
C      POINT, (X,Y,Z), OF A RAY PASSING THROUGH THE POINT,
C      (XM,YM,ZM), AT THE SPHERICAL ANGLE THETA
C      WITH  $XL1 < Z < XR1$ .

      EXTERNAL FCT
      DATA EPS/2.0E-4/
      COMMON/RDATA/ AL2,C,XM2,TTHETA,RAD,ARC
      COMMON/MESPOS/ XM,YM,ZM
      XM2=XM*XM

C
C      CHECK FOR NORMAL INCIDENCE
      IF(ABS(TTHETA).GT.1.E03)GO TO 90

C
C      EPS IS MAXIMUM ERROR IN WAVELENGTHS
      CALL RTMI(ROOT,F,FCT,XL1,XR1,EPS,25,IER)
      Z=ROOT
      X=XM
      Y=SQRT(AL2-(SQRT(XM2+Z*Z)+C)**2)
      IF(IER.EQ.0)RETURN
      PRINT 20,IER
20  FORMAT(' ','SUBROUTINE RTMI DID NOT FIND RAY',
      *'INTERSECTION POINT',/, ' ERROR CODE IS IER= ',I2)
      STOP
90  X=XM
      Z=ZM
      Y=SQRT(AL2-(SQRT(XM2+Z*Z)+C)**2)
      RETURN
      END

```

FCT 12

```

C      FUNCTION FCT(Z)
C
C      FCT IS THE DIFFERENCE IN THE Y-COORDINATES OF A
C      RAY PASSING THROUGH (XM,YM,ZM) AND THE RADOME
C      SURFACE AS A FUNCTION OF Z
      COMMON/RDATA/ AL2,C,XM2,TTHETA,RAD,ARC
      COMMON/MESPOS/ XM,YM,ZM
      FCT=YM+(Z-ZM)*TTHETA-SQRT(AL2-(SQRT(XM2+Z*Z)+C)**2)
      RETURN
      END

```

INIT 13

```

SUBROUTINE INIT(N)
C   THIS SUBROUTINE INITIALIZES THE MATRICES USED FOR
C   TRANSMISSION AND REFLECTION COEFFICIENT INTERPOLATION
C   N EQUISPACED DATA POINTS ARE USED
C
  COMPLEX ATPER(50),ATPAR(50),ARPER(50),ARPAR(50)
  REAL ANG(50),PI/3.141593/
  COMPLEX TPER,TPAR,RPER,RPAR,PHASOR,CMLX
  COMMON/TDATA/ATPER,ATPAR,ARPER,ARPAR,ANG,DIF0,DIF1,
  *DIF2,DEL,M,D0,D1,D2
  PHASOR(X)=CMPLX(COS(X),SIN(X))
C
  DEL=PI/2.0/FLOAT(N-1)
  DO 10 I=1,N
    ANG(I)=DEL*(I-1)
    CALL TRANS(ANG(I),TPER,TPAR,ARPER(I),ARPAR(I),
  *PERIPD,PARIPD)
C
C   COMPUTE INSERTION TRANSMISSION COEFFICIENTS
  ATPER(I)=CABS(TPER)*PHASOR(-PERIPD)
  ATPAR(I)=CABS(TPAR)*PHASOR(-PARIPD)
10 CONTINUE
  D0=2.0*DEL*DEL
  D1=-DEL*DEL
  D2=D0
  M=N
  RETURN
END

```

WSUM 22

```

FUNCTION WSUM(ZM0)
C   SUM WEIGHTING FUNCTION
C   REAL PI/3.141593/
C   COMMON /WEIGHT/ APRAD,IMS,R
C
  IMS=1 UNIFORM
  IMS=2 COSINE TAPER
C
  GO TO(10,20),IMS
C
10 WSUM=1.0
  RETURN
C
20 WSUM=COS(PI/2.*R/APRAD)
  RETURN
END

```

WDIF 23

```

C      FUNCTION WDIF(ZM0)
C      DIFFERENCE WEIGHTING FUNCTION
C      COMMON /WEIGHT/ APRAD,IMS,R
C      GO TO(1,2),IMS
C
1 WDIF=ZM0*2.0/APRAD
  RETURN
C
2 WDIF=ZM0*2.93106/APRAD*WSUM(ZM0)
  RETURN
  END

```

TRANST 14

```

C      SUBROUTINE TRANST(ARG,TPERI,TPARI)
C      THIS SUBROUTINE INTERPOLATES THE TRANSMISSION DATA
C      SUPPLIED BY INIT WITH A SECOND ORDER CURVE THROUGH
C      THE THREE CLOSEST DATA POINTS.
C
C      COMPLEX ATPER(50),ATPAR(50),ARPER(50),ARPAR(50)
C      REAL ANG(50),AL(3)
C      COMPLEX TPERI,TPARI,CMPLX,PHASOR
C      COMMON/CDATA/ATPER,ATPAR,ARPER,ARPAR,ANG,DIF0,
C      *DIF1,DIF2,DEL,N,D0,D1,D2
C
C      I=ARG/DEL+1.5
C      IF(I.EQ.1)I=2
C      IF(I.EQ.N)I=N-1
C      DIF0=ARG-ANG(I-1)
C      DIF1=ARG-ANG(I)
C      DIF2=ARG-ANG(I+1)
C      AL(1)=DIF1*DIF2/D0
C      AL(2)=DIF0*DIF2/D1
C      AL(3)=DIF0*DIF1/D2
C      TPERI=(0.0,0.0)
C      TPAFI=(0.0,0.0)
C      DO 10 K=1,3
C      TPERI=TPERI+ATPER(I-2+K)*AL(K)
10 TPAFI=TPAFI+ATPAR(I-2+K)*AL(K)
  RETURN
  END

```

TRANSR 15

```

C      SUBROUTINE TRANSR(ARG,RPER,RPAR)
C      THIS SUBROUTINE INTERPOLATES THE REFLECTION DATA
C      SUPPLIED BY INIT WITH A SECOND ORDER CURVE.
C
C      COMPLEX ARPER(50),ARPAR(50),RPER,RPAR,ATPER(50),
C      #ATPAR(50)
C      REAL ANG(50),AL(3)
C      COMMON/TDATA/ATPER,ATPAR,ARPER,ARPAR,ANG,DIFO,
C      #DIF1,DIF2,DEL,N,D0,D1,D2
C
C      I=ARG/DEL+1.5
C      IF(I.EQ.1) I=2
C      IF(I.FO.N) I=N-1
C      DIFO=ARG-ANG(I-1)
C      DIF1=ARG-ANG(I)
C      DIF2=ARG-ANG(I+1)
C      AL(1)=DIF1*DIF2/D0
C      AL(2)=DIFO*DIF2/D1
C      AL(3)=DIFO*DIF1/D2
C      RPER=(0.0,0.0)
C      RPAR=(0.0,0.0)
C      DO 10 K=1,3
C      RPER=RPER+ARPER(I-2+K)*AL(K)
10  RPAR=RPAR+ARPAR(I-2+K)*AL(K)
C      RETURN
C      END

```

CROSS 16

```

C      SUBROUTINE CROSS(AX,AY,AZ,BX,BY,BZ,CX,CY,CZ)
C      THIS SUBROUTINE COMPUTES THE NORMALIZED CROSS
C      PRODUCT OF A INTO B
C      C=(A X B)/ABS(A X B)
C
C      CX=AY*BZ-AZ*BY
C      CY=AZ*BX-AX*BZ
C      CZ=AX*BY-AY*BX
C      CMAG=SQRT(CX*CX+CY*CY+CZ*CZ)
C      CX=CX/CMAG
C      CY=CY/CMAG
C      CZ=CZ/CMAG
C      RETURN
C      END

```

U.S. GOVERNMENT PRINTING OFFICE: 1964
 FROM THE NATIONAL BUREAU OF STANDARDS

TRANS 18

SUBROUTINE TRANS(THETA,TPERP,TPARA,RPERP,RPARA,
#PERIPD,PARIPD)

```

C
C   THIS SUBROUTINE COMPUTES COMPLEX TRANSMISSION AND
C   REFLECTION COEFFICIENTS FOR MULTIPLE-LAYER,
C   SANDWICHED, PLANAR SHEETS.
C
C   ALL DIMENSIONED VARIABLES HAVE BEEN DIMENSIONED FOR
C   A MAXIMUM OF FIVE LAYERS.

```

C DIMENSIONS IN THIS SUBROUTINE ARE IN METERS

```

C TPERP COMPLEX PERPENDICULAR TRANSMISSION COEFFICIENT
C TPARA COMPLEX PARALLEL TRANSMISSION COEFFICIENT
C RPERP COMPLEX PERPENDICULAR REFLECTION COEFFICIENT
C RPARA COMPLEX PARALLEL REFLECTION COEFFICIENT
C THETA ANGLE OF INCIDENCE
C NL NUMBER OF LAYERS SANDWICHED TOGETHER
C BETA PROPAGATION CONSTANT IN AIR
C MU PERMEABILITY OF LAYER RELATIVE TO AIR
C EPSILN DIELECTRIC CONSTANT OF LAYER RELATIVE TO AIR
C TANDEL DIELECTRIC LOSS TANGENT
C SIGMA CONDUCTANCE OF LAYER
C GAMMAI PROPAGATION CONSTANT
C YIPERP PERPENDICULAR ADMITTANCE
C YIPARA PARALLEL ADMITTANCE
C THIK THICKNESS OF LAYER
C TOTD TOTAL THICKNESS OF SANDWICHED LAYERS
C PERIPD PERPENDICULAR INSERTION PHASE DELAY
C PARIPD PARALLEL INSERTION PHASE DELAY

```

```

COMPLEX Z,CEXP,CSQRT,CDY,J/(0.0,1.0)/,CMPLX
COMPLEX TPERP,TPARA,KEP,GAMMAI,YIPARA,YIPERP,Z,F
COMPLEX APP,BPP,CPP,DPP,APR,BPR,CPR,DPR,APRPR,BPRPR
COMPLEX CPRPR,DPRPR,APAPR,BPAPR,CPAPR,DPAPR
COMPLEX G,H,S,T,RPERP,RPARA,COSH,CSINH
COMPLEX APERP(5),BPERP(5),CPERP(5),DPERP(5)
COMPLEX APAPA(5),BPAPA(5),CPAPA(5),DPAPA(5)
DIMENSION KMU(5),KEP(5),GAMMAI(5),YIPERP(5),YIPARA(5)
DIMENSION EPSLN(5),LYN(5),THIK(5),MU(5),SIGMA(5)
DIMENSION TANDEP(5),DDY(5)
REAL LAMDA,MU,PI/3.141593/,KMU
INTEGER LFLAG/D/
EQUIVALENCE(MU,KMU)
COMMON/TH/THIKWL

```

$$\begin{aligned} \cosh(Z) &= (e^Z + e^{-Z})/2. \\ \sinh(Z) &= (e^Z - e^{-Z})/2. \end{aligned}$$

THIS PAGE IS BEST QUALITY PRACTICABLE
FROM COPY FURNISHED TO LDC

TRANS 19

```

C      SINT=SIN(THETA)
      COST=COS(THETA)
      SINT2=SINT*SINT
C
C      CHECK IF DATA IS TO BE READ
      IF(LFLAG.LE.0)GO TO 100
C
500 DO 22 I=1,NL
      GAMMAI(I)=J*BETA*CSORT(KMU(I)*KEP(I)-SINT2)
      YIPERP(I)=CSORT(KMU(I)*KEP(I)-SINT2)/KMU(I)
      YIPARA(I)=KEP(I)/CSORT(KMU(I)*KEP(I)-SINT2)
      DDY(I)=GAMMAI(I)*THIK(I)
      APERP(I)=CCOSH(DDY(I))
      BPERP(I)=CSINH(DDY(I))/YIPERP(I)
      CPERP(I)=YIPERP(I)*CSINH(DDY(I))
      DPERP(I)=APERP(I)
      APARA(I)=APERP(I)
      BPARA(I)=CSINH(DDY(I))/YIPARA(I)
      CPARA(I)=YIPARA(I)*CSINH(DDY(I))
      DPARA(I)=DPERP(I)
22  CONTINUE
C
      IF (NL.EQ.1)GO TO 25
C
      APP=APERP(1)
      BPP=BPERP(1)
      CPP=CPERP(1)
      DPP=DPERP(1)
      APR=APARA(1)
      BPR=BPARA(1)
      CPR=CPARA(1)
      DPR=DPARA(1)
C
      DO 35 I=2,NL
      APRPR=APP*APERP(I)+BPP*CPERP(I)
      BPRPR=APP*BPERP(I)+BPP*DPERP(I)
      CPRPR=CPP*APERP(I)+DPP*CPERP(I)
      DPRPR=CPP*BPERP(I)+DPP*DPERP(I)
      APRR=APR*APARA(I)+BPR*CPARA(I)
      BPRR=APP*BPARA(I)+BPR*CPARA(I)
      CPRR=CPR*APARA(I)+DPR*CPARA(I)
      DPRR=CPR*BPARA(I)+DPR*DPARA(I)
      APP=APRPR
      BPP=BPRPR
      CPP=CPRPR
      DPP=DPRPR
      APR=APRR

```

THIS PAGE IS A MICROFILMED COPY OF THE ORIGINAL
 FROM THE NATIONAL ARCHIVES

TRANS 20

```

      BPR=BPARR
      CPR=CPARR
      DPR=DPARR
35  CONTINUE
30  CONTINUE
C
      E=APRPR+BPRPR*COST+CPRPR/CCOST+DPRPR
      F=APARR+BPARR/COST+CPARR*COST+DPARR
      TPARA=(2.0,0.0)/F
      TPERP=(2.0,0.0)/E
C
      G=APRPR+BPRPR*COST-CPRPR/CCOST-DPRPR
      H=APARR+BPARR/COST+CPARR*COST+DPARR
      RPERP=G/H
      S=APARR+BPARR/COST-CPARR*COST-DPARR
      T=APARR+BPARR/COST+CPARR*COST+DPARR
      RPARA=S/T
C
      PCON1=BETA*TOTD*COST
      PERIPD=-ATAN2(AIMAG(TPERP),REAL(TPERP))-PCON1
      PARIPD=-ATAN2(AIMAG(TPARA),REAL(TPARA))-PCON1
C
50  IF(PARIPD.GE.0.)GO TO 60
      PARIPD=PARIPD+2.*PI
      GO TO 50
60  IF(PERIPD.GE.0.) RETURN
      PERIPD=PERIPD+2.*PI
      GO TO 60
C
100  LFLAG=1
      FREQ=11.009
      LAMDA=3.0008/FREQ
      FREQG=FREQ/1.39
      WRITE(5,107) FREQG
107  FORMAT(' ','OPERATING FREQUENCY IS ',F5.2,' GHZ')
C
      TOTD=0.
      BETA=2.*PI*FREQ/3.0008
      READ(5,112) NL
112  FORMAT(I1)
C
      DO 12 I=1,NL
      READ(5,10) LYN(I),THIK(I),MU(I),EPSILN(I),TANDEP(I)
10  FORMAT(I1,4F10.0)
      TOTD=TOTD+THIK(I)
      SIGMA(I)=TANDEP(I)*2.*PI*FREQ*8.354E-12*EPSILN(I)
C
      IF(LYN(I).EQ.1) PRINT 3

```


TRANS 21

```

3  FORMAT('0',3X,'LAYER NO. THICKNESS MU EPSILON',
# ' SIGMA LOSS TANGENT ')
PRINT4,LYN(I),THIK(I),MU(I),EPSILN(I),SIGMA(I),
#TANDEP(I)
4  FORMAT('0',5X,I2,9X,F7.5,3X,F5.3,3X,F5.3,4X,E9.3,5X,
#E12.6,3X,F8.4)
KEP(I)=EPSILN(I)*(1.-J*TANDEP(I))
12 CONTINUE
THIKWL=TOTD/LAMDA
WRITE(6,105)
105 FORMAT('1')
GO TO 500
C
25 APRPR=APEPP(1)
BPRPR=BPERP(1)
CPRPR=CPERP(1)
DPRPR=DPERP(1)
APARR=APAPA(1)
BPARR=BPARA(1)
CPARR=CPARA(1)
DPARR=DPARA(1)
GO TO 30
C
END

```

UNCLASSIFIED

SECURITY CLASSIFICATION OF THIS PAGE (When Data Entered)

REPORT DOCUMENTATION PAGE		READ INSTRUCTIONS BEFORE COMPLETING FORM	
1. REPORT NUMBER 14) AU-EE-0022-Final	2. GOVT ACCESSION NO. AD-A085 263	3. RECIPIENT'S CATALOG NUMBER	
4. TITLE (and Subtitle) 6) INVESTIGATION OF COMPLEX ANGLE PROCESSING TO REDUCE RADOME INDUCED ANGLE POINTING ERRORS		5. TYPE OF REPORT & PERIOD COVERED Final Technical Report Dec. 10, 1976/Sept. 15, 1978	
7. AUTHOR(s) 10) David G. Burks Edward R. Graf		8. CONTRACT OR GRANT NUMBER(s) 15) DAAK40-77-C-0022	
9. PERFORMING ORGANIZATION NAME AND ADDRESS Auburn University Engineering Experiment Station Auburn, AL 36830		10. PROGRAM ELEMENT, PROJECT, TASK AREA & WORK UNIT NUMBERS Radar Technology Advanced Sensors Directorate Technical Requirement No. 6150	
11. CONTROLLING OFFICE NAME AND ADDRESS Headquarters, US Army Missile R & D Command ATTN: DR DMI - ICBB/Roberts Redstone Arsenal, AL 35809		12. REPORT DATE October 1, 1979	
14. MONITORING AGENCY NAME & ADDRESS (if different from Controlling Office) Office of Naval Research, Atlanta Area Office Georgia Institute of Technology 325 Hinman Research Building Atlanta, GA 30332		13. NUMBER OF PAGES 205	
		15. SECURITY CLASS. (of this report) UNCLASSIFIED	
16. DISTRIBUTION STATEMENT (of this Report) DISTRIBUTION STATEMENT Approved for public release, Distribution Unlimited		15a. DECLASSIFICATION/DOWNGRADING SCHEDULE 1: 207	
17. DISTRIBUTION STATEMENT (of the abstract entered in Block 20, if different from Report) 9) Final technical report DA 76-15 SEP 78			
18. SUPPLEMENTARY NOTES			
19. KEY WORDS (Continue on reverse side if necessary and identify by block number) Radome Analysis Radome Induced Pointing Error Complex Angle Processing to Reduce Angle Pointing Errors			
20. ABSTRACT (Continue on reverse side if necessary and identify by block number) This work is an analysis of the effect of a tangent ogive radome on the pointing accuracy of a monopulse radar that employs an aperture antenna. The incident fields at the antenna are found by a ray-tracing procedure. The theory of monopulse radar and the transmission and reflection properties of planar dielectric slabs are presented. Two orthogonal polarization states which can be combined to produce an arbitrarily polarized incident field are considered. The antenna can be			

DD FORM 1 JAN 73 1473

EDITION OF 1 NOV 68 IS OBSOLETE

S. N 0102-LE-014-6601

UNCLASSIFIED

SECURITY CLASSIFICATION OF THIS PAGE (When Data Entered)

402958

UNCLASSIFIED

SECURITY CLASSIFICATION OF THIS PAGE (When Data Entered)

20. (con't)

scanned in two angular directions and radar pointing error is presented for both these angles as a function of antenna scan angle and polarization of the incident field.

A method that can be used to compensate for radome-induced error is presented. Complex angle processing for the purpose of pointing angle reduction was investigated.

S N 0102- LF- 014- 6601

UNCLASSIFIED

SECURITY CLASSIFICATION OF THIS PAGE (When Data Entered)